UNIVERSITÀ DEGLI STUDI DI PADOVA

UNIVERSITA' DEGLI STUDI DI PADOVA

DEPARTMENT OF CHEMICAL SCIENCES

PH. D. COURSE IN MOLECULAR SCIENCES
CHEMICAL SCIENCES CURRICULUM
XXXI CYCLE

FUNCTIONAL MATERIALS FOR PICKERING EMULSIONS

Coordinator: **Prof. Leonard Jan Prins**

Supervisor**: Prof. Michele Maggini**

Ph. D. Student: **Andrea Faresin**

Acronyms and abbreviations

HLB: Hydrophilic Lipophilic Balance

PE: Pickering Emulsion

ISC: InterSystem Crossing

TATP: TriAcetone TriPeroxide

TEM: Transmission Electron Microscopy

ATR-IR: Attenuated Total Reflectance-Infrared Spectroscopy

DLS: Dynamic Light Scattering

Np: Nanoparticle

SiO_2-Me: Silica nanoparticles functionalized with methyl-trimethoxy silane

SiO_2-tBu: Silica nanoparticles functionalized with di-methyl-t-buthyl-chlorosilane

SiO_2-C_{18}: Silica nanoparticles functionalized with di-methyl-n-octadecyl-chlorosilane

PTFE: PolyTetraFluoroEthylene

UV: UltraViolet

FULP: N-(3-propyltriethoxysilyl)-2-carbomethoxy-3,4-fulleropyrrolidine

SiO_2-FULP: Silica nanoparticles functionalized with FULP

DIBF: Diphenyl-IsoBenzoFuran

TEA: TriEthylAmine

FITC: Fluorescein IsoThioCyanate

DMSO: DiMethyl SulfOxide

APTES: N-(3-aminopropyl) triethoxysilane

MDBP: Methyl-DiBromo-Propionate

NMR: Nuclear Magnetic Resonance

TLC: Thin Layer Chromatography

GC-MS: Gas Chromatography-Mass Spectrometry

LED: Light Emitting Diode

NCC: NanoCrystalline Cellulose

TEMPO: (2,2,6,6-Tetramethylpiperidin-1-yl)-oxyl

PU: PolyUrethane

PU-NCC: Polyurethane-NCC composite material

NCC-Dye, NCC-GM1: NCC functionalized with GM1 dye

TEOS: TetraEthOxy Silane

NCC-Fe_3O_4: NCC- Fe_3O_4 hybrid material

NCC-TA: NCC functionalized with tannic acid

NCC-NH_2, NCC-APTES: NCC functionalized with APTES

EDC: 1-Ethyl-3-(3-dimethylaminopropyl)carbodiimide

NHS: N-Hydroxysuccinimide

TGA: TermoGravimetric Analysis

DMCHA: N,N-Dimethylcyclohexylamine

PMDETA: N,N,N',N'',N''-Pentamethyldiethylenetriamine

LOI: Limiting Oxygen Index

TA: Tannic Acid

DMF: DiMethylFormamide

RT: Room Temperature

MR: MicroReactor

XPS: X-ray Photoelectron Spectroscopy

BET: Brunauer-Emmett-Teller surface area analysis

XRD: X-Ray Diffraction

CNT: Classical Nuclear Theory

HER: Hydrogen Evolution Reaction

BE: Binding Energy

MAUD: Material Analysis Using Diffraction

PEEK: PolyEther Ether Ketone

GC-TCD: Gas Chromatography-Thermal Conductivity Detector

TPP: Meso-Tetraphenylporphyrin

NBS: N-BromoSuccinimide

HPLC: High Performance Liquid Chromatography

IMM: Interdigital MicroMixer

ESI-MS: Electron Spray Ionization-Mass Spectrometry

Contents

Abstract

This doctoral thesis highlights the most interesting experimental results achieved between 2015 and 2018 by the author, during his stay in the laboratories of the Department of Chemical Sciences of the University of Padova. The *fil rouge* of this thesis work is Pickering Emulsions (PE); emulsions where solid particles alone are used as stabilizers instead of the typical molecular or macromolecular surfactants that are employed to produce widely used emulsions in pharmaceutics, drug delivery, cosmetics, food industry to name a few. Solid micro/nanoparticles accumulate at the interface between two immiscible liquids (typically denoted as oil and water phase) and stabilize droplets against coalescence. A great advantage of a PE is that it is relatively stable once made and that many solid particles can be endowed with useful characteristics: conductivity, responsiveness, porosity, catalysis and so on.

The chemical modification of silica nanoparticles (SiNP) and their use as PE stabilizers is the first theme treated in this thesis work. SiNP are functionalized with hydrophobic molecular structures for tuning their wettability, and with photo-active moieties to impart photocatalytic properties. In addition, silica-based PE are used to confine special ingredients needed for the colorimetric detection of acetone whose presence is associated to triacetone triperoxide, a deadly explosive used by terrorists in recent attacks, and for the development of a testing kit in the form of a pen.

Another interesting PE stabilizer is nanocrystalline cellulose (NCC). An extensive sperimentation was carried out to learn how to handle and to chemically functionalize NCC. This led to the development of robust protocols that allowed to install on cellulose nanocrystals a pH-sensitive dye and magnetic nanoparticles that were used to develop, as a proof of principle, a solid pH sensor for urea detection and a colorimetric/magnetic, doubly-responsive system. The modified NCC materials hold the potential as PE stabilizers whose study is underway.

The last part of the thesis reports the study, in collaboration with prof. S. Gross of the Chemical Sciences Department in Padova and prof. E. Hensen of the University of Eindhoven, for the production of ZnS nanoparticles through a controlled nucleation and crystallization under continuous flow conditions at room temperature, in water and without the use of any stabilizing ligand. The colloids display an average size of 5 nm and an impressively high specific surface area of 287 m^2/g. Nanostructured ZnS is well known to be a direct wide-bandgap semiconductor and, for its tunable photophysical and electrochemical properties, is used for a broad range of applications ranging from catalysis and photocatalysis to nonlinear optics, optoelectronic devices and optical bioimaging. The possibility to prepare stable nanoparticles without the need of special ligand stabilization open the interesting

perspective to use those as-prepared particles directly from the continuous flow reactor to stabilize functional PE. Work in this direction is currently underway.

Furthermore, a toolbox that was always available during this thesis work was flow chemistry, an ensemble of techniques for the manipulation of fluids on the micrometer scale. Such manipulation is carried out inside microchannels, confined environments whose geometries can be exploited to optimize unit operations – such as mixing and heat transfer – of profound interest for chemists. A flow chemistry approach was used to prepare ZnS nanoparticles and also to develop a selective bromination protocol of tetraphenyl porphyrins. This latter study, along with a study on the application of functionalized NCC as a flame retardant have been a unique opportunity to face interesting problems, although they were not related to the Pickering emulsions general theme of this thesis work.

Structure of the thesis

Chapter one outlines the state of the art of Pickering emulsions with particular emphasis on applications in the field of photocatalysis and sensing.

Chapter two deals with the preparations, characterization and use of functionalized nanocrystalline cellulose for the development of sensing devices and flame retardant systems

Chapter three presents the controlled nucleation and crystallization of small and ligand-free ZnS nanoparticles via a low temperature and easy microfluidic approach.

Chapter four presents the continuous-flow, selective monobromination of meso-tetraphenylporphyrin in β-pyrrolic position.

Chapter 1

Pickering emulsions

Emulsions are common systems in everyday life. They are often found in food, for example milk or sauces, in healthcare and detergence products. A lot of studies have been carried on to explain and exploit the properties of emulsions, especially from a chemical point of view[1-4].

Generally speaking, an emulsion is a colloidal system of two immiscible fluids, obtained by dispersing one (named dispersed phase) into the other (matrix fluid or dispersant). As a recollection from the past, the notation "oil-in-water" or "water-in-oil" is still used to highlight the structure of the emulsion. "Dispersed phase-in-matrix phase" can concisely explain which of the two fluids is confined into the droplets, while the terms "water" and "oil" refers to the hydrophilic or lipophilic nature of the components. An example of the structure of the emulsion is showed in figure 1.

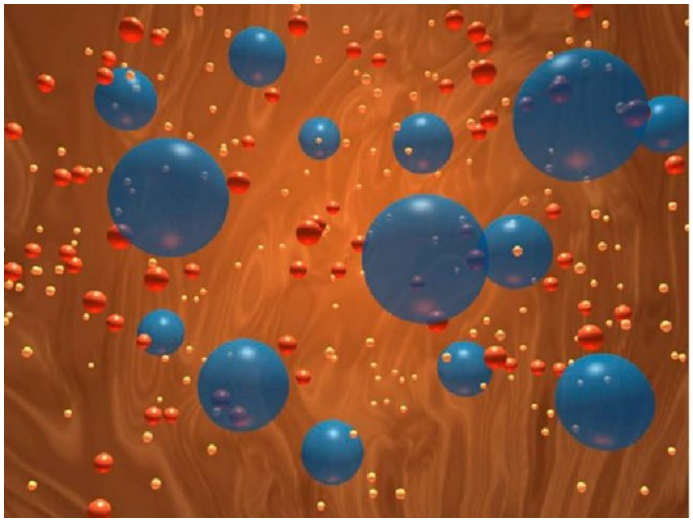

Figure 1. Graphic model of a multi-component colloidal system. Blue, red and orange spheres represent different droplets (dispersed phase); the background represents the dispersant (matrix phase).

To produce an emulsion it is necessary to mix intimately the two immiscible phases. This process generates a perturbation of the equilibrium state (where the phases are completely separated by density). Thermodynamically, the generation of an emulsion can be described by the variation of the equilibrium Gibbs free energy of the equilibrium state, from G_{eq} to G', where

$$G_{eq} = G_1 + G_2 + A_{12}\sigma_{12}$$

$$G' = G_1 + G_2 + A'_{12}\sigma_{12}$$

In a liquid-liquid system like the one studied in this thesis, G_1 and G_2 are the Gibbs free energies of the two liquids, σ_{12} is the surface tension between the two liquids and A_{12} is the total contact surface between the two phases. Since A_{12} is the only parameter that does not depend on the nature of the components, the system evolves to minimize it, which corresponds to the complete separation of the phases. Thus mixing process increases A_{12} to A'_{12}, generating droplets, the typical structure of emulsions.

However, after mixing, the system tends to the equilibrium state by reducing A'_{12}. At first, droplets assume spherical shape, the geometric solid with the lowest specific area; then droplets start to move, following Archimedes' law, to the top or the bottom of the system. In absence of a stabilizing agent, any collision between droplets leads to their coalescence and growth (since for a sphere the specific area scales with r^{-1}) until complete phase separation is reached.

Figure 2. In sequence from left to right, different steps of the collapse of an oil-in-water emulsion. On the left, freshly prepared emulsion; on the right, complete separation of the phases.

This separation process, known as coalescence, has catastrophic effects on the stability of emulsions, effects that are described by the sequence in figure 2.

Therefore, in order for the emulsions to be useful, it is first necessary to stabilize them. The surface tension between liquids (σ_{12}) can be reduced by adding specific molecules named surfactants at the liquid-liquid interface. The first application of molecular surfactants probably dates back to 1929 when Kurt von Neergaard studied the respiration mechanism[5]. A clear explanation of the properties and activity of surfactants arrives in 1950 by a series of seminal papers by Richard Pattle [6], Charles Macklin [7] and John Clements[8]. Surfactants are amphiphilic molecules with a polar head and non-polar tail. They can interpose between molecules at the liquid-liquid interphase reducing the surface tension and consequently, if used in adequate concentrations, stabilize droplets, as shown in figure 3.

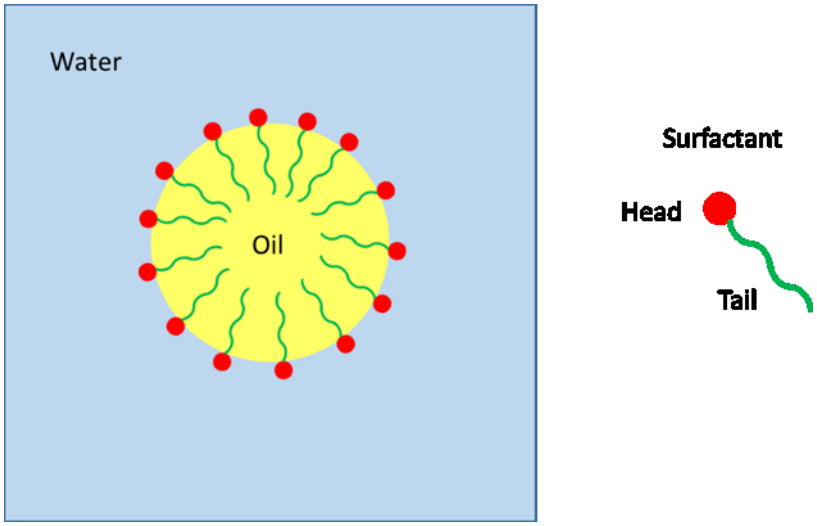

Figure 3. On the left, representation of a surfactant-stabilized emulsion. On the right, structure of a molecular surfactant.

The driving force that allows amphiphiles to adsorb at the interface is described by Hydrophilic-Lipophilic Balance (HLB) index:

$$HLB = 20 * \frac{M_h}{M}$$

where M_h is the molar mass of the hydrophilic moiety and M is the molar mass of the molecule.

Since their discovery, surfactants are the most common stabilizer used in industrial applications, in academic research and in everyday life. However, due to their molecular nature, surfactants have limited applications in some fields, especially in biology.

An alternative to molecular stabilizers came from 1907, when Spencer Umfreville Pickering first discovered that solid particles could adsorb at the liquid-liquid

interphase acting similarly to the surfactants[9]. As it often happens in science, Pickering emulsions (PE) did not become a trend immediately in academic research, but they were widely studied as an industrial application, especially in the field of oil refinery. Since the 80's, coincidently with the rise of nanomaterials as a scientific trend, Pickering emulsions have grown more and more interest in food chemistry, healthcare industry, detergence and, more recently, in catalysis and drug delivery[1-4].

From a thermodynamic point of view, solid nanoparticles behave similarly to molecular surfactants, as shown in figure 4.

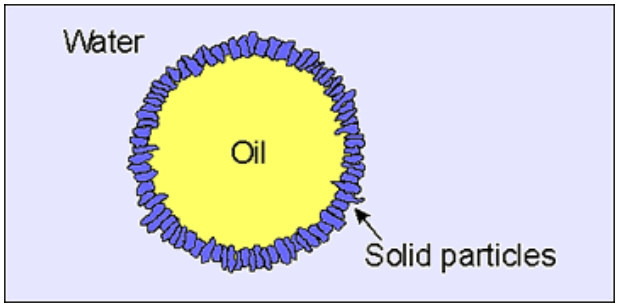

Figure 4. Structure of a Pickering emulsion stabilized by solid particles

Instead of the HLB index, in the case of solid particles the driving force is the wettability of their surface, expressed by the contact angle θ_w[10].

$$\Delta F_{ads} = -\pi r^2 \gamma_{L-L}(1 - |cos\theta_w|)$$

ΔF_{ads} is the Gibbs free energy of adsorption of a single particle at the interphase, r is the average hydrodynamic radius of the stabilizing particles and γ_{L-L} is the surface tension between the two liquids. Excluding γ_{L-L}, that is constant, two parameters are fundamental to determine the characteristics of PE. First, r, the dimension of the stabilizing material plays a fundamental role in the stability of the droplet. As thermodynamics suggests, bigger nanoparticles adsorbs strongly at the interface, granting very high stability. It becomes even more interesting if compared to the dimension of a molecular surfactant. In fact, Pickering emulsions are much more resistant to coalescence (years) than surfactant-stabilized emulsions (weeks-months). However, as logic suggests, the dimension of the stabilizer and the diameter of the stabilized droplet must be related in some way. Yves Chevalier studied this aspect and formulated the following mathematical description[11]:

$$D = \frac{6\varphi_{wd}}{\rho_d \varphi_{wp}(1 - \varphi_{wd})a_p}$$

D, the average diameter of the droplets depends on φ_{wd}, the weight fraction of the dispersed phase, on ρ_d, the density of the dispersed phase, φ_{wp} the weight fraction of

the stabilizing material and on the a_p term, named the maximum wet surface per mass unit of nanoparticles. a_p was further explained in the work by assuming that the droplets were covered by a single layer of nanoparticles with dense hexagonal packing[11].

$$a_p = \frac{3}{2\rho_{dp}D_p}$$

ρ_{dp} is the density of the stabilizing material and D_p its average hydrodynamic diameter. Then, even if larger particles adhere strongly to interphases, to stabilize Pickering emulsions specific nanoparticle sizes are required. So, the dimension of the stabilizer is not a practical operational parameter.

Thus, the only parameter that can be modified to increase the stability of the droplets is the contact angle of the material θ_w[12]. The wettability depends both on the nature of the stabilizer and on the chemical structure of the surface. With a chemical approach, functionalization allows to modify nanomaterials in order to add useful properties. In this case, the intrinsically hydrophilic nature of the starting material (for instance amorphous silica nanoparticles) can be tuned by adding hydrophobic molecules on the surface of the nanoparticles.

Apart from thermodynamics, there are also kinetic reasons that explain the high stability of PE. First of all, the addition of nanoparticles to a liquid increases the viscosity of the system. This effect is mainly due to the excess of nanoparticles that remains in the matrix phase after stabilization. In many cases, at high concentration of solid stabilizer, it is even possible to block the structure of the emulsion. This has a strong effect on the mobility of the components, especially on the Brownian motion that is a characteristic of colloidal systems. Droplets move slowly, so that coalescence is strongly delayed; moreover, the energy of collisions between nanoparticles is not enough to overcome the barrier of the Gibbs free energy of adsorption ΔF_{ads}, due to the decreased momentum of the stabilizer[10-11]. In other words, at room temperature Pickering emulsions are highly resistant to mechanical stress.

An interesting use of Pickering emulsions is reported here since it was exploited to develop a part of this thesis's project. Pickering emulsions can be employed to compartmentalize the reagents involved in a particular reaction as shown in figure 5.

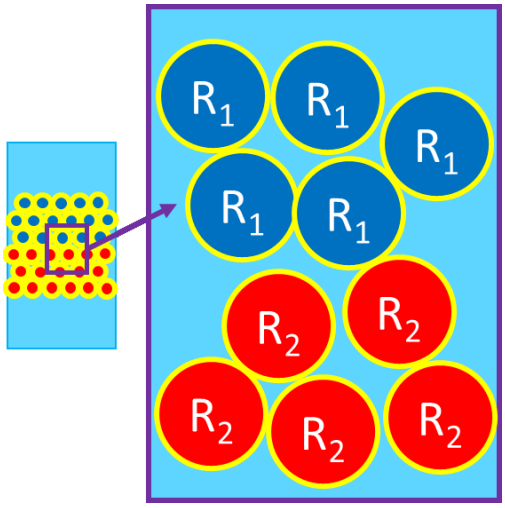

Figure 5. Example of compartmentalization of reagents 1 and 2 inside the droplets of an emulsion.

Thanks to the long term stability of the droplets, the reaction is inhibited until the PE is destroyed, for example, by mechanical stress. In addition, by compartmentalization of incompatible reagents (to avoid mutual quenching) and by introducing other reactive molecules in continuous phase which can diffuse freely to access the compartmentalized reagents, it was possible to carry out one-pot cascade reactions involving incompatible reagents such as deacetalization−reduction, deacetalization−Knoevenagel, de- acetalization−Henry and diazotization−iodization[13].

Photo-oxidation of organic molecules with singlet oxygen

From the electronic point of view, elemental oxygen is quite peculiar. Indeed, the ground state of this molecule is a triplet state, while the first excited state is singlet ($^1O_2$). Figure 6 shows the electronic configuration of O_2.

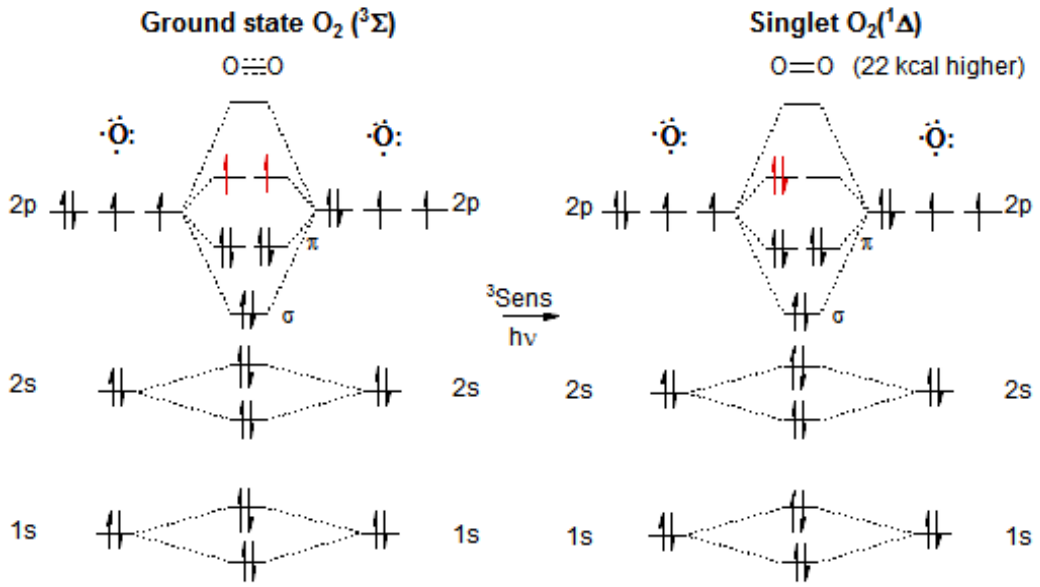

Figure 6. Diagram of the electronic states of oxygen. On the left, the triplet state. On the right, the singlet state.

Singlet oxygen is far more reactive than triplet oxygen, and for this reason it is a well known reagent in medicine for photodynamic therapy[14], and for photocatalytic applications, for example in oxidations, addition to double bonds and Diels-Alder reactions. However, from a toxicological point of view, the high reactivity of $^1O_2$ is dangerous for living tissues. To avoid undesired photodegradation of healthy tissues, it is necessary to control the generation and diffusion of activated oxygen species.

Generation of $^1O_2$ is usually achieved through sensitization of $^3O_2$, using a proper photosensitizer. In this work, C_{60}-fullerene was employed to the purpose of activating oxygen to its singlet state. This molecule, discovered in 1985 by Harold Walter Kroto[15], is a non-aromatic compound that can be excited by light in the visible range. Relaxation mechanism can be subjected to intersystem crossing (ISC), so to the transition from singlet excited state to triplet excited state. Figure 7 shows the chemical structure of [60]fullerene and its singlet-triplet transition.

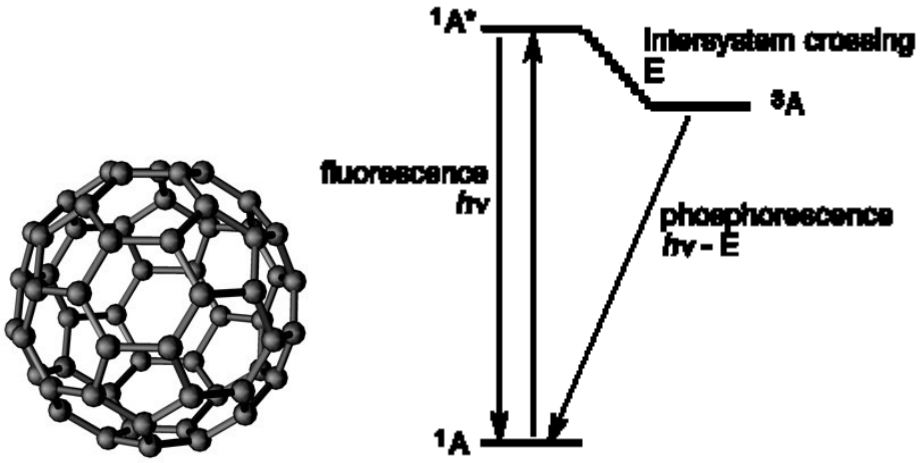

Figure 7. On the left, molecular structure of [60]fullerene. On the right, Jablonsky diagram with the electronic transition from singlet state ^1A to triplet ^3A.

The emitted photon has comparable energy to the $^3O_2 \rightarrow {}^1O_2$ transition, allowing the generation of singlet oxygen as reported in figure 8

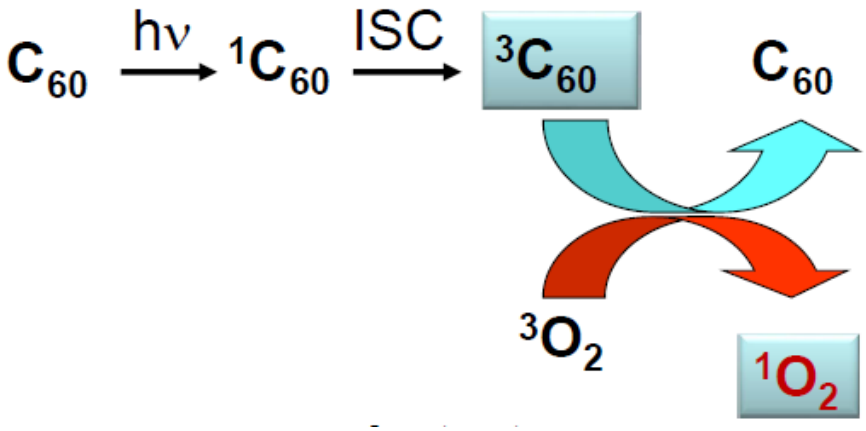

Figure 8. Mechanism of the photosensitization of singlet oxygen by [60]fullerene.

Apart from its electronic properties, [60]fullerene is an interesting molecular structure for organic chemistry. The spherical geometry [60]fullerene is responsible of the strain of the structure of double bonds, where the overlap of p_z orbitals is less efficient than in normal double bonds. This characteristic makes fullerene compounds reactive towards dipolar reagents, such as, for example, in 1,3-dipolar additions of azomethine ylides [16] as shown in figure 9.

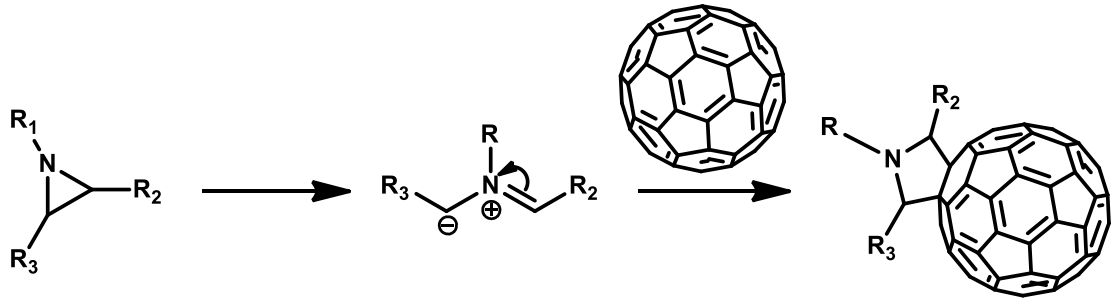

Figure 9. Mechanism of the formation of a fulleropyrrolidine via aziridine ring-opening.

In this thesis, we have used the 1,3 dipolar cycloaddition of azomethine ylides to functionalize the surface of silica nanoparticles with [60]fullerene. An aziridine starting material, bearing a triethoxy silane moiety, was used as 1,3-dipole precursor (vide infra).

Colorimetric detection of explosive triacetone triperoxide

Acetone is an important solvent or reagent in chemistry. It has a plethora of applications in everyday life and, for this reason, acetone is available in bulk quantities at different levels of purity. Acetone has been recently employed by terrorists to prepare hand-made explosives that were used in recent attacks. Richard Reid's shoe bomb in 2001, the bombings in London (2005), Boston marathon (2013) and more recently in Paris (2015) and Brussels (2016) are some sadly known terroristic attacks involving the use of TATP. The most famous acetone-based explosive is triacetone triperoxide (TATP) or "Satan's mother". Figure 10 clearly shows why TATP is so difficult to detect: it has harmless appearance (sugar-like microcrystalline white powders) and can pass undetected through explosive detection scanners designed to detect nitrate-containing explosives.

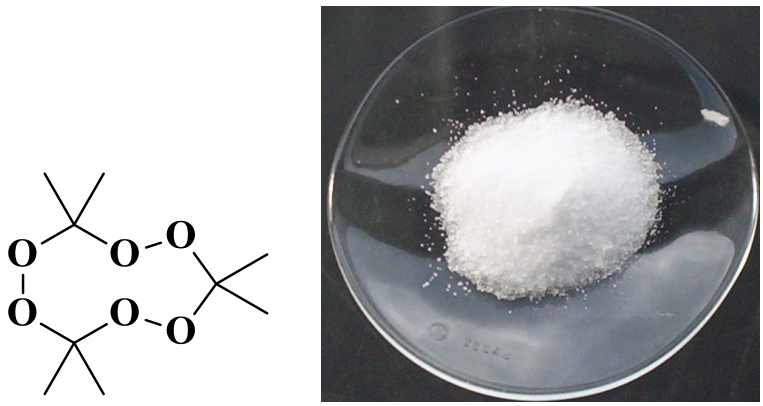

Figure 10. On the left, chemical structure of triacetone triperoxide and, on the right, the appearance of its solid form.

Triacetone triperoxide is obtained by mixing acetone with hydrogen peroxide in 1:1 molar ratio at 5°C. To catalyze the trimerization, a mineral acid is also added. Thus, all the reagents can be easily found and no specific equipment or skill is needed. The product has to be dried carefully to obtain a sugar-like powder with fruit-like smell, which is very unstable since it explodes easily if subjected to heat or friction. All these features make triacetone triperoxide a primary explosive, a high power compound with high sensitivity to mechanical and thermal stimulation.

For the chemical detection of TATP in the last few years a wide range of analytical techniques have been developed including infrared (IR) and raman spectroscopy, tandem chromatographic techniques (GC-MS, LC-MS), thin-layer chromatography (TLC), ion-mobility spectrometry (IMS), nuclear resonance spectrometry (NMR), electro-generated chemo-luminescence (EGC), and fluorescence. However, although these methods may offer low detection limits and high selectivity, they are normally the prerogative of laboratory facilities since they require complex and expensive instrumentation, trained staffs, and slow analysis speed. Therefore, it is paramount to supply the on-site personnel of security checkpoints of airports and mass transit facilities as well as crime scenes with robust, ease of use, cost-effective methods for rapid and selective identification and detection of TATP. In this quest, colorimetric methods constitute a powerful tool for qualitative analysis as they provide a diagnostic signal that can be intuitively detected by naked eye. In addition, results can be made semi-quantitative or quantitative by comparison with colour standards either visually or by using smartphone digital cameras[17]. Although current colorimetric assays reported in the literature were traditionally designed for clinical applications, environmental-analysis, beverages and food testing and so on[18], there is a flourishing of colorimetric tests targeting explosive materials. As far as TATP is concerned, it should be pointed out that most of the colorimetric assays so far reported do not directly detect TATP but rather the hydrogen peroxide produced by its decomposition through acidic hydrolysis. Some relevant protocols exploit the colorimetric detection of hydrogen peroxide for example by a horseradish-peroxidase enzyme coupled with a colour producing reagent (2,2-azino-bis(3-ethylbenzothiazoline)-6-sulfonate, ABTS, or p-hydroxyphenylacetic acid, *p*-HPAA); 2) a non-enzimatic colour reaction based on copper(II)-neocuproine; 3) titanyl oxalate and acidic KI reagent; 4) molybdenum hydrogen bronze suspension; 5) a combination of three azo-dyes. Surprisingly, the colorimetric detection of the acetone counterpart has not been exploited so far to detect TATP. Actually, there is a colorimetric test for acetone in medical environment that could be adapted for testing residual acetone in TATP or to detect acetone upon TATP decomposition in acid. The original test is based on a combination of glycin and sodium nitroprusside that can react with acetone in basic conditions to form a characteristic purple colour[19,20]. From the chemical point

of view, there are several reactions involved (figure 11) that have not been fully understood so far[21,22]. In particular, under the basic conditions needed for the formation of the purple colour, the sodium nitroprusside slowly decomposes producing an inactive green complex. This latter side reaction can be avoided by mixing the reagents just prior the analysis or making a dry formulation in the form of stickers that are dipped in the biological fluid for the test. Most importantly, these stickers do not show any reaction if simply exposed to acetone vapours, thus water must play a role.

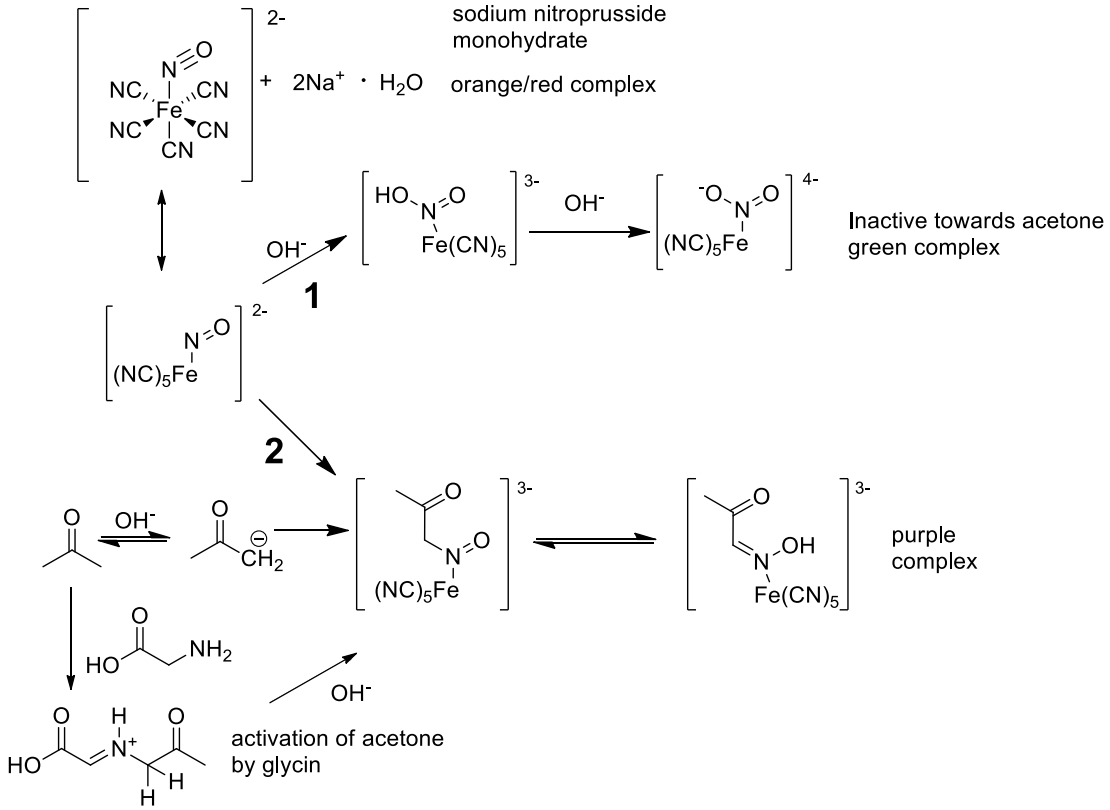

Figure 11. Reactivity of sodium nitroprusside towards bases and acetone.

Results and discussion

Preparation and characterization of silica nanoparticles as Pickering emulsion stabilizers

The stabilization of an emulsion with solid particles requires materials with specific wettability. Since we were interested in the production of toluene-in-water Pickering emulsion, a convenient approach is the uning of the hydrophilic or lipophilic nature of solid stabilizers. To this purpose, I used silica nanoparticles as starting materials, since they are cheap and commercially available in different sizes. The nanoparticles used here have a diameter of 12 nm in their dry state that increases up to 110 nm when dispersed in water, for the effect of aggregation. TEM images of silica nanoparticles used in this work are shown in figure 12.

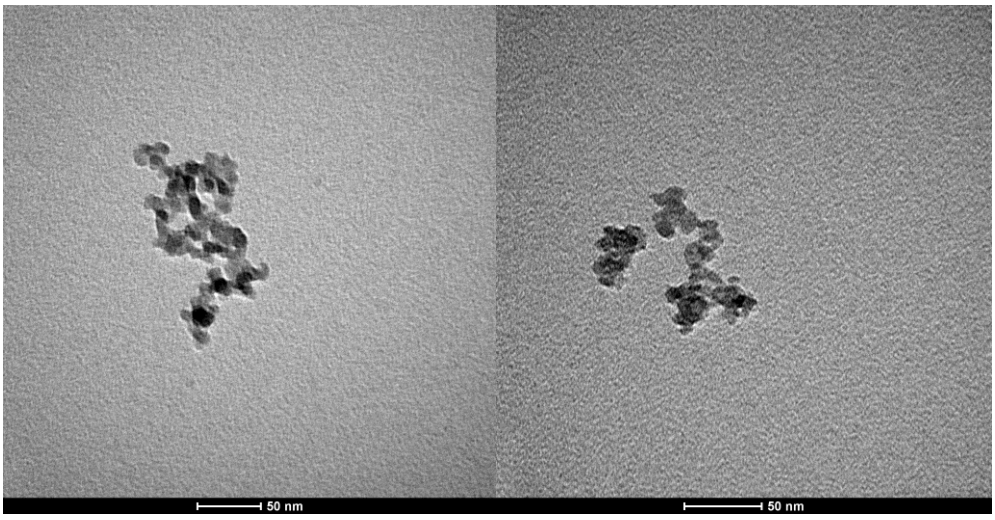

Figure 12. Images of silica nanoparticles dispersed in water.

As a consequence of the orthosilicate structure, the surface of silica nanoparticles displays –OH defects that are mainly responsible for their hydrophilic nature. An evaluation of the amount of hydroxyl group on the surface of commercial amorphous SiO_2 available for functionalization was made by Zhuravlev and coworkers who estimated an average of 5 hydroxyl groups per nm^2[23].

Assuming the shape of particles as spherical, with an average diameter d of 12 nm, the surface area S will be:

$$S = \pi d^2$$

The number of nanoparticles n can be obtained dividing the total mass of the stabilizer M by the average mass of a single particle m.

$$n = \frac{M}{m}$$

m can be obtained knowing the volume V and the density of amorphous silica ρ (2.2 g/cm^3).

$$m = V\rho = \frac{1}{6}\pi d^3 \rho$$

Following these steps, it is possible to evaluate the total number of hydroxyl groups N_{OH} and the stoichiometric amount of reagents that are necessary to functionalize the surface of silica nanoparticles.

$$N_{OH} = 5 * S * n$$

Since the surface of silica nanoparticles can be functionalized only partially, a large excess of reagents was employed to functionalize the surface as much as possible so to markedly reduce the hydrophilicity of the nanoparticles.

To this purpose the use of alkyl-silanes is considered the most convenient way to immobilize hydrophobic moieties on the surface of silica[24,25]. In particular, chlorosilanes and alkoxysilanes can react with –OH groups, to add peculiar properties to nanomaterials. In this case, commercial silanes were employed, bearing different alkyl chains in order to study the effects of the chain structure on the affinity of nanoparticles towards the water phase. In particular, the alkyl silane compounds employed contained, respectively, a short alkyl chain (trimethoxy-methyl silane), a branched chain (t-butyl-dimethyl chlorosilane) and a long linear chain (octadecyl-dimethyl chlorosilane), are shown in figure 13. The silanization reactions were carried out in dry toluene under reflux in the presence of triethylamine as a base.

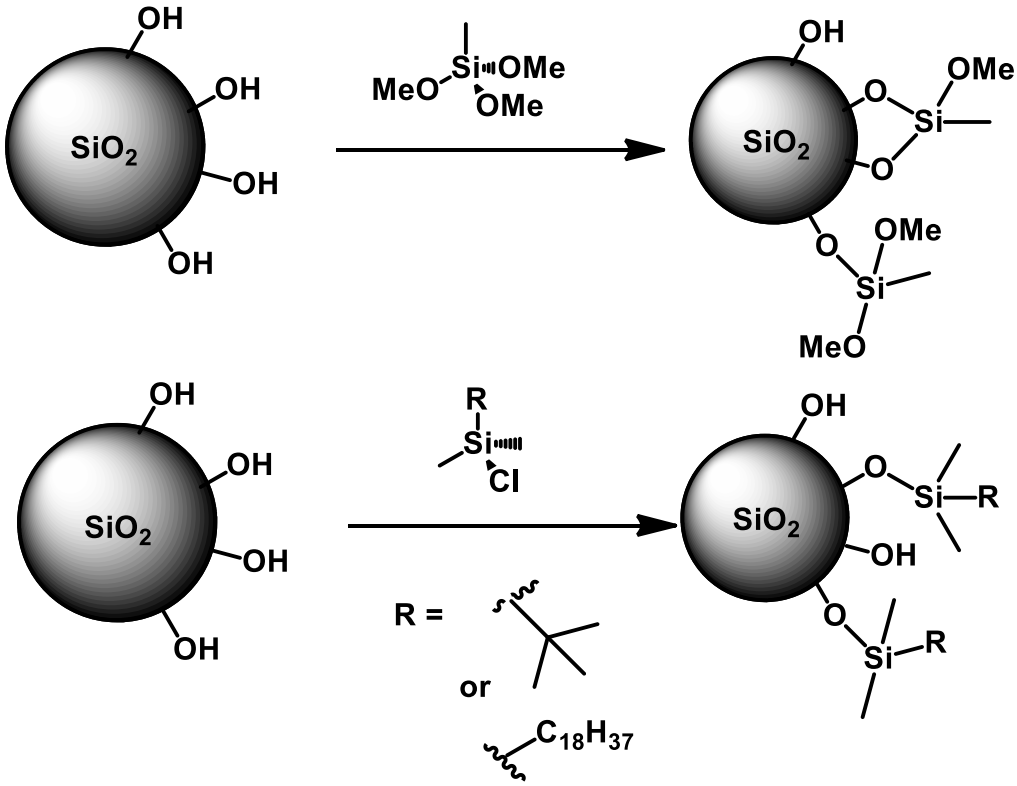

Figure 13. Functionalization of silica with chlorosilanes and alkoxysilanes.

The amount of alkyl-silane groups attached to the surface of the silica nanoparticles was too low to be detectable by ATR-IR spectrometry. However, elemental analysis and DLS measurements (reported in table 1) on water dispersions of functionalised silica showed relevant differences between the starting material and allowed to estimate the degree of functionalization.

Material	C%	Average hydrodynamic diameter
SiO_2	-	107.3 ± 0.9
SiO_2-Me	4.64	254 ± 9
SiO_2-tBu	4.06	191 ± 13
SiO_2-C_{18}	5.37	214 ± 3

Table 1. Elemental analysis and DLS measurements on different hydrophobic silica nanoparticles. From the top, commercial pristine silica Nps, methyl-modified silica NPs, t-butyl-modified silica NPs and octadecyl-modified silica Nps.

Surprisingly, the most hydrophobic material is the one functionalized with short alkyl chains. The first explanation of this result comes from the elemental analysis of nanoparticles. Indeed, if we convert the mass %C loading into a molar % loading of molecules by taking into account the number of C atoms per chain, we may

understand that the coverage of the surface is considerably higher in the case of SiO_2-Me (table 2).

Material	Molar %
SiO_2	-
SiO_2-Me	1.18-4.64*
SiO_2-tBu	0.67
SiO_2-C_{18}	0.26

Table 2. Results of elemental analysis converted into molar %. *Alkoxysilanes can substitute from 1 to 3 alkoxy groups, making it difficult to estimate the correct molar loading.

Other than the higher surface coverage, a higher molar loading corresponds to a lower number of hydroxyl groups left, the major responsible for the hydrophilicity of silica. For these reasons, methyl-modified silica nanoparticles were chosen as stabilizers for the following Pickering emulsion experiments.

Emulsification process

As described by the equation

$$G_{eq} = G_1 + G_2 + A_{12}\sigma_{12}$$

in order to produce a stable emulsion it is necessary to increase the total contact surface between the two phases A_{12}, overcoming the energy barrier imposed by the surface tension γ_{L-L}[10]. Different emulsification procedures have been reported in the literature ranging from the use of stirring devices to membranes or continuous-flow approaches. In this work, we compared 4 different approaches to emulsification: microtip sonication, homogenization, microfluidic mixing in a T-junction and an in-flow tube-in-tube device.

The first processing step is the dispersion of the stabilizer into the matrix phase, in our case water. This step is common for all the four dispersion methods that I considered. To this purpose, methyl-modified nanoparticles were dispersed in water by stirring overnight.

I started with sonication to disperse toluene droplets into the aqueous phase containing the stabilizer. The application of sound waves at high frequencies to a liquid-liquid system is able to overcome the energetic barrier of surface tension between the two phases (water and toluene) and form an emulsion. In the hope to further reduce the dimension of droplets, a microtip sonicator device was also used.

However, it turned out that emulsion suffers from extensive foaming due to the inclusion of air in the system. The concomitant formation of a dispersion of air droplets is due to the generation of hot spots by the microtip that leads to cavitation of the solvent. Moreover, microtip sonication only works on low amounts of liquid, so this method was dismissed.

The second approach uses a homogenizer as dispersing device. It consists of two concentric cylindrical parts: a central rotor and an external stator, shown in figure 14.

Figure 14. On the left, picture of the homogenizer. On the right, particular of the rotor-stator equipment.

The rotation of the internal part, combined with the static external portion generates high shear stress that is energetic enough to form droplets. By this procedure it was possible to emulsify large amounts of materials, reason for which it is largely employed in food and cosmetic industry. As for microtip sonication, part of the energy produced by shear stress is converted into heat, but without any cavitation effect.

Finally, two different custom-made microfluidic devices were employed for the generation of droplets. The first device was built by soft photolithography. Two parts compose it: a head that provides a convenient interface with the user pumping apparatus, and a body, which is the functional structure that contains the microfluidic channels. The head is made by flanged PTFE (polytetrafluoroethylene) tubing and glass slides. On the other hand, the body is made by glass slides and an epoxy-based resin (named NOA 81). Figure 15 shows a description of the structure of the device and the chemical structure of the epoxy resin.

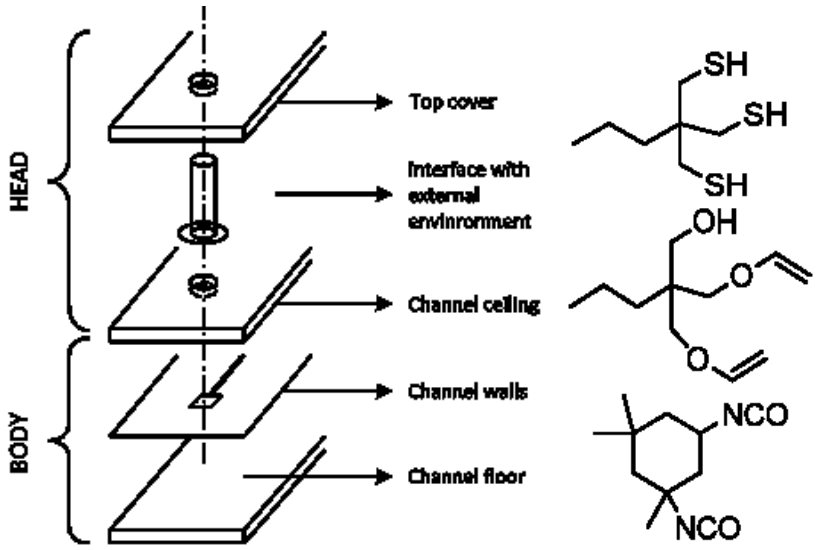

Figure 15. On the left, schematic representation of the device. On the right, components of NOA 81 resin.

The epoxy resin is sensitive to UV-light, so, using appropriate masks, it is possible to polymerize NOA (that solidifies) and remove the excess to obtain specific patterns. The mask used in this work is reported in figure 16. It was printed at high resolution (56kdpi) on a transparency sheet and used in the photo-polymerization of NOA.

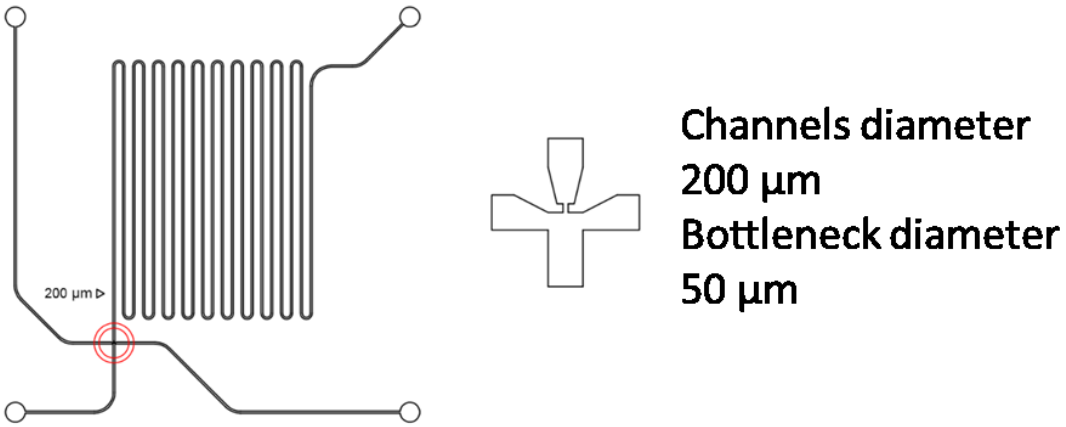

Figure 16. Mask design used in the preparation of the microfluidic junction. On the right, particular of the bottleneck of the 4 ways-junction (circled in red).

Referring to the 4 ways-junction shown in figure 16, the matrix phase with dispersed stabilizers is pumped through the two lateral channels, while the dispersed phase that will compose the droplets is pumped through the channel below.

It should be pointed out that the microfluidic device can be used to scale-up the production of Pickering emulsions both by collecting the outcome for a longer time or through parallelization of identical devices (i.e. via a numbering-up approach).

The second device designed had a tube-in-tube structure, shown in figure 17.

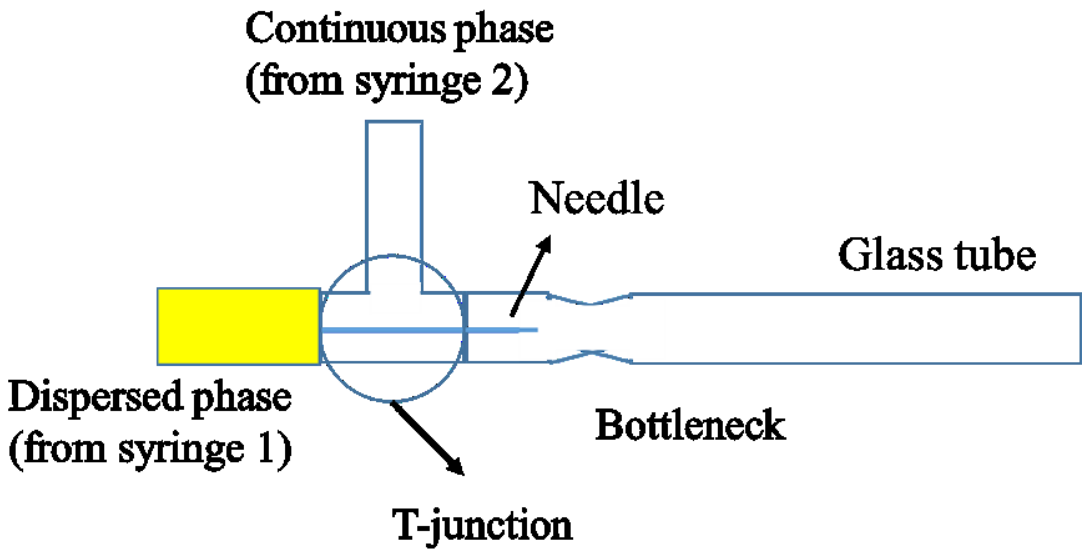

Figure 17. Design of the tube-in-tube device. The dispersed phase is pumped through a syringe needle directly near the bottleneck.

This device was made of a PTFE T-junction connected to a glass tube. The continuous phase was pumped through the side injector to ensure constant flow, while a stainless steel needle was inserted in the transversal injector. At the end of the needle, that protrudes inside the glass tube, a constriction was created to accelerate the flux of the carrier. Also in this case, the device generated a train of droplets that was carried away by the continuous phase, but the different geometry, with respect to the previous microfluidic device, has been studied recently by D. A. Weitz[26].

The emulsions were analysed with an optical microscope; droplets'size and dispersion, calculated from digital image analysis, are summarized in table 3.

Method	Average diameter of droplets
Microtip sonication	N. D.
Homogenization	34 ± 12 µm
4 ways-junction	17 ± 14 µm
Tube-in-tube	1 ± 0 mm

Table 3. Average diameter of droplets obtained with different methods.

The homogenization approach led to small droplets with an acceptable dimensional distribution. This process turned out to be suitable for the rapid production of large amounts of stable emulsions, so it was adopted to produce PE for further applications. On the contrary, for the low amounts of droplets produced, the two microfluidic approaches were discarded, despite the interesting peculiarities that the employment of both designs showed in the characteristics of the droplets. Indeed, by using the 4 ways-junction, we obtained smaller droplets than with the homogenizer, thanks to the precise design of the device, but the dimensional distribution was broader, probably due to the instability of very small droplets that accelerate coalescence and their random growth.

On the other hand, the droplets obtained with the tube-in-tube device were slightly bigger. Interestingly, during the generation of each single droplet, the dispersed phase adhered strongly to the steel surface of the needle, growing until the carrier flux was capable of removing it. Surprisingly, this fact had great effects on the size distribution of droplets, that were perfectly monodispersed. The results of the three methods are shown in figure 18.

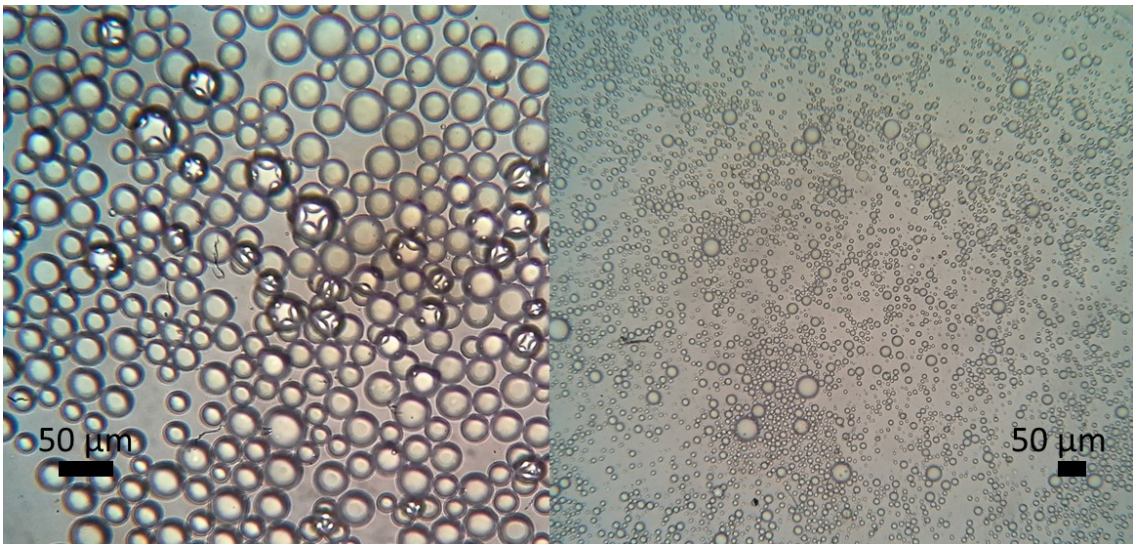

Homogenization 4 ways-junction

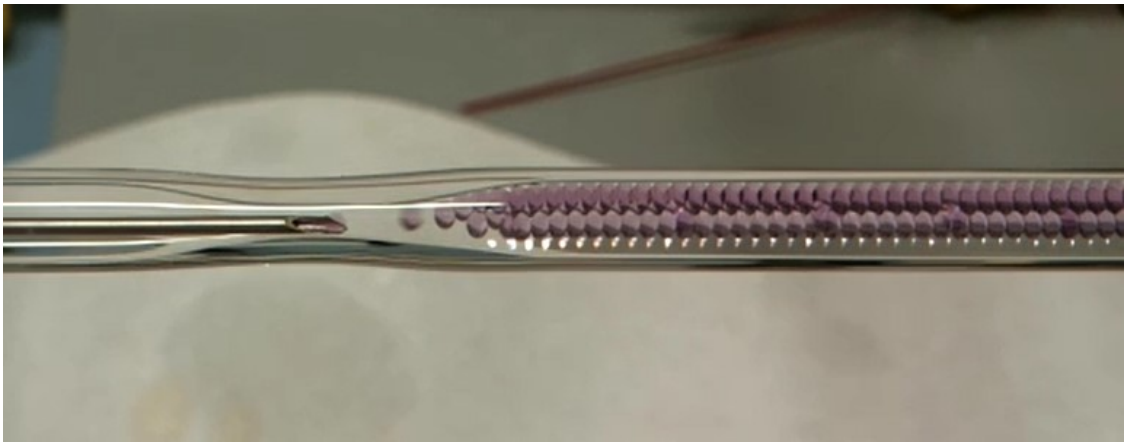

Tube-in-tube

Figure 18. In the previous page, optical microscope image of the emulsions obtained with the homogenizer (left) and with the 4 ways-junction (right); above, particular of the needle in the tube-in-tube device during the generation of stable droplets.

To further confirm the Pickering structure of prepared emulsions pristine silica nanoparticles were modified with fluorescein isothiocyanate and mixed with methyl-modified silica. The mixture was dispersed in water and emulsified with toluene to obtain a Pickering emulsion with fluorescent stabilizer. With the help of Doct. Ilaria Fortunati and Prof. Camilla Ferrante, the structure of this PE was analyzed at the confocal microscope.

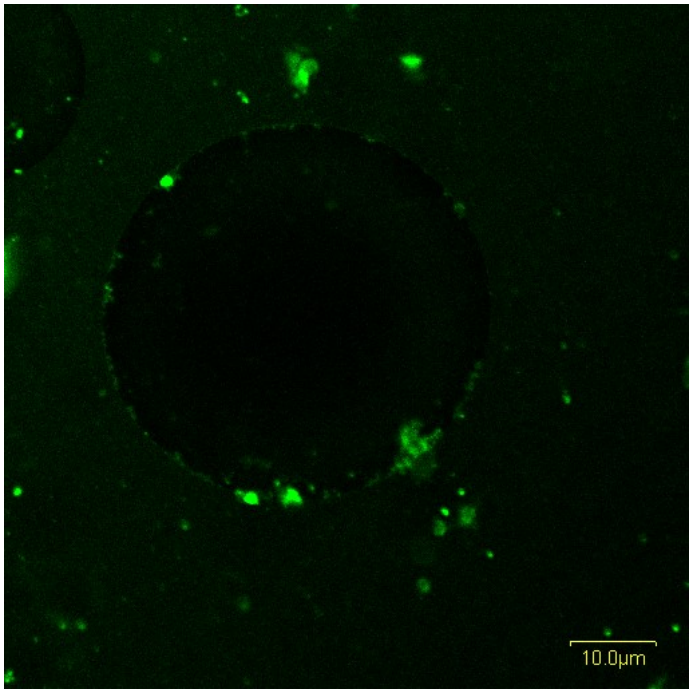

Figure 19. Confocal microscope image of a toluene droplet stabilized by fluorescent silica nanoparticles.

From the image in figure 19, the presence of a thin layer of nanoparticles all around the liquid-liquid interface can be confirmed, along with the presence of an excess of nanoparticles in the matrix phase that grants further stability to the system.

Pickering emulsions as microreactors for photocatalytic oxidations

Pickering emulsions have already showed interesting applications in the field of catalysis, especially for their biphasic nature and their ability to isolate different species into the droplets [27-29].

Preparation and characterization of a catalytic Pickering emulsion

The first step in the preparation of a catalytic Pickering emulsion is the design of the stabilizer that needs not only to have appropriate wettability properties and dimensions, but also to possess catalytic properties. Since the aim is the singlet oxygen photo-oxidation, the stabilizer must act as a photosensitizer for the production of singlet oxygen. At least three different strategies can be envisaged to this purpose: first, two different materials can be used, one with the correct wettability and the other with photo-sensitizing properties. This approach has potential problem coming from the fact that materials with different wettability will likely adsorb unequally at the liquid-liquid interface, complicating the rationalization of the results. A second strategy, is to functionalize nanoparticles with both the groups for contemporary tuning the wettability and the photocatalyst. A lot of research has been recently reported based on this strategy [30,31], but other than the problems connected to the control of multiple functionalization of a surface, a complete characterization of bi-functional materials proved to be an issue in many cases.

Probably the best approach is to conjugate the two moieties responsible for the two properties of interest (i.e. wettability and photocatalysis), into a single molecule that will be immobilized on the surface of the stabilizer. We decided to use [60]fullerene since it is both a well-known singlet-oxygen sensitizer and a hydrophobic molecule. Furthermore, the reactivity of [60]fullerene allows for the easy covalent immobilization on the surface of silica nanoparticles. This functionalization requires the synthesis of a fullerene derivative, N-(3-propyltriethoxysylil)-2-carbomethoxy-3,4-fulleropyrrolidine (FULP). The reaction scheme is shown in figure 20.

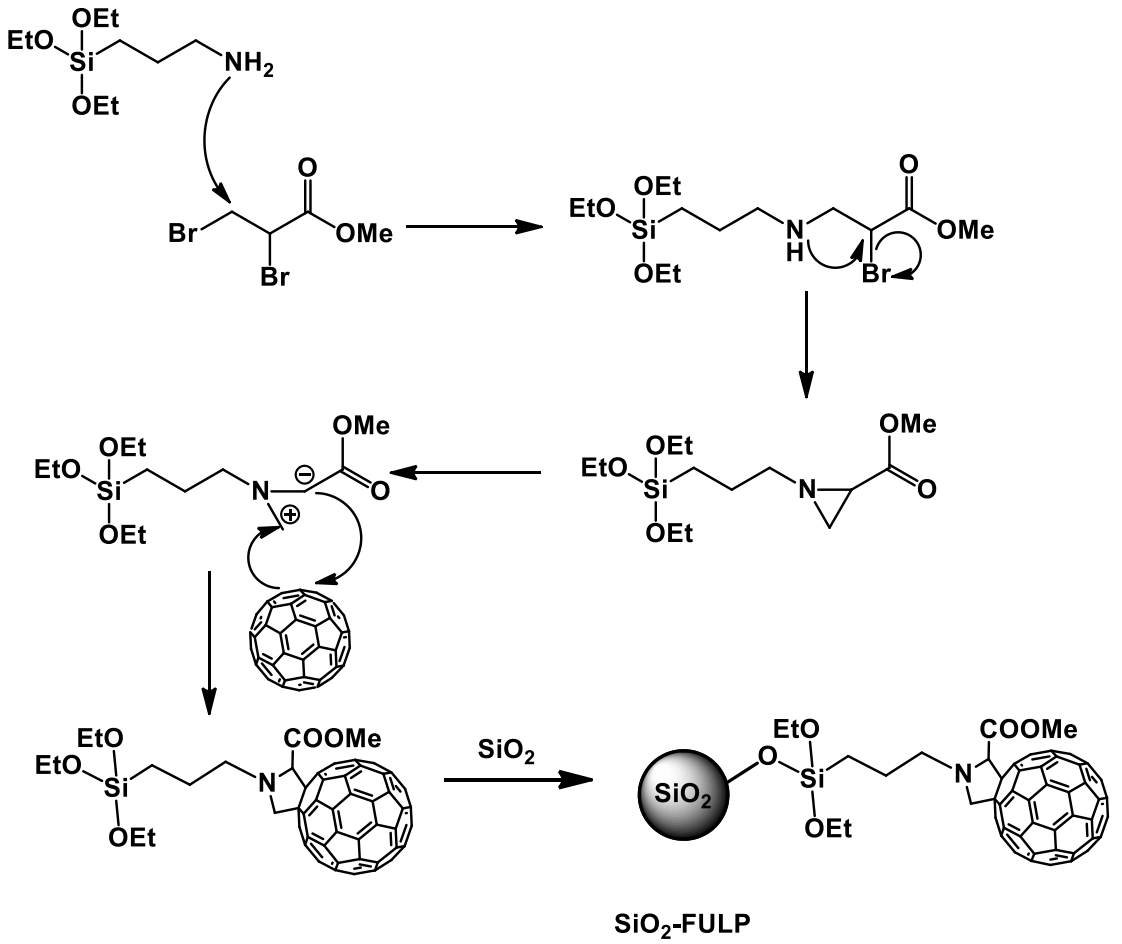

Figure 20. Functionalization of silica with [60]fullerene through the synthesis of a fulleropyrrolidine intermediate.

The synthesis of FULP starts from the preparation of the linker. The amino moiety of 3-aminopropyl triethoxysilane undergoes two nucleophilic substitutions with 2,3-dibromo propionate to an aziridine. This opens upon heating to give an azomethine ylide intermediate that reacts as a 1,3-dipole with a double bond of [60]fullerene to give the corresponding fulleropyrrolidine. A purification step by chromatography is required to remove unreacted fullerene and fullerene multiple adducts. After purification, thanks to the triethoxysilane functional group, FULP can be covalently linked to the surface of silica nanoparticles.

The obtained nanoparticles were dispersed in water and analyzed by DLS to verify the increased average hydrodynamic diameter upon functionalization. Table 4 reports the comparison between selected analytical data relative to SiO_2-FULP and pristine silica nanoparticles.

Material	C mass %	Average hydrodynamic diameter
SiO_2	-	107.3 ± 0.9
SiO_2-FULP	6.44	261 ± 12
SiO_2-Me	4.64	254 ± 9

Table 4. Comparison between silica-FULP and pristine silica nanoparticles.

As expected, silica-FULP has comparable hydrophobicity to methyl-modified silica.

A toluene-in-water Pickering emulsion stabilized by SiO_2-FULP nanoparticles was thereafter prepared, as reported in figure 21.

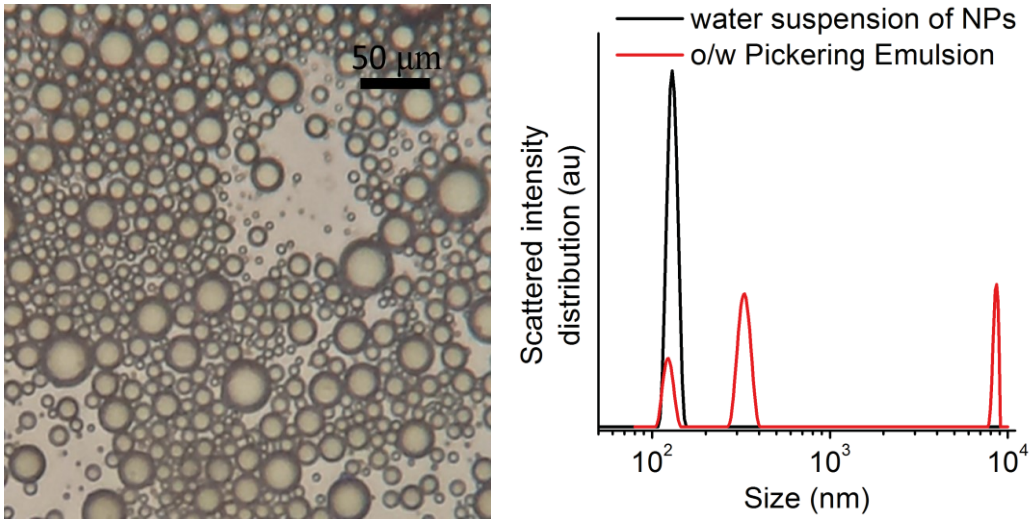

Figure 21. On the left, Pickering emulsion stabilized by SiO_2-FULP. On the right, DLS measurements of the dispersed stabilizer (black line) and the emulsion (red line).

The size diagram in figure 21 shows the narrow dimensional distribution of the dispersed stabilizer. Moreover, after the emulsification process two new peaks appeared that can be ascribed to the droplets (the one on the right, out of the detection range of DLS) and to aggregates of nanoparticles (in the middle).

Photocatalytic oxidation with singlet oxygen inside droplets

Whereas photooxidations with heterogeneous catalysts are widely studied[32-35], photooxidations in Pickering emulsions are still in their infancy. It is important to verify that the photo-oxygenation is really taking place inside the droplet rather than in the surrounding matrix. Since emulsions are biphasic systems, composed by two immiscible phases, complete immiscibility is an essential condition for the two liquids selected. In our case, water and toluene were chosen because they are sufficiently

immiscible to fulfil the first requisite. Second, the substrate must be soluble only in the toluene droplet so the photo-oxidation will necessarily take place exclusively inside the droplet. As model substrate we choose diphenyl-isobenzofuran (DIBF), a molecule with an extended conjugated system that can be detected by UV-Vis spectroscopy[36,37]. The oxidation of this substrate has been carried out in the presence of $^1O_2$, to give a colourless endoperoxide derivative. DIBF is slightly soluble in toluene, while it is totally insoluble in water. The oxidation mechanism is shown in figure 22. This substrate is highly hydrophobic so its leakage from the droplet can be ruled out. During the photoreaction, the PE is exposed to air, so both the aqueous continuous phase and the toluene droplets will be saturated with oxygen with the aqueous phase richer in oxygen due to its larger solubility with respect to toluene. As far as the sensitizer is concerned, singlet oxygen will be formed at the water-toluene interface and it has to migrate inside the toluene droplet in order to carry out the photo-oxidation of DIBF. Since as stated before, the system contains also some stabilizer dispersed in the matrix, not directly involved in the formation of the PE, one could argue that some singlet oxygen could be formed far from the water-toulene interface, and then migrate inside the droplet. However, I may exclude this contribution since the migration of singlet oxygen is limited by its extremely short lifetime[38,39].

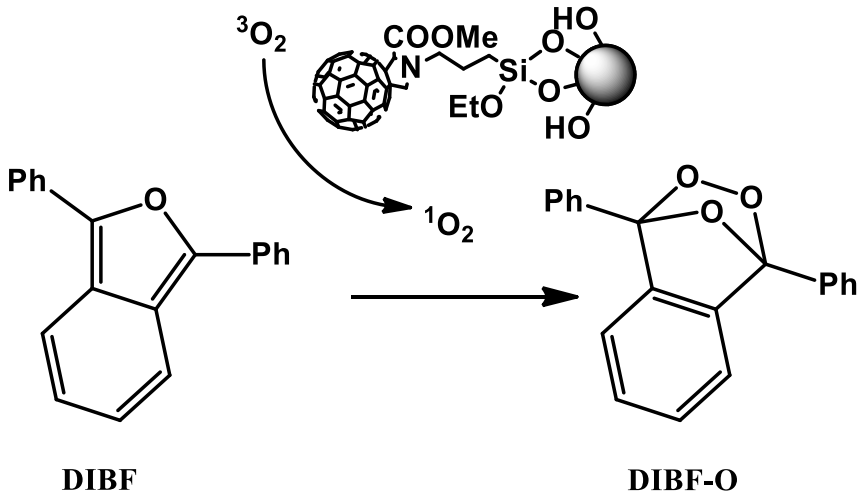

Figure 22. Oxidation mechanism of DIBF in presence of SiO_2-FULP

The reaction was performed both inside the droplets of a toluene-in-water PE and in the traditional conditions of heterogeneous catalysis, where the catalyst was just dispersed into the reaction mixture containing only toluene as a solvent. A graphic representation of the differences between the two processes is shown in figure 23. The volumetric mass percentage of catalyst and the concentration of the substrate were kept constant throughout the experiments.

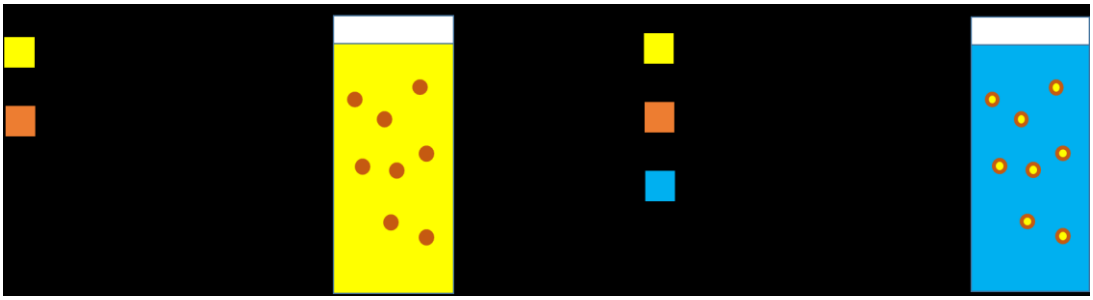

Figure 23. Scheme of traditional heterogeneous photooxidation (on the left) and photooxidation inside PE (on the right).

In the case of traditional heterogeneous catalysis, SiO_2-FULP nanoparticles were dispersed in toluene before the addition of the substrate in dark conditions. Then mixture was poured into a glass reactor (figure 24) and illuminated with white leds for 75 minutes. Samples taken at fixed times were filtered and analyzed by UV-Visible spectroscopy.

Figure 24. Image of the reactor for photocatalytic oxidations.

For the experiments in PE, DIBF was first dissolved in toluene in dark and SiO_2-FULP was dispersed in water. Then two phases were emulsified by homogenization and loaded into the photo-reactor and illuminated for 75 minutes. Samples were taken at fixed times and centrifuged to separate the phases. The supernatant was collected and filtered for UV-Visible analysis.

From absorbance spectra of the fractions I could obtain the concentration curve plotted against the reaction time. The comparison between the two processes is shown in figure 25.

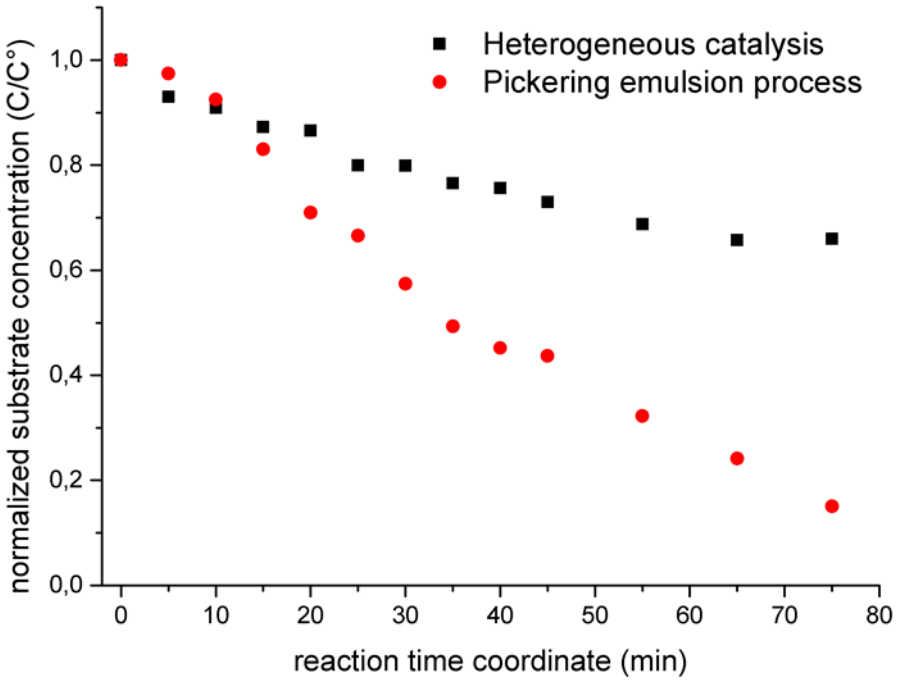

Figure 25. Concentration of DIBF as function of reaction time for the two processes. In black, traditional catalysis; in red, the process into the droplets of a Pickering emulsion.

This graph supports the fact that the reaction inside the PE proceeds faster than under traditional conditions. In order to rationalize this behaviour we carried out a modelization of the kinetic curve according to two following consecutive steps[37]:

a) Generation of $^1O_2$ at the toluene-water interface:

$$^3O_2 \xrightarrow{FULP} {}^1O_2$$

b) DIBF oxidation by singlet oxygen:

$$DIBF + {}^1O_2 \rightarrow DIBF(O_2)$$

Assuming this second reaction to be first order for both DIBF and singlet oxygen, it is possible to write the kinetic equations that describes the oxidation mechanism.

$$\frac{d[DIBF]}{dt} = -k_2[{}^1O_2][DIBF]$$

$$\frac{d[{}^1O_2]}{dt} = k_1[FULP][{}^3O_2] - k_2[{}^1O_2][DIBF] = k_1'[{}^3O_2] - k_2[{}^1O_2][DIBF]$$

$$\frac{d[\,^3O_2]}{dt} = -k_1[FULP]\left[\,^3O_2\right] + h \cdot a \cdot \Delta C^*_{O_2}$$

The term $h \cdot a \cdot \Delta C^*_{O_2}$ represents the O_2 mass transfer through the triphasic (oxygen-water-toluen) system. h is the permeability of the system towards oxygen, a parameter that depends on the Henry's constant. a is the specific surface between air and the matrix phase. $\Delta C^*_{O_2}$ is the deviation from the Henry's equilibrium concentration of oxygen in water. This parameter is equal to 0 in the case of traditional heterogeneous catalysis, but becomes relevant in the presence of a second mass transfer through the liquid-liquid interface, that perturbs the equilibrium state.

An analytical solution of the above equations proved to be complicated, therefore some assumptions were made to simplify the system of equations. First, the activity of fullerene as a sensitizer is high enough to be able to excite immediately oxygen to the singlet state. Second, as suggested by Henry's constants for oxygen in water and in toluene[40], the mass transfer through the water phase is faster than the liquid-liquid transfer. Third, the reaction occurs at the toluene-water interface. With these three assumptions we can determine that the kinetically determinant step is the generation of $^1O_2$.

We can also assume that the high reactivity of activated oxygen species allows the instantaneous oxidation of DIBF, so $\left[\,^1O_2\right]$ can be considered at a steady state during the process. With these considerations the kinetic equation for the oxidation of DIBF becomes the following

$$\frac{d[DIBF]}{dt} = -k_2'[DIBF]$$

which can be integrated to give the equation

$$\frac{[DIBF]}{[DIBF]_0} = e^{-k_2't} = e^{-\frac{t}{\tau}}$$

This last equation allows the direct analysis of the spectrometric data and the calculation of τ, a parameter that describes the mass transfer phenomena. Fittings performed with equation obtained were in compliance with the curves' trends of repeated experiments (the parameter R^2, always > 0.98, certified the good quality of fittings, shown in figure 26).

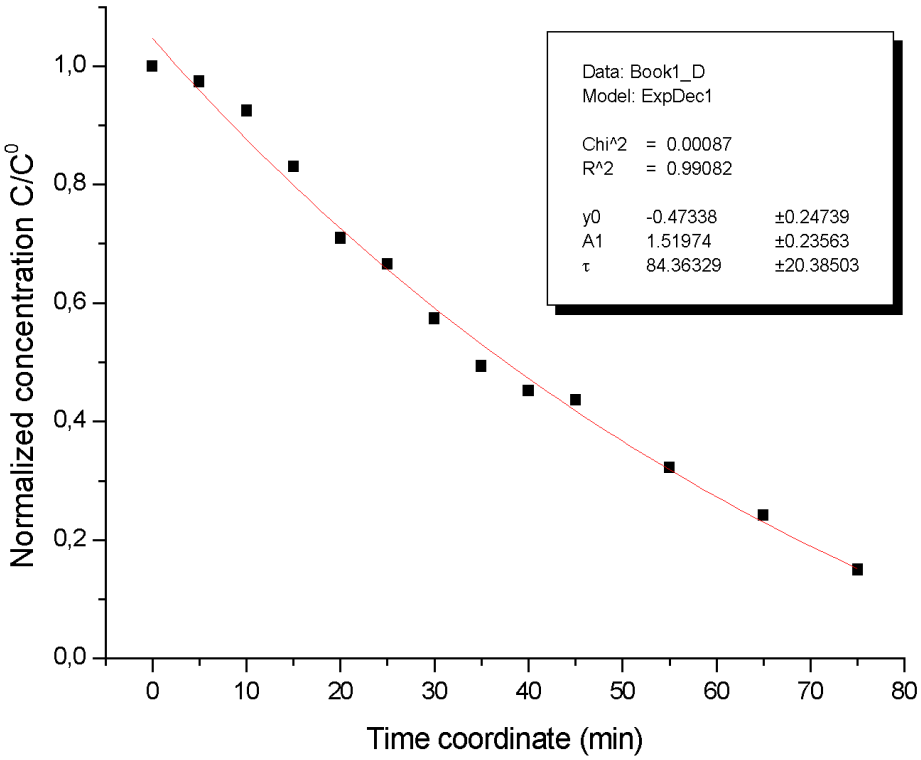

Figure 26. Exponential fitting of the curve obtained from UV-Visible spectra.

Pickering emulsion-based sensor for triacetone triperoxide detection

Compartmentalization of reagents into Pickering emulsions

As reported in the introduction part of this chapter, Pickering emulsions can be used for the confinement of chemical reactions and biological processes for new high-tech applications. In particular, different aqueous reagents can be compartmentalized and kept separated within the water drops of an emulsion, a strategy that living systems use to process multistep cascade reactions in a one-pot fashion[41]. In particular, we wished to use different Pickering emulsions to store separately the reagents for the detection of acetone described before, namely glycine, sodium nitroprusside and basic phosphate buffer, which would slowly evolve to an acetone insensitive system if mixed all together. That would allow to preserve their detection performances until the use when, under a mechanical stimulus that disrupt the PEs, the reactants are allowed to mix. The easiest way to achieve complete separation is the storage of each compound into an ad-hoc prepared “box”, a system that does not allow any mutual interaction. Recently, new methods for the isolation of reagents have been

developed, adsorption and encapsulation for examples. These strategies allow not only the isolation of the content, but also release of the same as a consequence of an external specific stimulus. This ability gives to these approaches the name “smart”. To include Pickering emulsions into the “smart” category, a PE-based system to control reactive species and release them by using a specific stimulus was studied.

In a first approach, I analyzed the isolation of hydrochloric acid and sodium hydroxide inside PE droplets. I prepared two different water-in-toluene Pickering emulsions using diluted HCl and NaOH as dispersed phase, stabilized with methyl-modified silica. To visualize the different droplets I added a small amount of Congo Red dye during the emulsification process. The two PEs, nameley the acidic one with blue droplets dispersed in toluene and the basic one with red droplets, were poured into a vial through a lamination process to obtain a layered structure as the one shown in figure 27.

Figure 27. Picture of the two water-in-toluene PEs after lamination. The red layer is made of aqueous NaOH droplets, the blue layer is made of aqueous HCl droplets. Toluene, the matrix phase, is present as supernatant.

No change in the layered structure was observed for several weeks on standing, or even after gentle shacking of the vial thus confirming the stability of PEs and the possibility to isolate separate reagents inside the droplets.

PE-based pen sensor

The use of compartmentalized reagents requires to overcome some issues regarding both stability and feasibility. To address the stability issue, it is necessary to verify that reagents trapped in the aqueous phase does not mix as the result of their solubility in the dispersing phase. In our case, the three reagents, sodium nitroprusside, glycin and the phosphate buffer were insoluble in the organic phase. Related to the feasibility issue, it is necessary to excogitate a procedure to disrupt on demand the PEs containing the separated reagents. Of course, this procedure should be easy and without requiring an expensive apparatus or necessitating of electrical powering. Generally speaking, it is possible to disrupt a Pickering emulsion in three ways. One way could be the addition of a third solvent, miscible with both the dispersed and the continuous phase. In this case, surface tension between the phases is reduced and the emulsion collapses. A second possibility is to increase the temperature of the system, in order to desorb the stabilizer from the liquid-liquid interface. This method requires energy to overcome the Gibbs free energy of adsorption of nanoparticles.

$$\Delta F_{ads} = -\pi r^2 \gamma_{L-L}(1 - |cos\theta_w|)$$

After desorption, emulsions become unstable so droplets are subjected to coalescence. Both the above approaches are impractical for in-field use.

The approach I preferred, exploits mechanical stimuli to break droplets in situ, through the use of an empty ballpoint pen commercially available which is originally designed to load inks and dyes used for artworks. As matrix phase, isooctane was used rather than toluene; this modification was dictated to avoid the employment of solvents with low vapour pressure. Figure 28 shows the working principle of this design.

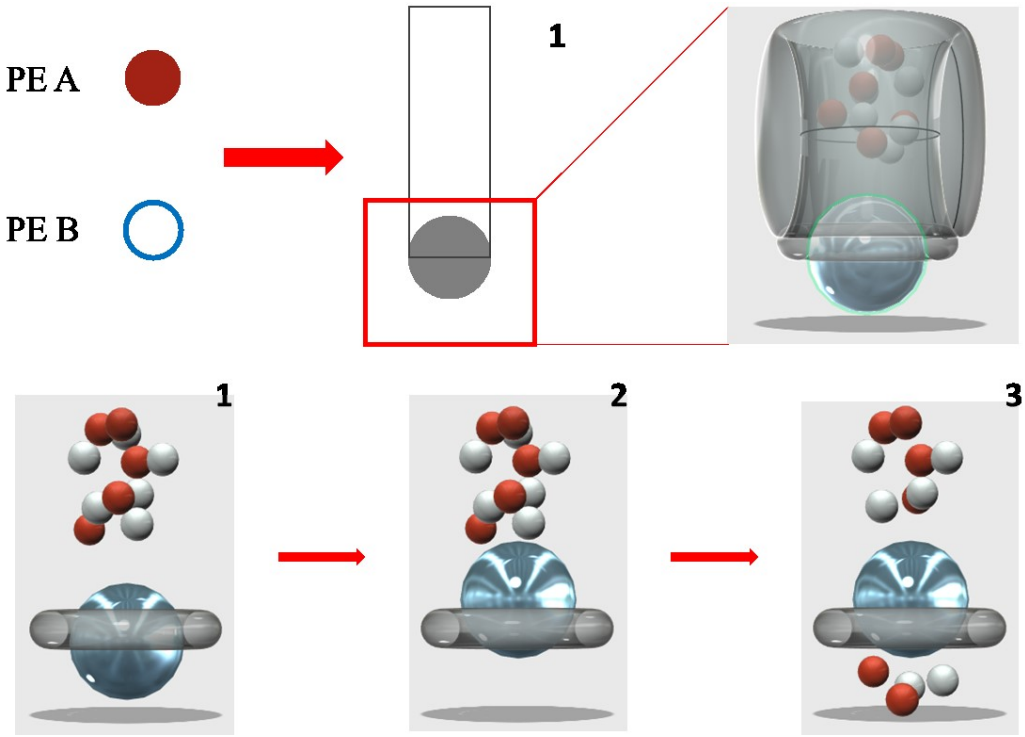

Figure 28. Scheme of the working principle of the Pickering pen sensor. Red spheres represent solution A (sodium and glycin in water), white spheres represent solution B (phosphate buffer).

After preparation, the two water-in-isooctane Pickering emulsions stabilized with methyl modified silica nanoparticles were gently mixed inside the ballpoint pen reserve as showed in step 1. When the pen is used to draw a sign by pressing it against a filter paper, the metal sphere on the tip of the pen goes up, like in step 2, and the content leaks out as shown in step 3 and the friction produced enough mechanical stimulus to disrupt the PEs and mix the reagents. The filter was immediately exposed to acetone vapours and the typical purple coloration appeared after about 20 seconds.

To confirm the efficacy of the new design, the pen sensor was tested with diluted water solutions of acetone, from 10% to 0,1% in weight, in order to estimate a lower detection limit. The pen was used to draw on paper strips that were exposed to acetone vapours coming from different solutions. The strips are shown in figure 29.

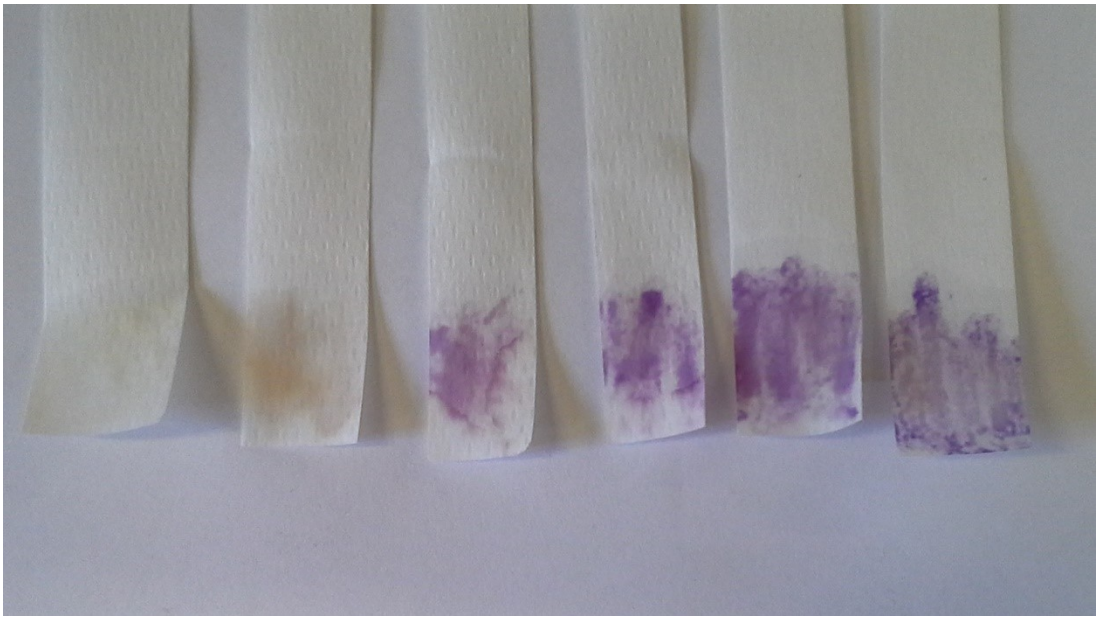

Figure 29. Paper strips used for the test on (from left to right) pure water, 0.1%, 0.5%, 1%, 5%, 10% solutions of acetone.

The test confirmed to be effective even for low concentration of analytes. Furthermore, the pen is an easy-to-use device that requires no specific skill to be employed.

Conclusions

In this work, I studied the properties of Pickering emulsions and their application in photocatalysed oxidation with singlet oxygen and as a stable system for the compartmentalization of reagents and the detection of acetone, a component of TATP explosive. To this purpose, I prepared and characterized different stabilizers in order to modify the wettability of silica nanoparticles by covalent functionalization. I studied the emulsification process and compared several devices to produce Pickering emulsions with long term stability.

The acquired knowledge was employed to apply the PE structure to photocatalysis, by investigating a model oxidation with singlet oxygen that occurred inside the droplets. I functionalized silica with a C_{60}-fullerene derivative to obtain a material with the characteristics of being both a good stabilizer for emulsions and a sensitizer for the generation of singlet oxygen. The templating properties of PEs were exploited to cover the surface of toluene droplets with this catalyst, and the generation of singlet

oxygen into the same droplets was indirectly recorded monitoring the oxidation of a model substrate, diphenyl isobenzofuran.

Collected data from repeated experiments were employed to compare the Pickering emulsion approach to a more traditional “in-flask” heterogeneous photocatalysis. Results shows an increasing in the reaction speed, probably due to the concentration of the catalyst, caused by the adsorption of nanoparticles, near to the substrate and to the improved mass transfer of oxygen through a biphasic system.

Furthermore, the stability of Pickering emulsions allowed to confine reactive molecules inside droplets, limiting their interaction with the external environment. These characteristics makes PE suitable to store chemicals in safe compartments until the necessity to use. I exploited this ability to prepare a Pickering-based pen sensor for acetone detection. The high stability of PE allowed to keep sodium nitroprusside and phosphate buffer separated and stable until use, simply by drawing on a filter paper and exposing the filter to the vapours of the analyte. Moreover, the design of the system can be optimized for the detection of different chemicals entities as reported in table 5.

Test	Ingredients	Detected substances
Simon’s test	Sodium nitroprusside, Basic buffer, acetaldehyde	Amines
Urine standard test	Sodium nitroprusside, Basic buffer, keton	Amines
Marquis’ test	Formaldehyde, Sulfuric acid	Amines (specific)
Liebermann’s test	Potassium nitrite, Sulfuric acid	Cocaine, Morphine, PMA, PMMA
Froehde’s test	Molybdic Acid, Sulfuric acid	Alkaloids
Mandelin’s reagent	Ammonium metavanadate, Sulfuric acid	Alkaloids
Mecke’s reagent	Selenous acid, Sulfuric acid	Alkaloids

Table 5. List of tests with similar working mechanism.

I verified the efficacy and the reliability of the pen sensor analysing different diluted acetone samples, and I am working to further improve the stability and the rheological properties of the two Pickering components.

Experimental part

Preparation and characterization of Pickering Emulsions

Functionalization of silica Nps with silanes

Commercial silica **Np**s (1g) were dispersed in toluene (50 mL) by sonication, then triethylamine (**TEA**, 1.4 mL, 10 mmol) and silane (10 mmol, table below) were added to the dispersion and left under reflux overnight. The final mixture was centrifuged and resuspended several times in toluene to eliminate the excess of reagents, then dried under vacuum.

Reagent	C% loading of Nps from elemental analysis
Methyl-trimethoxy silane	4.64
t-butyl-dimethyl-chlorosilane	4.06
n-octadecyl-dimethyl-chlorosilane	4.37

Preparation of microfluidic junction for droplet generation

The mask design was printed on a transparent acetate sheet. Two glass slides were drilled in correspondence of the tubing entrance and exit, washed several times with detergent solution and isopropanol and dried under nitrogen flux. These two slides were glued together, with flanged PTFE tubes (external diameter 2.1 mm, internal diameter 1.5 mm) in between as shown in the figure below, using NOA 81 resin, to prepare the head of the reactor.

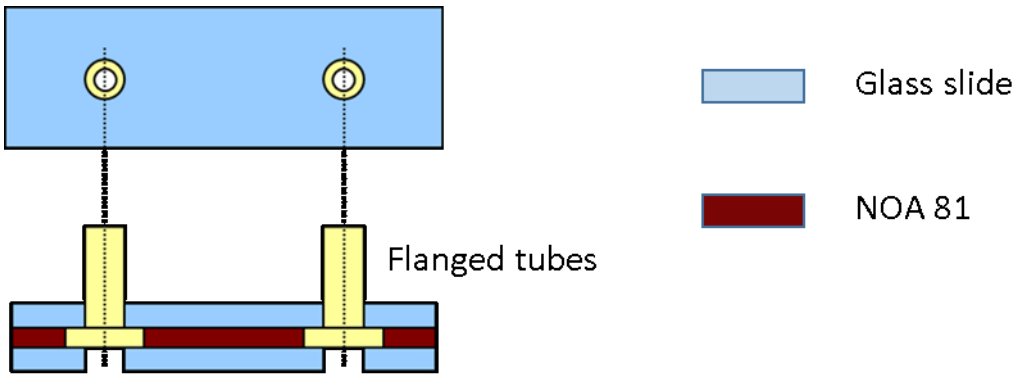

To avoid occlusion, smaller PTFE tubes (external diameter 1.6 mm, internal diameter 0.5 mm) were fitted inside the larger tubes with the purpose to seal them. NOA 81 polymerization was performed using UV light (365 nm) for 60 seconds. Excess of NOA was removed after the polymerization and the head was irradiated for other 30 minutes. After irradiation it was put on a heating plate set at 50°C and left curing overnight.

The next day, a third glass slide was washed as described previously. 4 small square pieces of filter paper (3 mm thick) were soaked in NOA and glued to the 4 corners of the glass slide. NOA resin was poured on the third glass slide, avoiding the formation of bubbles, then the head was assembled on the NOA layer. The weight of the head is enough to eject the excess of resin, while the pieces of filter paper ensure the thickness of the channel. The reactor was put inverted, with the head down, and the mask was fixed at the body (figure below).

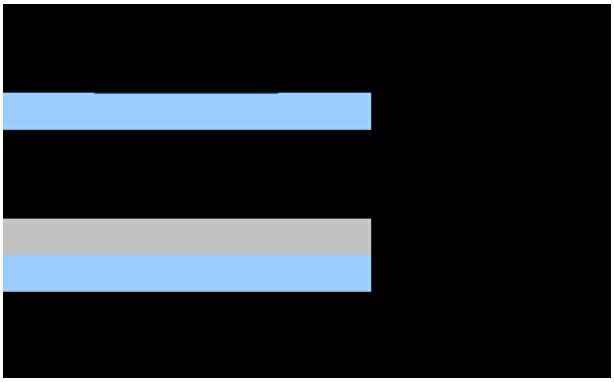

NOA 81 was polymerized under UV light for 60 seconds, then the mask and the smaller tubes were removed and the channels emptied from the non-polymerized resin by connecting tubes to vacuum. After the removal, keeping one tube connected to vacuum, the other tubes were connected to a beaker containing ethanol to clean the channels with this solvent. Ethanol washing was alternated with small aliquots of 1:3 acetone:water solution (acetone is responsible of swelling phenomena, so it has to be used carefully).

After channel washing, the reactor was cured at 50°C overnight before using.

Preparation of toluene-in-water Pickering Emulsion

Functionalized silica nanoparticles (3% w/v respect to the total volume toluene+water) were first dispersed in water by three different procedures, namely: ultrasonication, microtip sonication, and magnetic stirring. Magnetic stirring overnight was choosen as the best method to disperse the materials. Then toluene (10% v/v) was added and the Pickering emulsion was formed with different devices (sonication, magnetic stirring, in-flow devices, homogenizer).

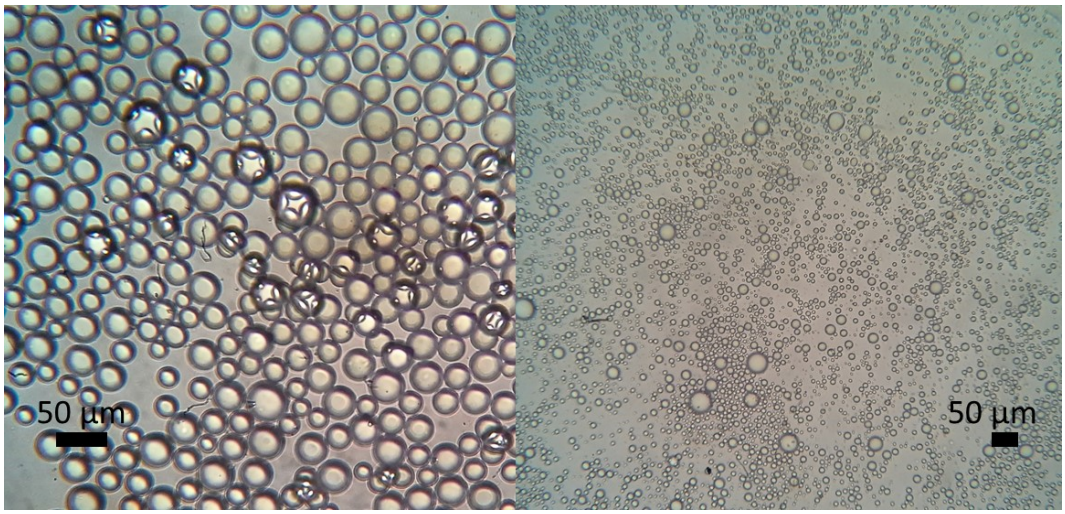

Homogenization 4 ways-junction

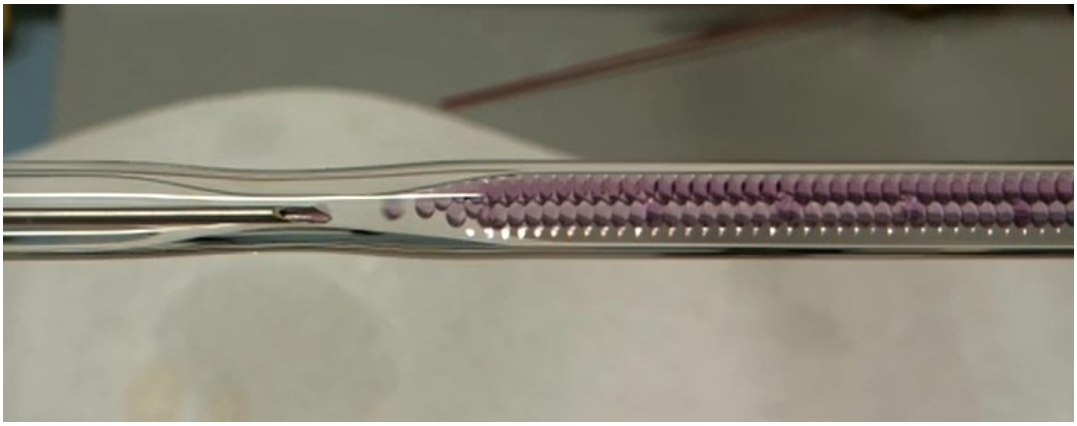

Tube-in-tube

Pickering emulsions obtained with different emulsification processes. Upper pictures were taken in an optical microscope. The picture below was taken with a common mobile phone.

Functionalization of silica Nps with fluorescein isothiocyanate (FITC)

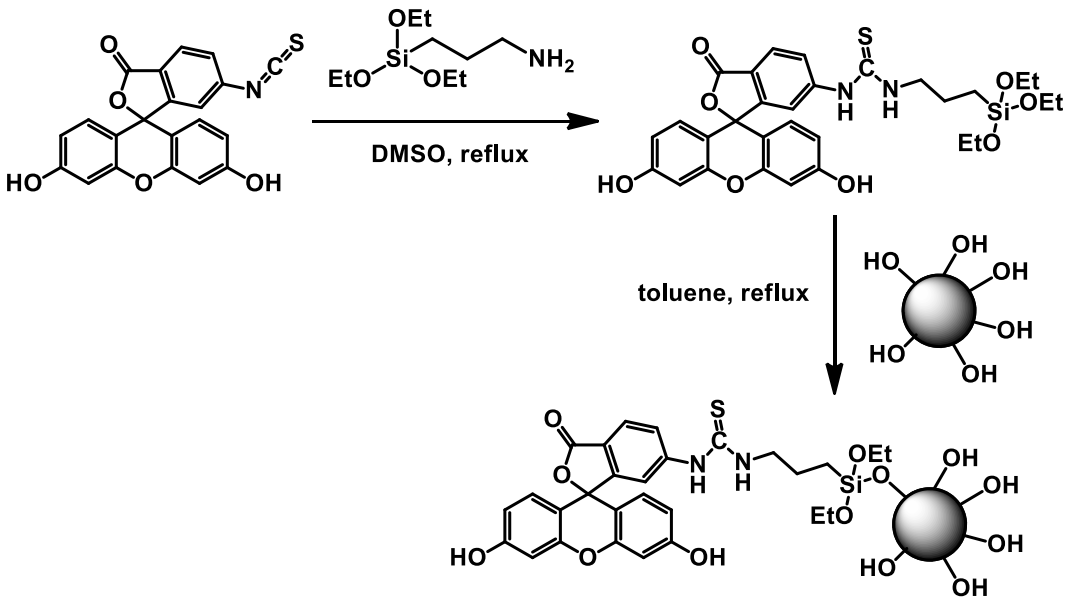

FITC (10 mg, 0.025 mmol) was dissolved in 10 mL of DMSO in dark under N_2. Then APTES (6 µL, 0.025 mmol) was added to the solution and the mixture was magnetically stirred in dark overnight. Then SiO_2 Nps (60 mg) were dispersed in 20 mL of toluene and added to the above mixture. The reaction was refluxed for 6 hours, then stirred overnight at room temperature under N_2. The product was recovered by centrifugation and suspended in fresh toluene several times, then dried under vacuum.

Preparation of toluene-in-water fluorescent PE

Me-modified Si Nps (2.8 % w/w respect to water) and fluorescent Si Nps (0.6 % w/w respect to water) were dispersed in 90 mL of water by stirring overnight. Then toluene (10% v/v) was added and emulsified using the homogenizer.

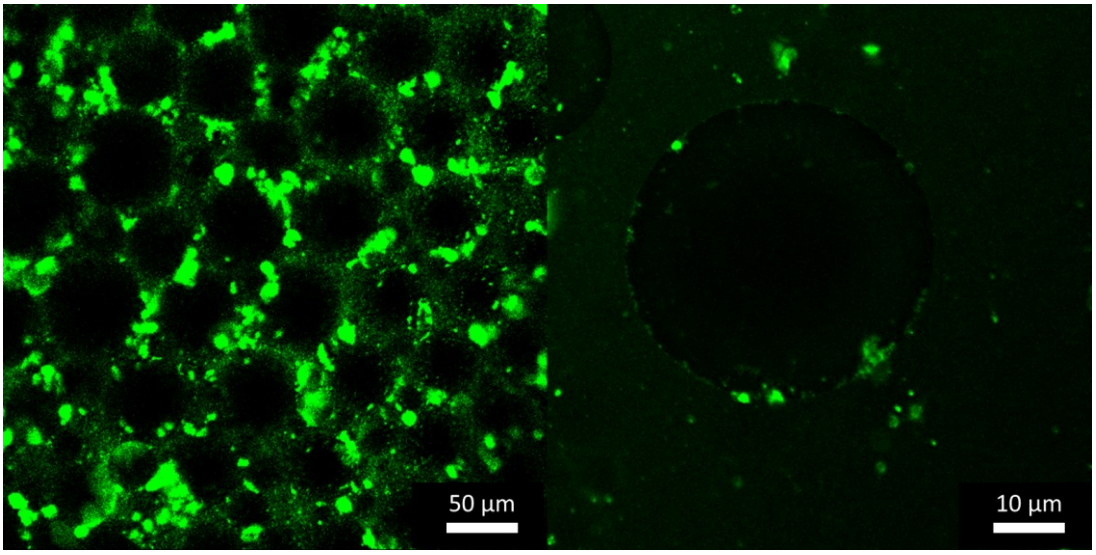

Images of PE stabilized with fluorescent SiO_2 nanoparticles. On the right, particular of a single droplet.

Preparation, characterization and application of catalytic Pickering Emulsions

Synthesis of methyl-2,3-dibromopropionate

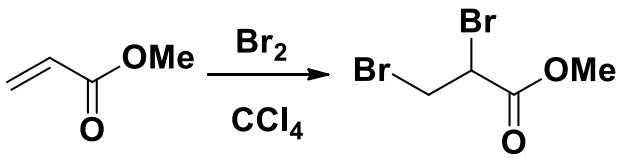

Methyl methacrylate (11.2 mL, 124.4 mmol) was dissolved in 35 mL of anhydrous CCl_4. The solution was cooled below 5°C and bromine (6.5 mL, 126.6 mmol) was added dropwise and the reaction was stirred for 2 hours. The volatiles were removed under vacuum, then the residue was solubilized with toluene and dried again for several times for further purification.

Yield: 29 g (95%)

^{1}H-NMR (250 MHz, $CCl_4/CDCl_3$), δ (ppm): 3.66 (dd, J = 4.4 Hz, J = 9.9 Hz, 1H, -CH), 3.83 (s,3H, $-OCH_3$), 3.91 (dd, J = 9.8 Hz, J = 11.3 Hz, 1H, $-CH_2$), 4.43 (dd, J = 9.8 Hz, J = 11.3 Hz, 1H, $-CH_2$).

NMR and mass spectra are reported at the end of the chapter for clarity.

Synthesis of N-(3-propyltriethoxysilyl)-2-carbomethoxy aziridine

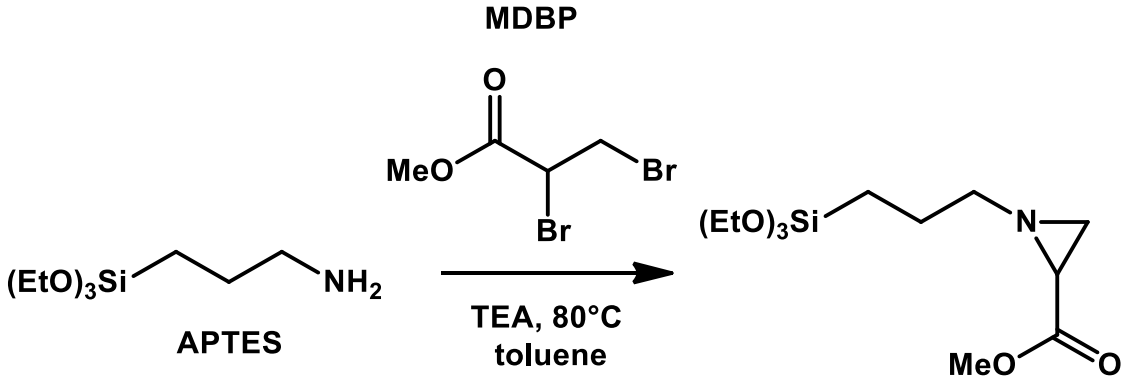

Methyl-2,3-dibromopropionate (MDBP, 1.0 mL, 8.0 mmol) was dissolved in anhydrous toluene (1.0 mL) at 5-10°C under N_2 atmosphere. A mixture of N-(3-aminopropyl)triethoxysilane (APTES, 2.0 mL, 8.0 mmol), triethylamine (TEA, 2.4 mL, 17.0 mmol) and 5.0 mL of anhydrous toluene was added dropwise in about 20 minutes. Then the solution was slowly heated up to 80°C. After 2 hours, the crude was filtered through a celite filter, dried under vacuum and stored in the fridge.

Yield: 1.8 g (75%)

^{1}H-NMR (200 MHz, $CDCl_3$), δ (ppm): 0.61-0.63 (m, 2H, CH2Si), 1.24 (t, J = 8 Hz, 9H, CH_3), 1.62 (m,1H, NCH_2CH), 1.73 (m, 2H, CH_2), 2.05 (m, 1H, NCH_2), 2.18 (m, 1H, CH), 2.35 (NCH_2CH_2), 3.74 (s, 3H, OCH_3), 3.84 (q, J = 8 Hz, 6H, OCH_2).

^{13}C-NMR (200 MHz, $CDCl_3$), δ (ppm): 8.19, 18.49, 23.06, 34.74, 37.38, 52.37, 58.59, 63.85, 171.60.

GC-MS ($C_{13}H_{27}NO_5Si$, MM = 305 g/mol) m/z: 305 [M^+], 218 [M-$CH_2CHCOOMe$-H], 163 [$Si^+(OEt)_3$].

NMR and mass spectra are reported at the end of the chapter for clarity.

Synthesis of N-(3-propyltriethoxysilyl)-2-carbomethoxy-3,4-fulleropyrrolidine (FULP)

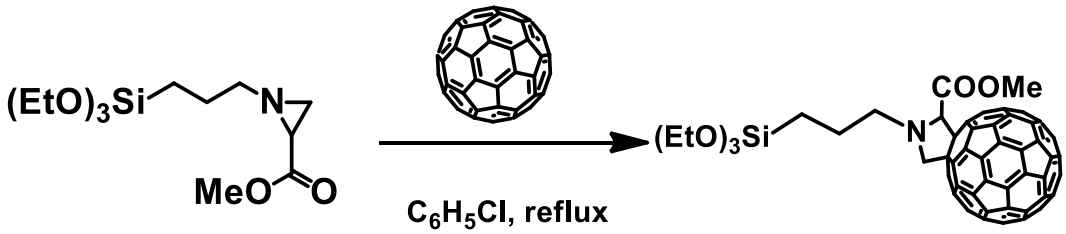

C60-fullerene (100 mg, 0.13 mmol) was dissolved in 100.0 mL of chlorobenzene. Then **1** (170 mg, 0.56 mmol) was added to the mixture and refluxed for 38 hours (TLC: silica on aluminum; eluent: toluene:ethylacetate/9:1, Rf fullerene = 1, Rf product = 0,7). The solution was concentrated under vacuum and the desired product was isolated through preparative column chromatography (silica; eluent: toluene to recover unreacted fullerene, toluene:etilacetato/9:1 to isolate the product). The fractions containing compound **2** were concentrated and the product precipitated with acetonitrile. After washing with acetonitrile through centrifugation, the product was dried under vacuum and stored in the fridge.

Yield: 210 mg (37%)

^{1}H-NMR (200 MHz, CS_2-$CDCl_3$), δ (ppm): 0.69 (m, 2H, CH_2Si), 1.28 (t, J = 8 Hz, 9H, CH_3), 2.02 (m, 2H, CH_2), 2.97 (m, 1H, NCH_2), 3.30 (m, 1H, NCH_2), 3.84 (s, 3H, OCH_3), 3.89 (q, J = 8 Hz, 6H, OCH_2), 4.33 (d, J = 8 Hz, 1 H, NCH_2C_{60}), 5.09 (d, J = 8 Hz, 1 H, NCH_2C_{60}), 5.10 (s, 1H, $NCHC_{60}$).

^{13}C-NMR (200 MHz, CS_2-$CDCl_3$), δ (ppm): 8.46, 18.81, 22.23, 51.81, 54.96, 58.59, 65.06, 69.56, 72.71, 77.27, 126.97, 135.79, 136.50, 137.00, 138.23, 140.00, 140.19, 140.49, 140.56, 142.08, 142.11, 142.25, 142.36, 142.42, 142.59, 142.65, 142.93 142.99, 143.39, 144.73, 144.78, 144.89, 144.94, 145.32, 145.58, 145.68, 145.75, 145.94, 146.16, 146.31, 146.39, 146.57, 147.55, 147.64, 151.86, 154.48, 155.17, 155.48, 170.34.

GC-MASSA ($C_{73}H_{27}NO_5Si$, MM = 1025 g/mol) m/z:1025 $[M]^+$, 965 [M-$COOCH_3$-H].

NMR and mass spectra are reported at the end of the chapter for clarity.

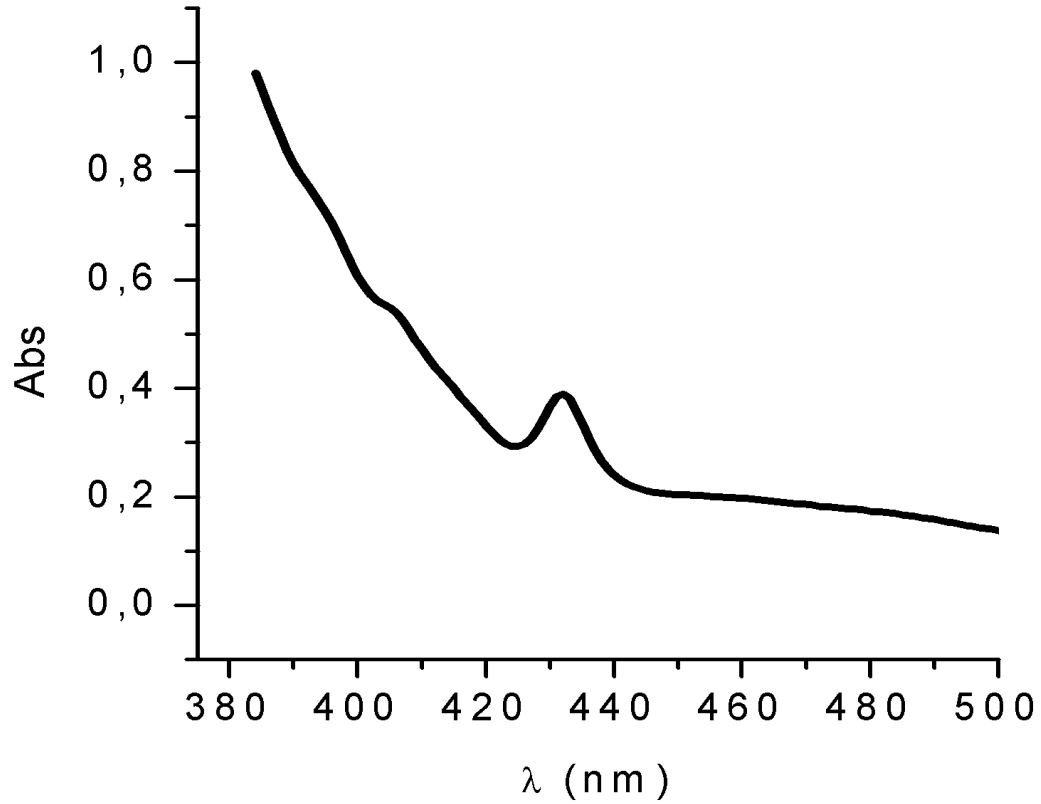

Particular of the UV-Visible spectrum of FULP. The peak at 430 nm is characteristic of the compound.

Functionalization of silica Nps with fulleropyrrolidine (FULP)

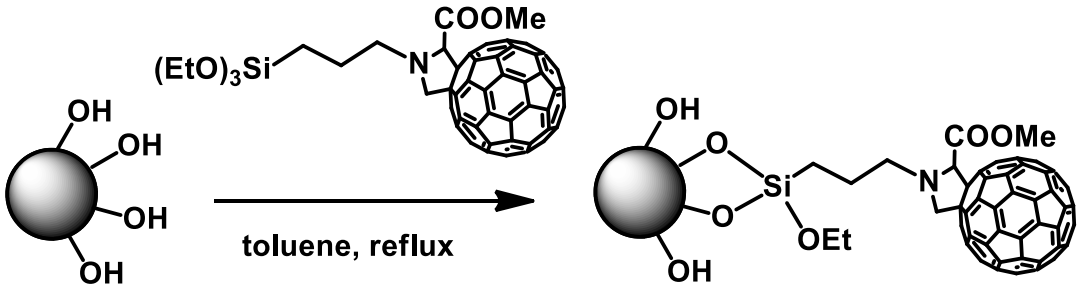

Commercial silica **Np**s (1 g) were dispersed in toluene (50 mL) by sonication, then **2** (50 mg, 0.05 mmol) was added to the dispersion and refluxed under stirring for 48 hours. The desired product was recovered by centrifugation and suspended several times with toluene to eliminate the excess of reagents, then dried under vacuum.

C% loading (determined by elemental analysis): 6.44%

Oxidation with singlet-oxygen by heterogeneous catalysis

FULP-silica **Np**s were dispersed in 100 mL of toluene (0,04% w/w) overnight. Then 1,3-diphenyl-isobenzofuran (**DIBF**, 150 mg, 0.55 mmol) was added to the dispersion and dissolved under N_2 flux in dark. The mixture was poured into the photo-reactor and gently stirred under illumination with white LEDs for 90 minutes. Samples were collected at fixed times and filtered to eliminate the solid catalyst. 10 µL of each sample were diluted to 1 mL with toluene in a UV-Vis quartz cuvette for the analysis.

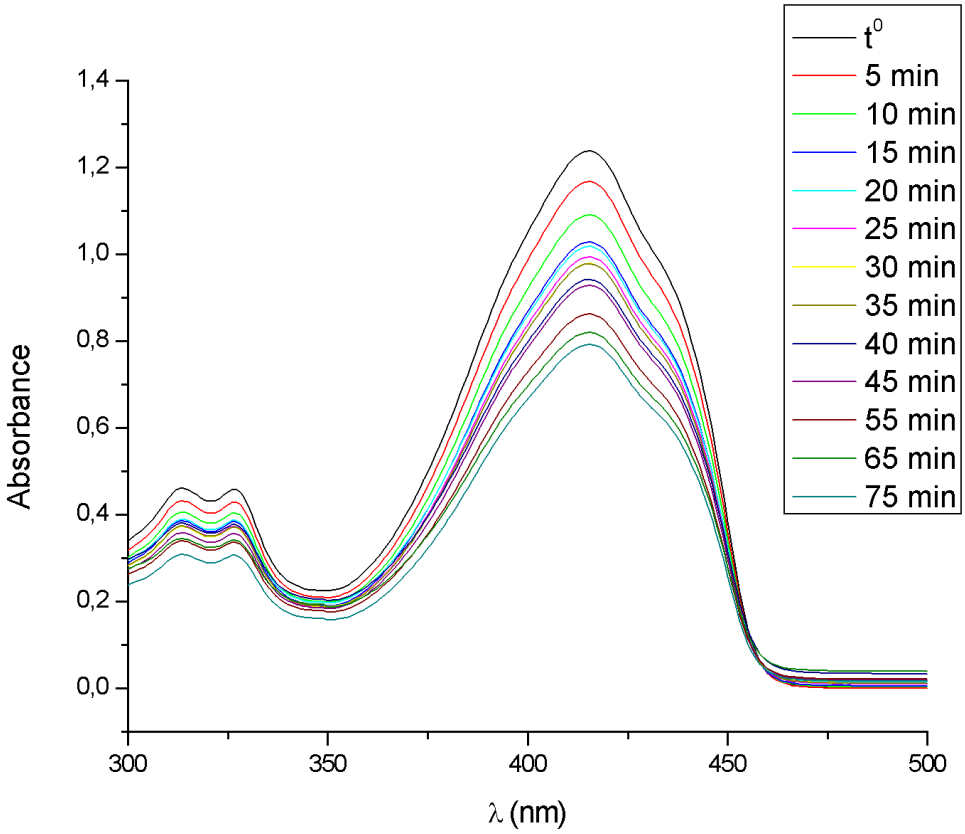

Concentration of DIBF monitored during the reaction by UV-Visible spectroscopy.

Preparation of catalytic Pickering emulsions

FULP-silica **Np**s were first dispersed in water (0,04% w/v respect to the total volume toluene+water) overnight. Then **DIBF** (15 mg, 0.055 mmol) was dissolved in 10 mL of toluene (10 mL) and added to the above aqueous suspension. PE was prepared using the homogenizer and stored in dark under N_2 until used.

Oxidation with singlet-oxygen: catalysis in Pickering emulsion droplets

Catalytic **PE** (50 mL) was loaded into the reactor, gently stirred and illuminated for 90 minutes. Samples were collected at fixed times; the dispersed phase containing the substrate was separated by centrifugation (10000 rpm, 5 minutes) and filtered to eliminate the solid catalyst. 10 µL of each sample were then diluted to 1 mL with toluene in a UV-Vis quartz cuvette for the analysis.

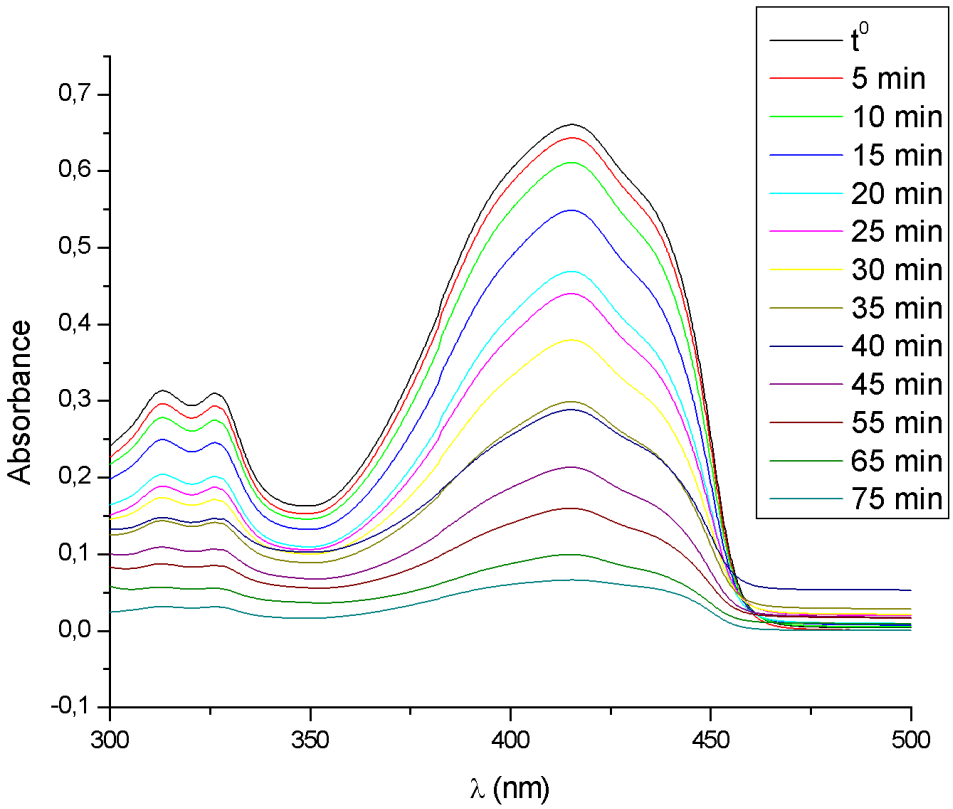

Concentration of DIBF monitored during the reaction by UV-Visible spectroscopy.

Pickering emulsion based pen-sensor

Preparation of solution A

Sodium nitroprusside (3% w/w) was dissolved in 30 mL of water by sonication. Then glycine (1.33 g, 17.7 mmol) was added to the solution and dissolved.

Preparation of solution B

Na_3PO_4 (1.62 mg, 9.9 mmol) and Na_2HPO_4 (0.62 mg, 4.4 mmol) were dissolved in 16.7 mL of milliQ water by sonication and immediately diluted at the desired concentration.

Traditional test

Two drops of solution A were poured on a filter paper. Immediately, two drops of solution B were poured on the spot and the filter was exposed to acetone vapours for 30 seconds. The colour turned to purple in few seconds.

Preparation of PE A

Me-modified silica Nps (see page 45) (variable amount for different experiments: from 0.5 to 3% w/w respect to the total amount iso-octane + water) were dispersed in 70 mL of iso-octane by stirring overnight. Then 30 mL of solution A were added to the suspension and emulsified using the homogenizer.

Preparation of PE B

Me-modified silica Nps (see page 45) (variable amount for different experiments: from 0.5 to 3% w/w respect to the total amount iso-octane + water) were dispersed in 70 mL of iso-octane by stirring overnight. Then solution B was diluted at different ratios (1/1; 1/2; 1/5; 1/10, total volume: 30 mL) and added to the dispersion. The mixture was emulsified using the homogenizer.

Preparation and use of PE based pen-sensor

15 mL of PE A and 15 mL of PE B were poured into the ballpoint pen using a funnel. The pen was then gently shaked to intimately mix the two emulsions, and used to draw on a piece of filter paper. The drawing was exposed to acetone vapours for 30 seconds.

References

1. S. Roohinejad, *Food Hydrocolloids*, **2019**, 87, 307.
2. P. Sarkar, *Environmental Chemistry Letters*, **2018**, 16, 1, 59.
3. S. Guido, *Advances in Colloid and Interface Science*, **2018**, 256, 305.
4. A. L. Yarin, *Advances in Colloid and Interface Science*, **2018**, 252, 21.
5. K. Von Neergaard, *Zeitschrift für die Gesamte Experimentelle Medizin,* **1929**, 66, 373.
6. R. Pattle, *Nature* **1955**, 175, 1125.
7. C. C. Macklin, *Lancet,* **1954**, i, 1099.
8. J. A. Clements, *American Journal of Physiology*, **1956**, 187, 592.
9. S. U. Pickering, *Journal of Chemical Society*, **1907**, 91, 2001.
10. Y. Chevalier, *Colloids and Surfaces A: Physicochemical and Engineering Aspects*, **2013**, 439, 23.
11. Y. Chevalier, *Journal of Colloid and Interface Science*, **2010**, 351, 348.
12. B. P. Binks, *Langmuir*, **2000**, 16, 8622.
13. B. P. Binks, *Journal of American Chemical Society*, **2014**, 137, 3, 1362.
14. M. Selke, *Journal of Materials Chemistry*, **2004**, 14, 487.
15. H. W. Kroto, *Nature*, **1985**, 318, 162.
16. M. Maggini, *Journal of American Chemical Society*, **1993**, 115, 9798.
17. D. Citterio, *Analytical Chemistry*, **2002**, 74, 5766.
18. J. Lin, *Trends in Analytical Chemistry*, **2000**, 19, 541.
19. *US Patent* 2,990,253, June 27, **1961**.
20. *US Patent* 4,147,514, April 3, **1979**.
21. H. L. Pardue, *Analytical Chemistry*, 65, **1993**, 1903
22. T. A. Turney, *Journal of Inorganic and Nuclear Chemistry*, **1961**, 18, 179.
23. L. T. Zuravlev, *Colloids and Surfaces*, **2000**, 173, 1.
24. T. Bein, *Microporous and Mesoporous Materials*, **2010**, 132, 60.
25. G.D. Pirngruber, *Microporous and Mesoporous Materials*, **2005**, 85, 111.
26. D. A. Weitz, *Angewandte Chemie International Edition*, **2011**, 50, 1648.
27. V. Nardello-Rataj, *Chemistry*, **2012**, 18, 14352.
28. I. J. van Hest, *Angewandte Chemie*, **2012**, 124, 10904.
29. V. Nardello-Rataj, *Angewandte Chemie International Edition*, **2015**, 54, 2006.
30. W. Wu, *Journal of Materials Chemistry*, **2012**, 22, 23181.
31. W. Wu, *Physical Chemistry Chemical Physics*, **2012**, 14, 13914.
32. J. R. Aranzaes, *Angewandte Chemie International Edition*, 44, **2005**, 7852.
33. A. T. Bell, *Science*, 299, **2003**, 1688.
34. M. Misono, *Chemical Rewievs*, 98, **1998**, 199.
35. W. J. Thomas, *Principle and Practice of Heterogeneous Catalysis*, Wiley-VHC, book.
36. D. R. Kearns, *Journal of American Chemical Society*, **1975**, 97, 462.
37. M. L. Wolbarsht, *Journal of American Chemical Society*, **1974**, 96, 3343.
38. D. R. Kearns, *Journal of American Chemical Society*, **1972**, 94, 1031.
39. C. S. Foote, *Journal of American Chemical Society*, **1983**, 105, 3423.
40. A. Schumpe, *Journal of Chemical and Engineering Data*, **1989**, 34, 251.

41. B. P. Binks, *Journal of American Chemical Society*, **2015**, 137, 1362.

NMR and mass spectra

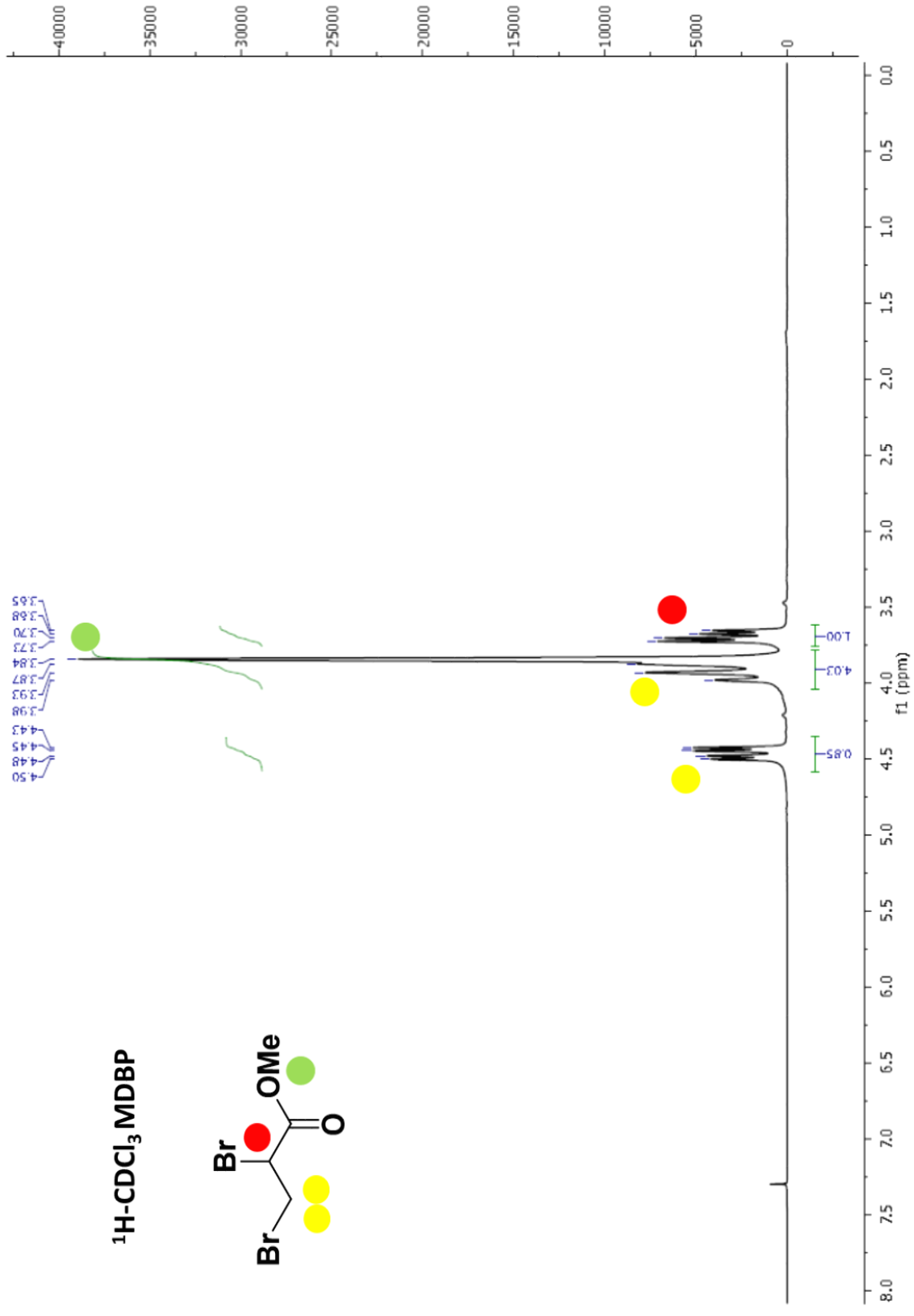

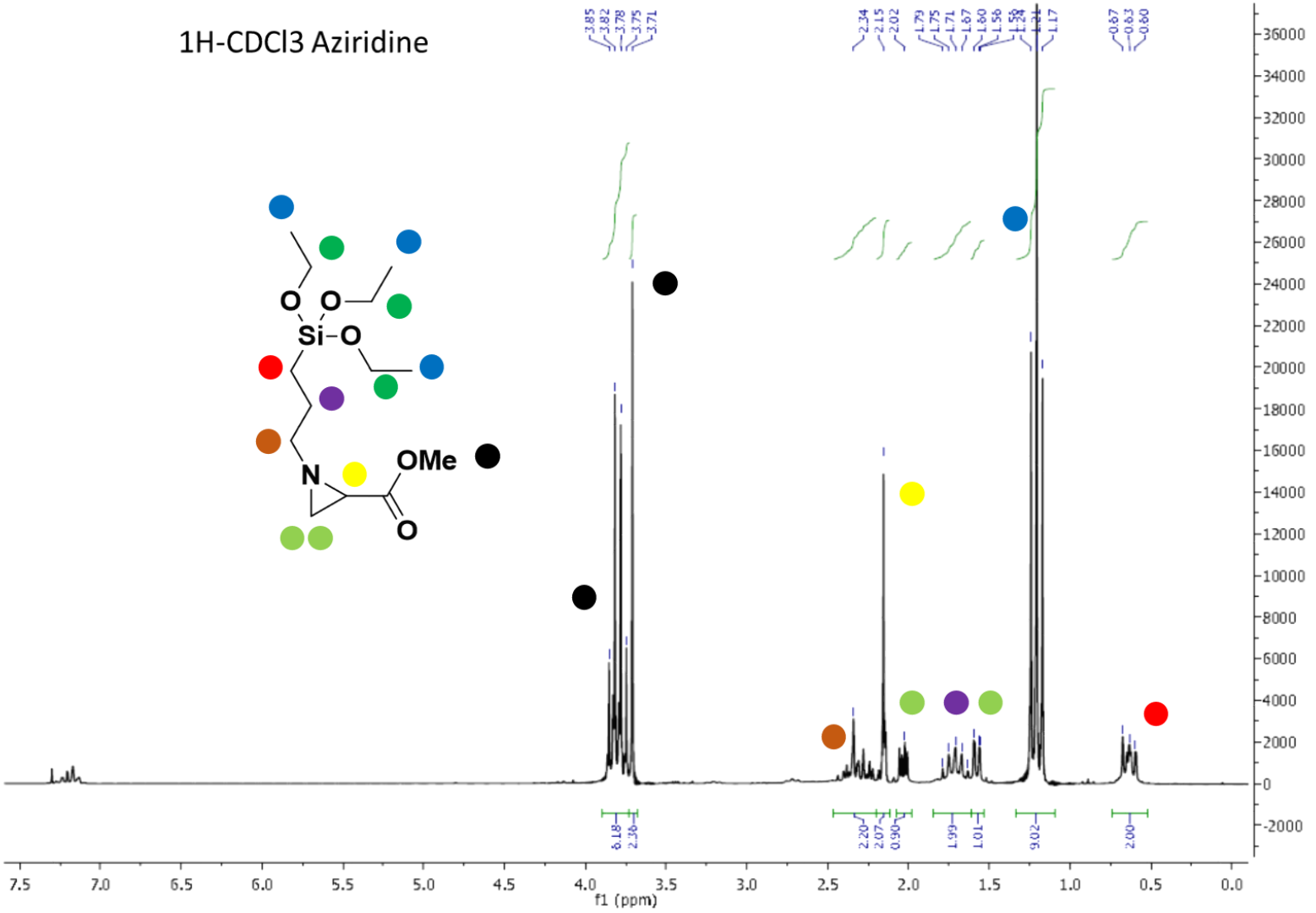
1H-CDCl3 Aziridine
O
O
Si–O
N
OMe
O
3.85
3.82
3.78
3.75
3.71
2.34
2.15
2.02
1.79
1.75
1.71
1.67
1.60
1.56
1.17
0.67
0.63
0.60
9.18
2.36
2.20
2.07
0.90
6.97
7.01
9.02
2.00
f1 (ppm)

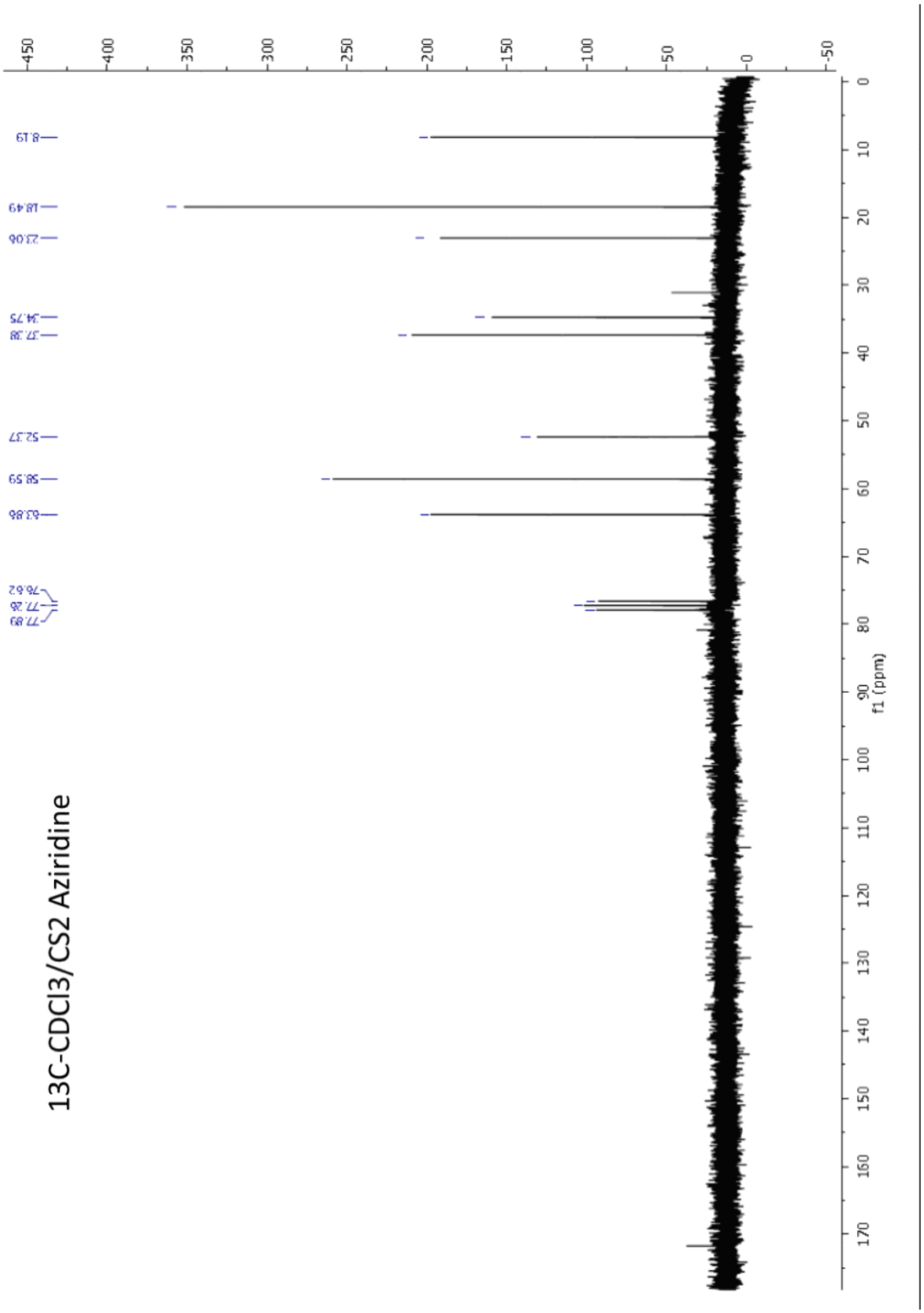
13C-CDCl3/CS2 Aziridine
8.19
18.49
23.06
34.75
37.38
52.37
58.59
63.86
76.62
77.26
77.89
f1 (ppm)

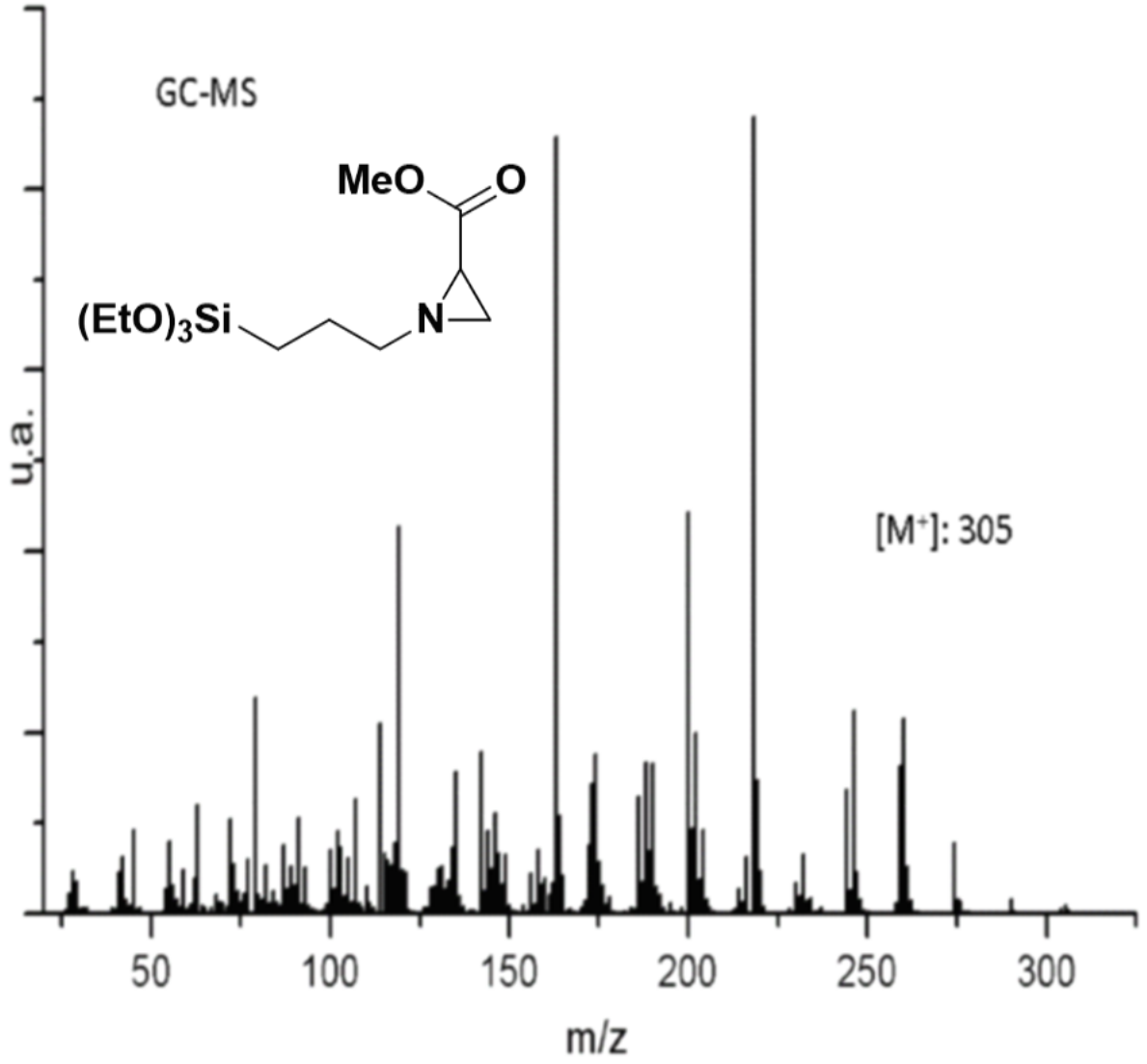
GC-MS
MeO
O
(EtO)3Si
N
u.a.
[M+]: 305
50
100
150
200
250
300
m/z

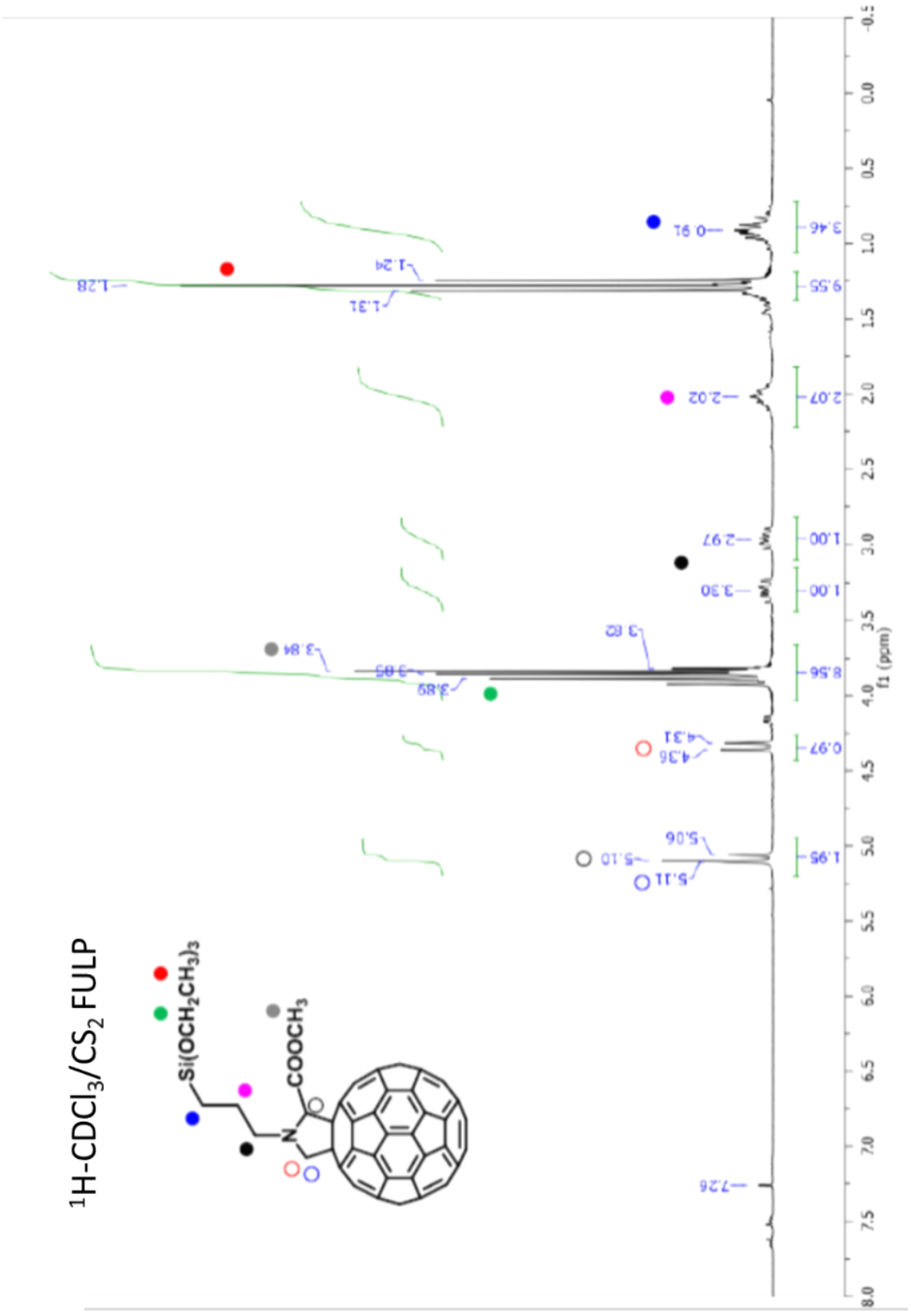
^{1}H-CDCl$_3$/CS$_2$ FULP
Si(OCH$_2$CH$_3$)$_3$
COOCH$_3$
N
f1 (ppm)

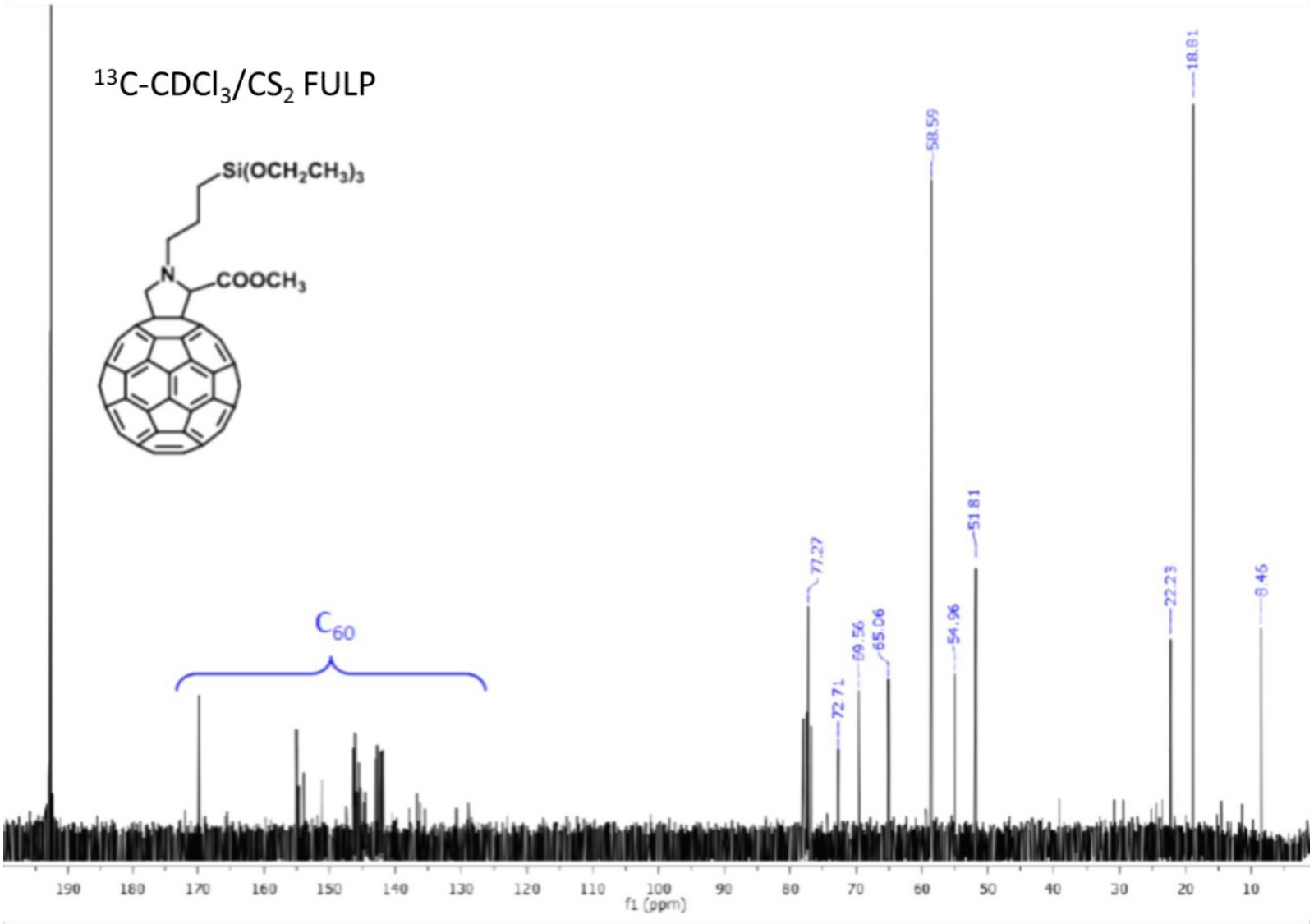
^{13}C-CDCl$_3$/CS$_2$ FULP
Si(OCH$_2$CH$_3$)$_3$
N
COOCH$_3$
C$_{60}$
77.27
72.71
69.56
65.06
58.59
54.96
51.81
22.23
18.81
8.46
190 180 170 160 150 140 130 120 110 100 90 80 70 60 50 40 30 20 10
f1 (ppm)

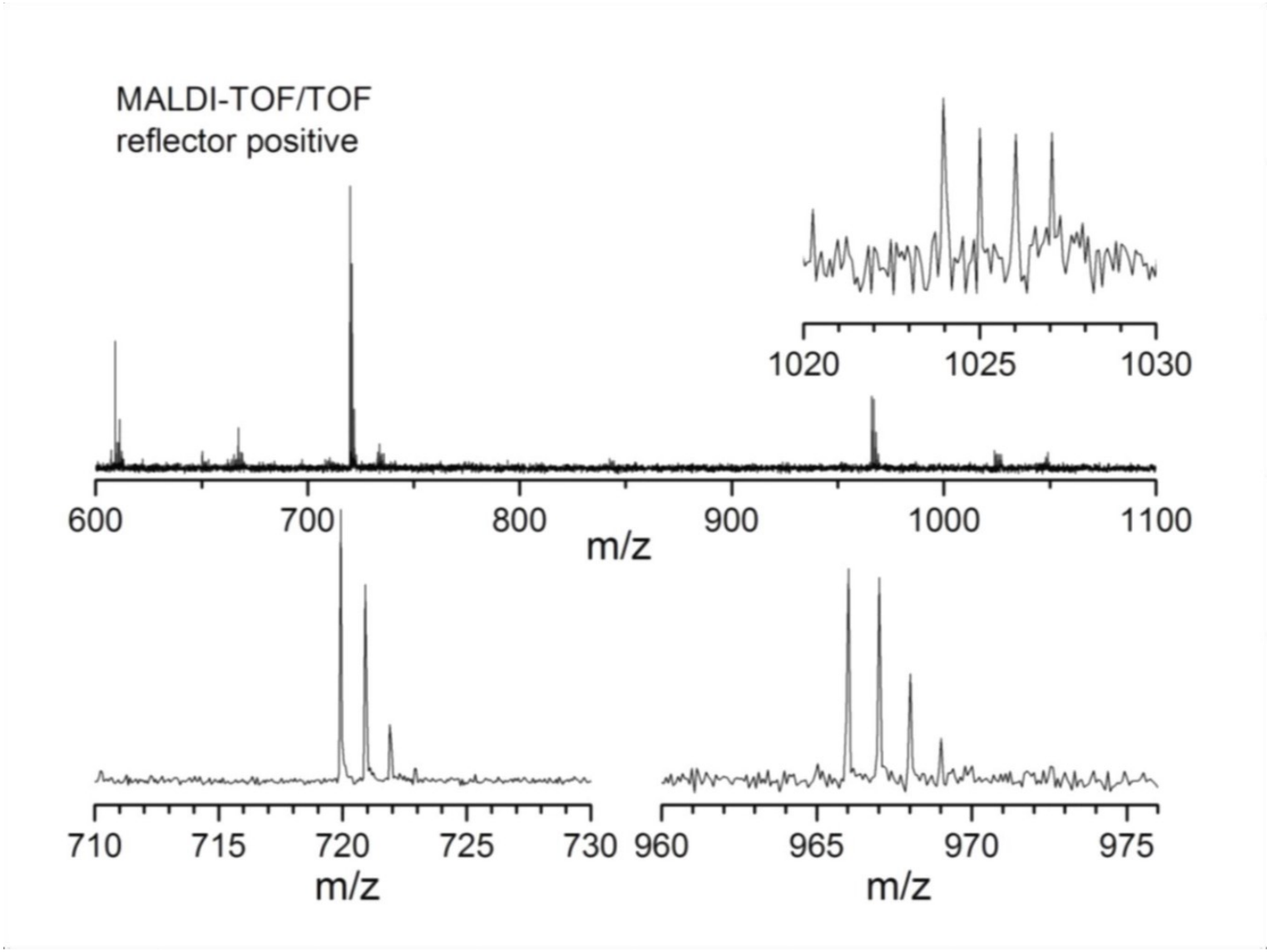
MALDI-TOF/TOF
reflector positive
1020
1025
1030
600
700
800
900
1000
1100
m/z
710
715
720
725
730
m/z
960
965
970
975
m/z

Chapter 2

Nanocrystalline cellulose

In 1838, Anselme Payen identified and characterized the cellulose, the most abundant renewable polymer on earth[1]. Cellulose is made of the repetition of β-D-anhydro glucopyranose units through β-1,4-glycosidic bonds as shown in figure 30.

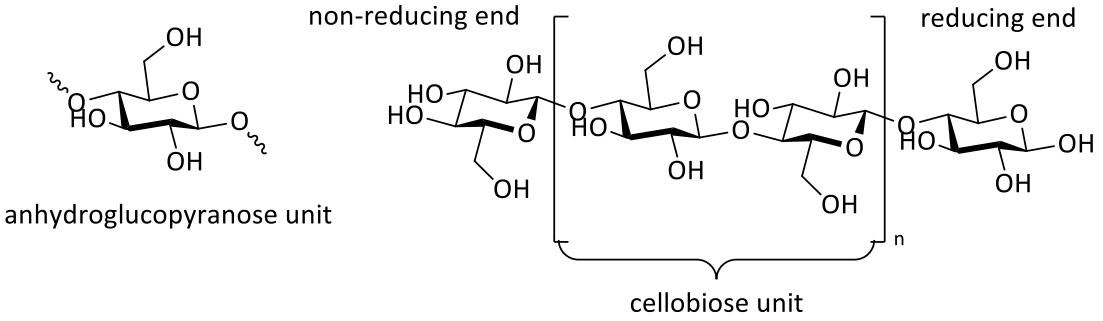

Figure 30. On the left, β-D-anhydro glucopyranose unit. On the right, polymer structure of cellulose.

The β-1,4-glycosidic bond is not only responsible of forming the polymeric chain, but also, due to its rigid structure, blocks the 6-carbon rings in chair conformation. This fact has also an effect on the conformation of the sequence of the glucopyranose units. Indeed, as shown in figure 31, the glucopyranose units are alternatively rotated of 180°, so that the two ends of a chain have different properties. Moreover, this peculiar structure allows the formation of an extended hydrogen bonds network, thanks to the numerous hydroxyl groups, and large crystalline areas. In fact, cellulose polymer chains can organize in hierarchical structures, named fibrils driven by both Van der Waals interactions and hydrogen bonds[2].

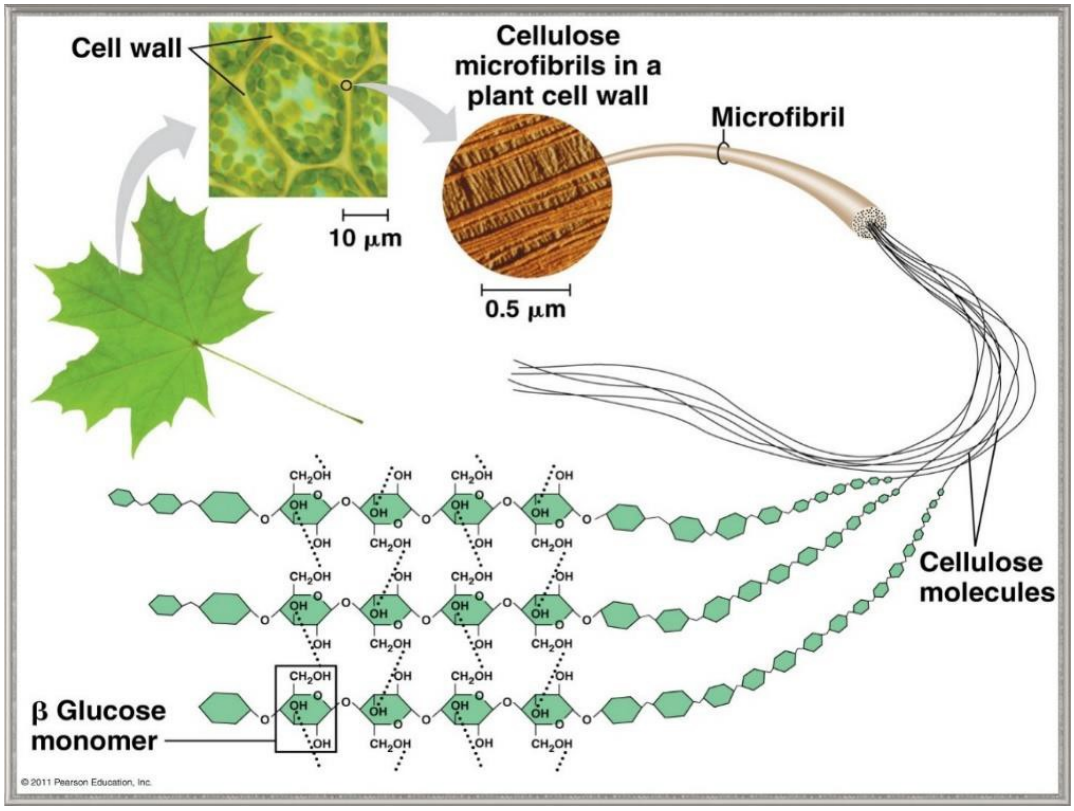

Figure 31. Hierarchical structure of cellulose in nature.

As a cheap, biocompatible and lightweight material, cellulose is widely used for the preparation of paper and in food and pharmaceutical industry. Moreover, several derivatives with different properties can be obtained from this polymer; one of them is nanocrystalline cellulose (NCC), discovered in 1950 by Bengt Ranby who first described the production of NCC from the degradation process of cellulose with sulfuric acid[3]. β-1,4-glycosidic bonds are subjected to hydrolysis in presence of strong acids, degrading the polymeric structure of cellulose. However, crystalline zones are more packed than amorphous zones, so acid diffuse more slowly and degradation can be stopped selectively. The results are needle-shaped nanocrystals (degree of crystallinity up to 88%), called NCC, with thickness from5 to 20 nm and length from 100 nm to 1 µm, as those shown in figure 32.

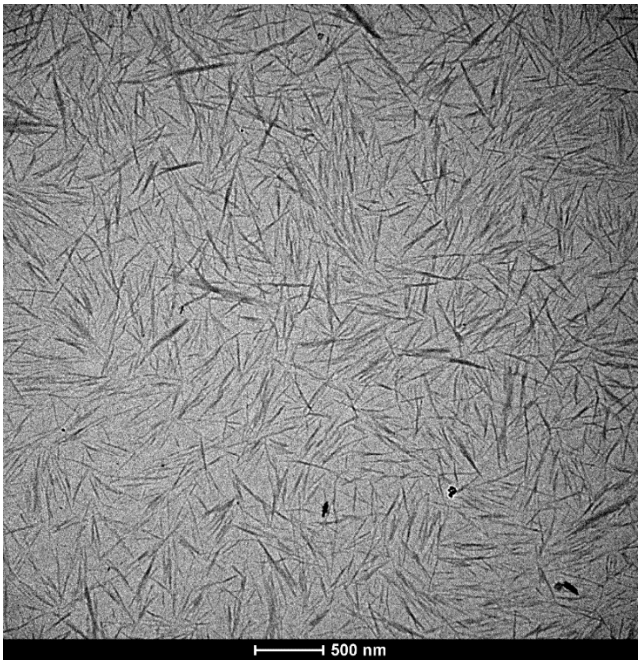

Figure 32. TEM image of nanocrystalline cellulose.

A peculiarity of NCC obtained through hydrolysis with sulfuric acid is the formation of sulfate ester groups (-OSO_3^-), with some of –OH on the surface. The degree of substitution DS can be calculated using the following formula.

$$DS = \frac{\frac{m_{NCC}S\%}{M_S}}{n_{surface(-OH)}}$$

$m_{NCC}S\%$ is the mass percentage of sulfur on the surface of NCC estimated through elemental analysis, M_S is the molar mass of sulfur and $n_{surface(-OH)}$ is the approximated number of surface hydroxyl groups[4,5]. Sulfate defects are particularly important since they impart a net negative charge to the nanocrystals of thus promoting their dispersibility of NCC in aqueous and polar media.

The average size, especially the length of crystals, varies depending on the cellulose source used, for example from cotton, algae or bacteria[6]. This characteristic is particularly important for optical applications, as in aqueous suspensions (from 1% to 10% w/w) NCC can organize in specific helical structure, with path **P** from 20 µm to 80 µm, as shown in figure 33[7].

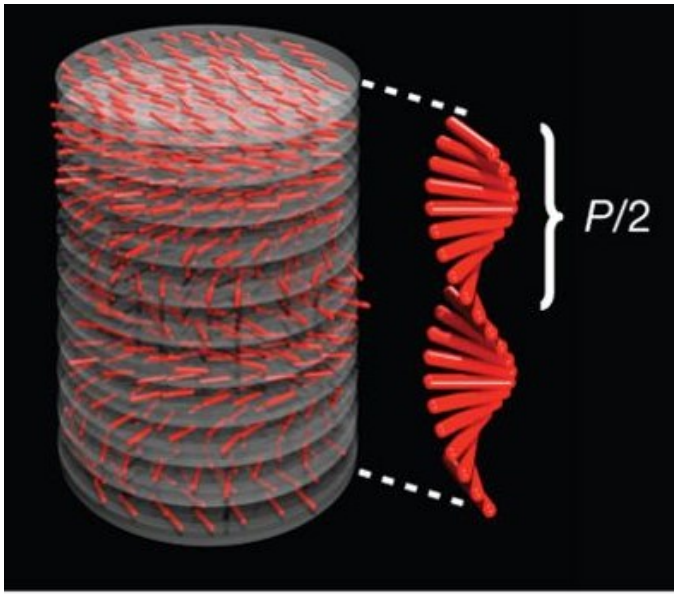

Figure 33. Representation of the helical structure of dispersed NCC.

This peculiarity is responsible for the nematic behaviour of NCC dispersions, typical of liquid crystals and the iridescent aspect of the dried films[8].

From an engineering point of view, NCC is employed for its toughness and flexibility as filler for polymeric materials. Being a cheap and biodegradable resource, NCC is widely used in the industry of packaging and medicine. To the purpose of increasing the dispersibility of cellulose nanocrystals in low polarity non-aqueous matrices, many studies have been carried out in order to chemically modify NCC[9], as it will be described in a better detail in the following paragraph. From the molecular structure of polysaccharides chains, we expect the presence of three hydroxyl groups: a primary –OH in position 6, more exposed and for this reason more reactive, and two secondary –OH in position 2 and 3 (figure 34).

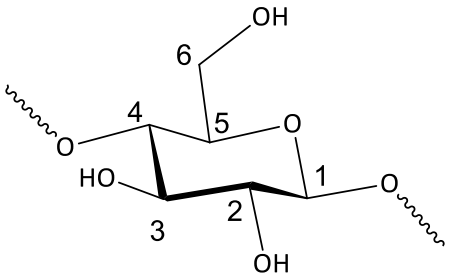

Figure 34. Molecular structure of β-D-anhydro glucopyranose unit with numeric labelling of carbon atoms.

Functionalization of NCC

In general, chemical modification of a nanomaterial is used either to improve its dispersibility in a certain matrix or to add properties to the material itself. In the case of NCC, these modifications occur almost exclusively on the surface of NCC due to the highly packed structure of crystalline cellulose that is hardly permeable. Several approaches are available to functionalize NCC. Most of the procedures, some shown in figure 35, exploit directly the reactivity of hydroxyl groups towards alcohols, carboxylates and amines[10].

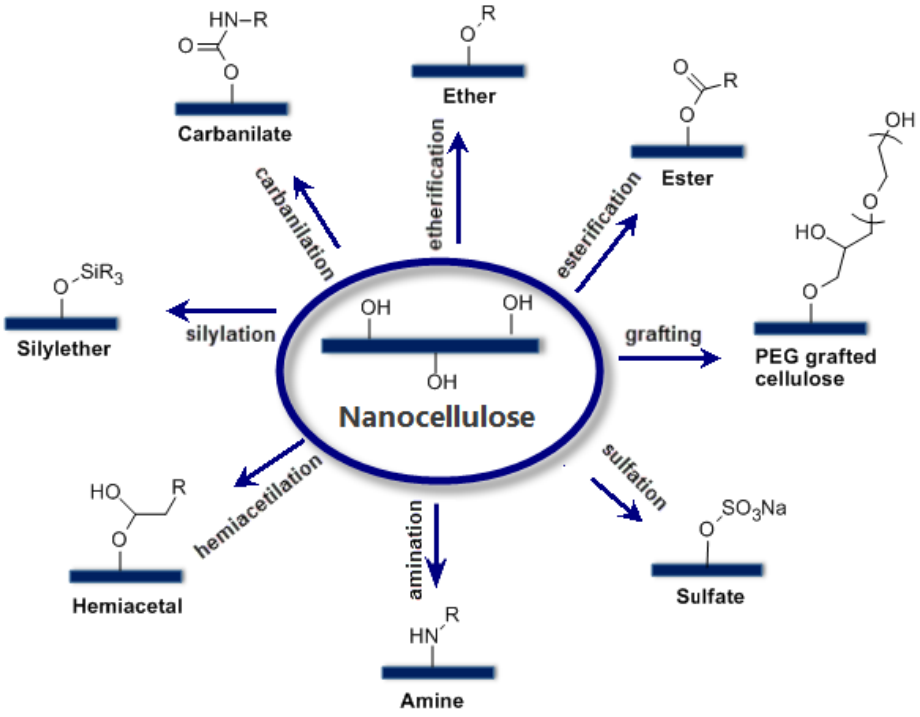

Figure 35. Possible approaches described in literature[10] for the modification of NCC.

Alternatively, –OH groups can be processed to obtain different chemical characteristics. Two interesting examples are silanization[11] and oxidation with TEMPO[12-15] (figure 36), procedures that can add different functional groups for further functionalization.

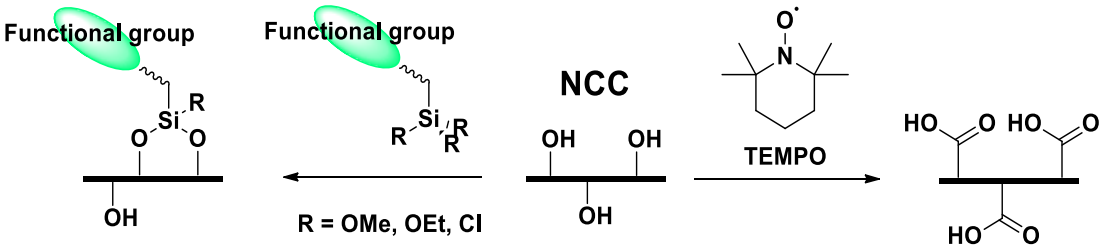

Figure 36. Surface modification of NCC with silane (left arrow) and oxidation with TEMPO (right arrow).

As mentioned before, functionalization allows for adding physico-chemical properties to cellulose nanocrystals. This opens up to a variety of NCC applications in many fields such as medicine, food chemistry, optics and engineering, due to the combination of the mechanical characteristics of cellulose and the specific peculiarities of the selected function. One can combine these properties by both functionalizing NCC with small molecules and by preparing hybrids between NCC and other materials with different characteristics.

Applications of NCC

NCC-dye pH sensors

Great mechanical properties, cheapness, biocompatibility, renewability and the possibility of functionalization make nanocrystalline cellulose a widely employed material in industry and a challenging trend in academic research. In this work, I focused the attention on the chemical reactivity of the surface of crystals and the possible application of the produced nanomaterials.

As mentioned before, the functionalization of NCC is obtained through chemical transformations that involve surface hydroxyl groups. From the industrial point of view, the reactivity of –OH has been widely investigated for dyeing of cotton, especially to increase the solidity of dyes on textiles. These studies have provided a vast selection of reactive molecules that can be immobilized on the surface of cellulose derivatives with strong covalent bonds. In particular, Remazol dyes (shown in figure 37), can be activate to produce a vinyl sulfone intermediate that reacts with hydroxyl groups through Michael addition.

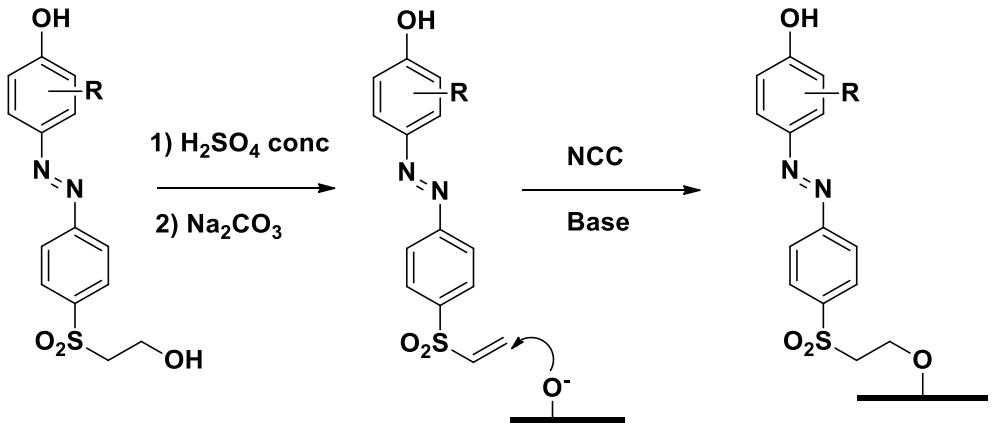

Figure 37. Functionalization of NCC with a generic Remazol dye.

Other than solidly attaching to cellulose, many Remazol dyes are sensitive to pH variations, and can be used as colorimetric indicators [16-20]. This ability is gaining more and more interest in medical and food application, and cellulose-based materials offers a good platform for developing new chemical sensors.

NCC as filler for polyurethane foams

Polyurethanes are widely employed as insulant materials for packaging, refrigeration and, mainly, housing[21]. These compounds are produced by polymerization of diisocyanates and diols as shown in figure 38.

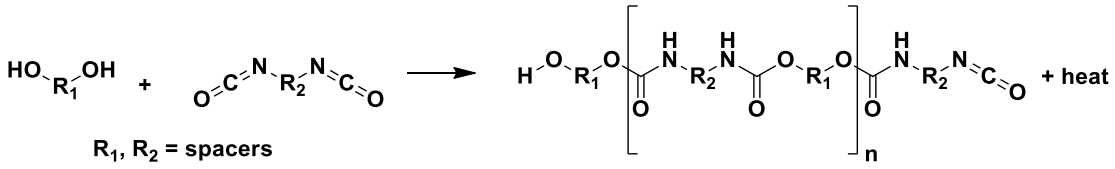

Figure 38. Polymerization reaction of generic diol and diisocyanate.

In presence of a proper amount of water, isocyanate is hydrolyzed generating gaseous carbon dioxide, responsible of the expansion of polyurethane and consequent formation of foam structure. The reaction is shown in figure 39.

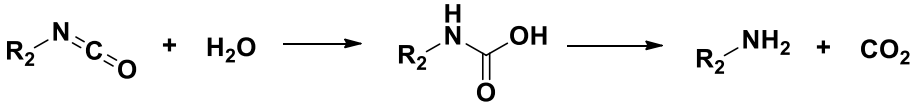

Figure 39. Generation of CO_2 through hydrolysis of isocyanate moiety.

Moreover, amines can react with isocyanates to form a di-substituted urea, shown below (figure 40), compound which is still active in the polymerization due to isocyanate groups.

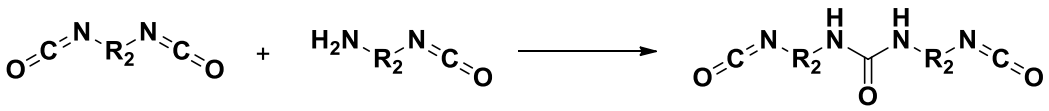

Figure 40. Secondary reaction that occurs in presence of amines.

To ensure mechanical strength to the foam, a mixture of aromatic polyols with low degree of polymerization (DP) is used as starting material, due to the rigid shape of aromatic rings, and diphenylmethane diisocyanate for the polymerization (figure 41).

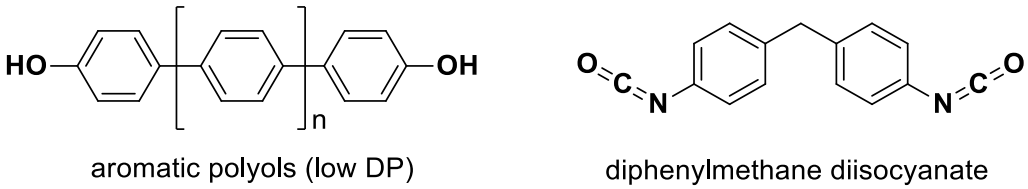

Figure 41. Molecular structure of polyols (left) and diisocyanate (right) used for PU synthesis.

To control the polymerization reaction, catalysts and surfactants are added to the mixture. These molecules affect different phases of the foaming process:

1) Cream time: the mixture starts to assume a creamy consistency and begins to expand;
2) Gel time: start of the hardening process;
3) Tack free time: the polymerization is not completed yet, but the foam is rigid enough to resist to pressure stimuli.

Dimethylcyclohexyl amine and pentamethyl-diethylene triamine, used in this work, are blowing agents that both shorten cream time, by accelerating CO_2 production in presence of water, and have positive effects on gelation process. On the other hand, NiaxSilicones L-6900, a silicone-based surfactant, was used to stabilize the foam structure during cream time.

Polyurethanes are good thermal insulators, but also highly flammable materials. To overcome this issue, additives can be dispersed in PU foams to reduce or to slow down collapse. Other than improving resistance to fire, these compounds can also influence mechanical properties and morphological structure. Out of many reported additives[22-25], NCC has already shown to produce great improvements from the structural point of view, but has been scarcely studied from the thermal characteristics.

Nanocrystalline cellulose, as cellulose-based material, is by nature a thermal insulator. Furthermore, as for many organic polymers including polyurethanes, combustion of requires oxygen to generate gaseous water and carbon dioxide, as shown in figure 42.

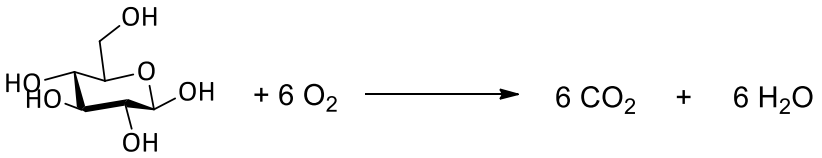

Figure 42. Combustion of cellulose monomer.

Therefore, the thermal decomposition of these materials subtracts oxygen from the environment, an essential ingredient for the propagation of fire, and diffuses gaseous inert species (CO_2 and water), which further reduce the local concentration of O_2. Moreover, at high temperatures, burning organic compounds leave inflammable char residues that deposit on surfaces, protecting from fire propagation. All these properties make the combination of NCC and polyurethanes an interesting composite for engineering applications.

From a chemical point of view, to optimize the characteristics of PU-NCC composites, the main issue to overcome is the homogeneous dispersion of NCC in the polymeric structure of the foam. Polyols, the main ingredient of polyurethanes in terms of volume, are viscous liquids, difficult to be stirred. For this reason, solid additives need high affinity to the PU precursors to obtain a homogeneous mixture. This can be achieved by functionalizing the surface of additives through the addition of specific moieties, following the approaches shown before in page 71.

PU-NCC composites have been already studied by engineers for their improved mechanical properties. The natural properties of cellulose combined with chemical modifications can bring even more advantages in terms of thermal resistance, and consequently open the way for new applications of these systems.

Results and discussion

Functionalization of NCC with Remazol dye GM1

Functionalization of cellulose has been widely investigated in textile industry to avoid leaking of dyes. To this purpose, covalent functionalization is much better than simple adsorption of molecules, due to the strong bonds that can be formed between specific molecules and hydroxyl groups on the surface. I adopted this approach to build a NCC-based pH sensor. I started from the pH sensitive core of the system: the molecular function. I used GM1, a dye from the Remazol serie, a family of dyes that can be covalently bonded to cellulose through Michael addition[16,26-30]. Remazol dyes can be modified to obtain vinyl sulfone derivatives, as described by the steps in figure 43.

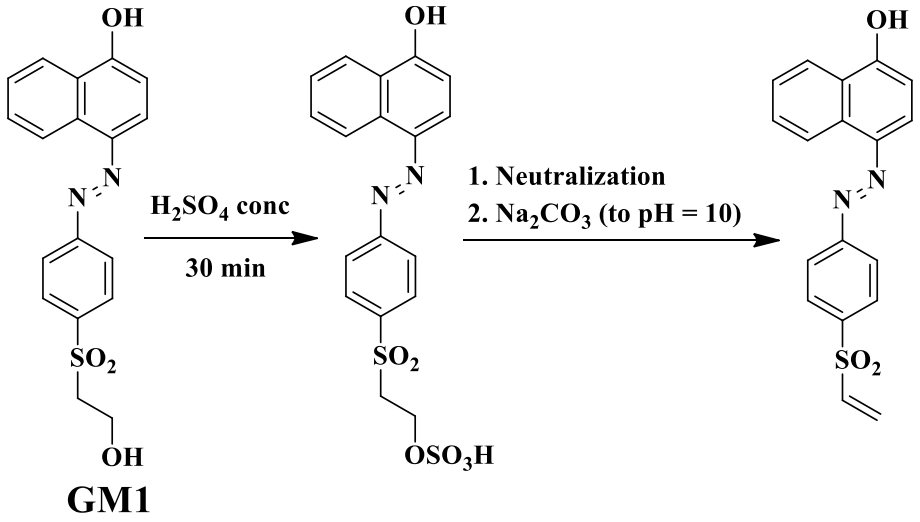

Figure 43. Activation of GM1dye through the synthesis of vinyl sulfone intermediate.

The formation of the vinyl moiety requires the activation of the aliphatic hydroxyl group, to promote the following elimination reaction. To this purpose, concentrated sulfuric acid was employed to obtain the corresponding sulfonic ester by reaction with hydroxyl groups on NCC surface. After neutralization, the pH is increased to 10 in order to promote the elimination reaction and produce the vinyl sulfone intermediate. Finally, nanocellulose is added to the mixture and deprotonated with NaOH. In these conditions, $–O^-$ groups react with –C=C double bonds, which are electrophiles due to the presence of the sulfate group, to obtain NCC-GM1 hybrids, as described in figure 44.

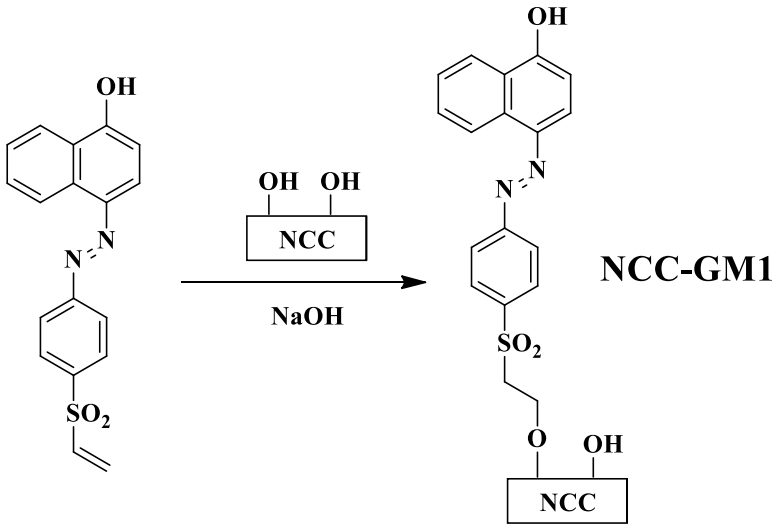

Figure 44. Functionalization of NCC with GM1-vinyl sulfone intermediate.

During the reaction, one can observe colour variations of the dye according to to the different pH conditions used, from intense red in concentrated sulfuric acid, to orange near neutrality, and finally to intense purple at the final steps. The final material itself shows this behaviour after dialysis, as demonstrated in figure 45.

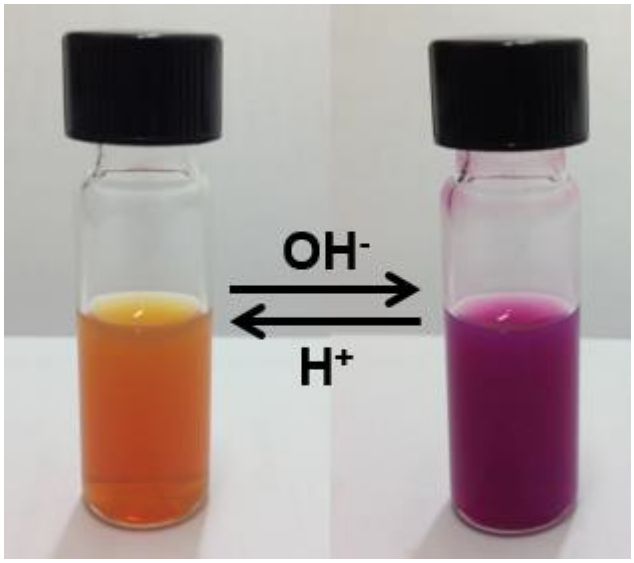

Figure 45. Colour variation at different pH of NCC-Dye hybrids dispersed in water.

NCC-GM1 hybrid is a solid pH sensor. It means that this sensor is easier to be manipulated and processed than its correspondent molecule GM1. Once that GM1 is covalently bonded to the NCC surface, leaking phenomena are prevented and the material can be easily recovered by filtration. However, it is possible to build more sophisticated devices in order to avoid the need of continuous recovery and re-dispersion.

To this purpose, we designed and prepared a device employing NCC-GM1 for urea detection. Urea is an important analyte in clinical tests for bloods and urines, because at high concentration, it is a signal of kidney malfunctioning. In presence of water, urea thermally decomposes generating one equivalent of carbon dioxide and two equivalents of ammonia as shown by the following reaction (figure 46).

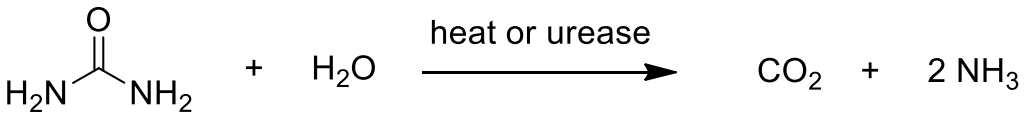

Figure 46. Decomposition of urea.

The same reaction can occur in the presence of the enzyme urease, without the need of increasing temperature. The key point is the generation of ammonia, basic specie that increases the pH of water solutions. For this reason, NCC-GM1 can be suitable as a sensor for urea.

The first prerequisite for a good pH sensor is a pka value similar to the one of the analyte. In other words, urea is the target but it is detected exploiting the urease enzyme so the indirect analyte we are going to measure is ammonia, with a pka of 9.24. The pka of NCC-GM1 hybrid was estimated to be 9.1 ± 0.1[31] with small variations depending on the DS of the starting NCC (these results were obtained through UV-Visible spectroscopy by the research group before I started my work as a Ph. D.), making the nanomaterial a good sensor for urea. Finally, to avoid the necessity of continuously recover the sensor and the enzyme, I decided to immobilize the two in a gel matrix.

To this purpose, I selected tetraethoxysilane (TEOS) as precursor to prepare a sol-gel matrix. To form a gel structure TEOS has to be dissolved in diluted HCl to allow the hydrolysis of Si–OEt bonds; then pH was set to 7 to produce the conditions required for polymerization of silicates. In particular, Si–OH moieties reacts to produce siloxane bonds Si–O–Si, forming a large 3D network[32], as shown in figure 47.

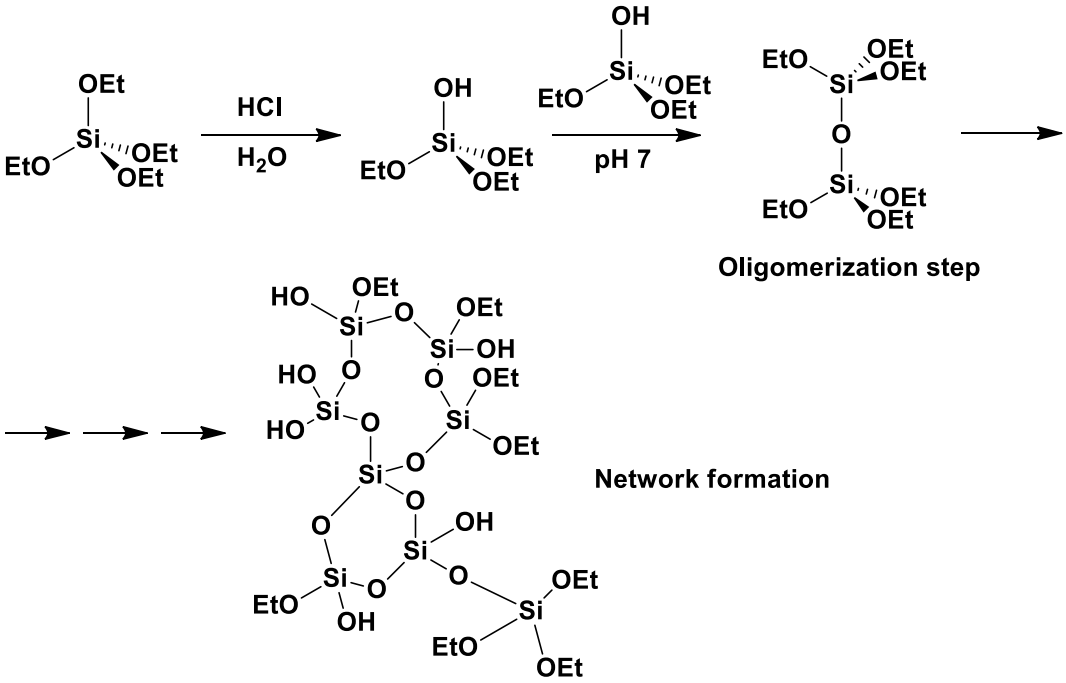

Figure 47. Hydrolysis of TEOS and formation of 3D network characteristic of TEOS gel structures.

The condition used for gelation process allows the incorporation of both NCC-GM1 and urease during the oligomerization step, in order to immobilize the sensor and the enzyme inside the gel matrix. In particular, immediately after neutralization of hydrolyzed TEOS, NCC-GM1 and urease were dispersed in the solution by sonication. The obtained dispersion was distributed homogeneously on one of the four walls of a disposable cuvette, set horizontally until the gel was formed for solvent evaporation. These preparation steps are shown in figure 48.

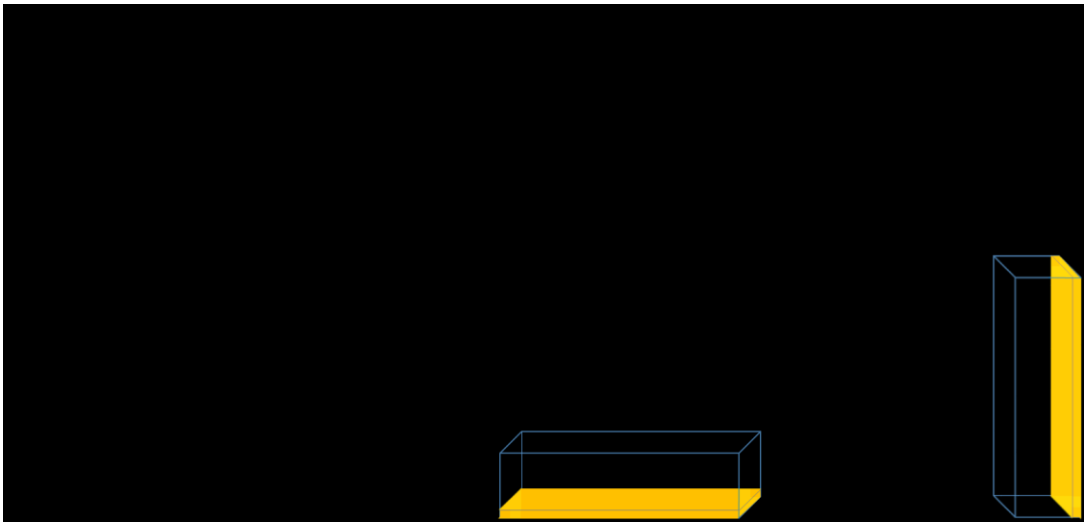

Figure 48. Preparation of devices for urea sensing.

TEOS gel structure allows the diffusion of solvents and small molecules, but can retain larger systems like NCC and enzymes. By filling the cuvette with a urea solution, urea and ammonia can freely diffuse and interact with the system. The reaction can be observed via UV-Visible spectroscopy as shown in figure 49.

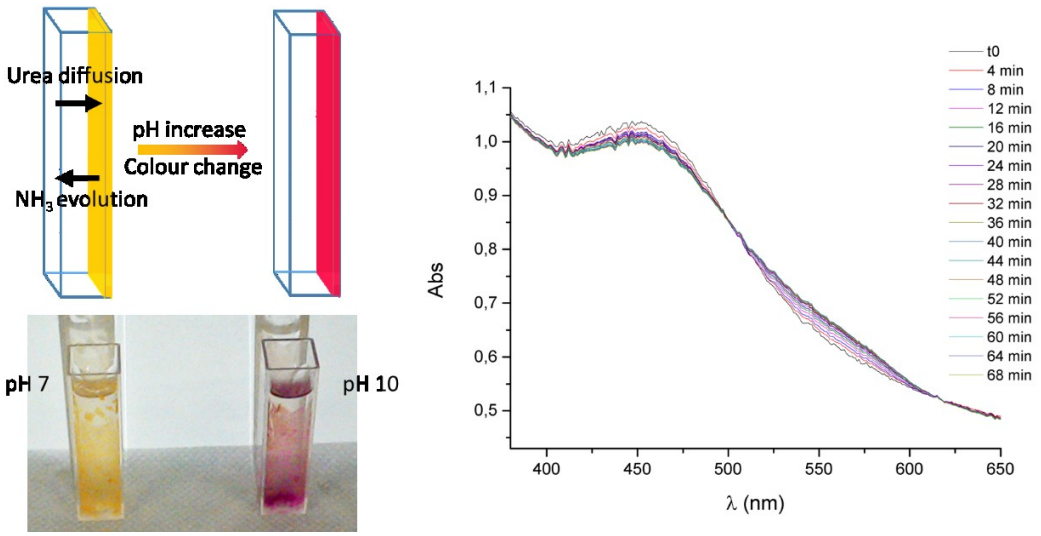

Figure 49. On upper left, scheme of the working mechanism of the device; on bottom right, two cuvettes-sensor at different pH; on the right, UV-Visible monitoring of colour change during time.

Cuvettes were left for 4 hours in TRIZMA buffer to set the starting pH to 7, then emptied and filled with urea solution. Thanks to the cuvette-structure, it was possible to perform analysis directly inside the UV-vis spectrometer without the need of sampling. I monitored the colour change during time obtaining the graph shown in figure 50.

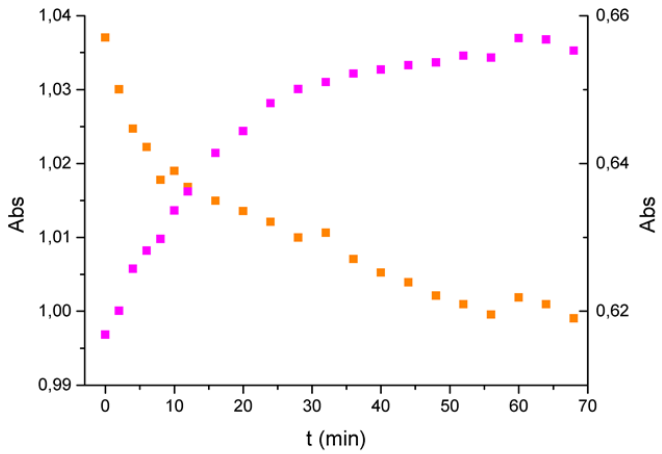

Figure 50. Variation of absorption at fixed wavelength (orange squares for 452 nm and purple squares 563 nm) during time.

Qualitative detection of Urea via UV-Visible spectroscopy or simply colorimetrically was possible using the devices I prepared. In future, I will work to make the colorimetric response faster (by modifying the concentration of NCC-GM1 in gel phase and the thickness of the gel layer) and quantitative.

Preparation and application of NCC-Fe_3O_4 hybrids

Magnetism is a property that can be easily exploited to control magnetic systems. Attraction and repulsion at the molecular scale have been already successfully exploited in chemistry, for example quadrupoles in mass spectroscopy are a good example for what concern the selection and manipulation of molecules. In the nanoscale, magnetic supports can be used to recover catalysts and other precious entities in a fast and efficient way. To this purpose, Lyudmila Bronstein already showed how this approach can be useful and applicable to this aim[33].

As described by Rojas and co-workers[34], Fe_3O_4 nanoparticles can be attached to carboxy-NCC using dopamine as a linker. The resulting hybrid could be collected easily using a common magnet, due to the acquired magnetic properties. I combined this hybrid material with the pH sensor NCC-GM1, described in the previous section, to produce double stimuli-responsive systems.

In this hybrid, magnetism is given by magnetite nanoparticles. It is produced through co-precipitation of Fe^{2+} and Fe^{3+} from water-soluble precursors in the presence of ammonia. The precipitation reaction is carried out under nitrogen, due to the instability of Fe(II) magnetite precursor to air oxygen. Right after precipitation, magnetic nanoparticles are coated with oleic acid, in order to protect them from aggregation. The use of surfactants as protecting agent is reported by Schütch and others as a way to control dimensions and purity of magnetic nanoparticles in general[35]. With this method, I was able to produce nanoparticles with a diameter of about 10 nm, protected by a shell made of oriented oleic acid, as showed in figure 51.

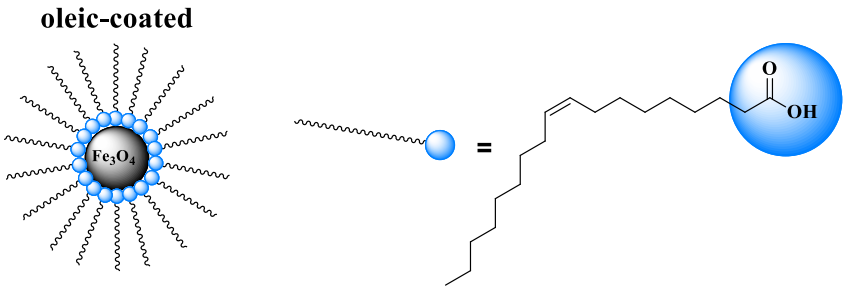

Figure 51. On the left, Fe_3O_4 nanoparticle coated with oleic acid. On the right, chemical structure of oleic acid.

Due to the coating effect of oleic acid, these nanoparticles were highly dispersible in toluene, facilitating purification from ammonia and excess reagents. Dopamine was then added to the dispersion and sonicated in order to exchange with oleic acid, as shown in figure 52.

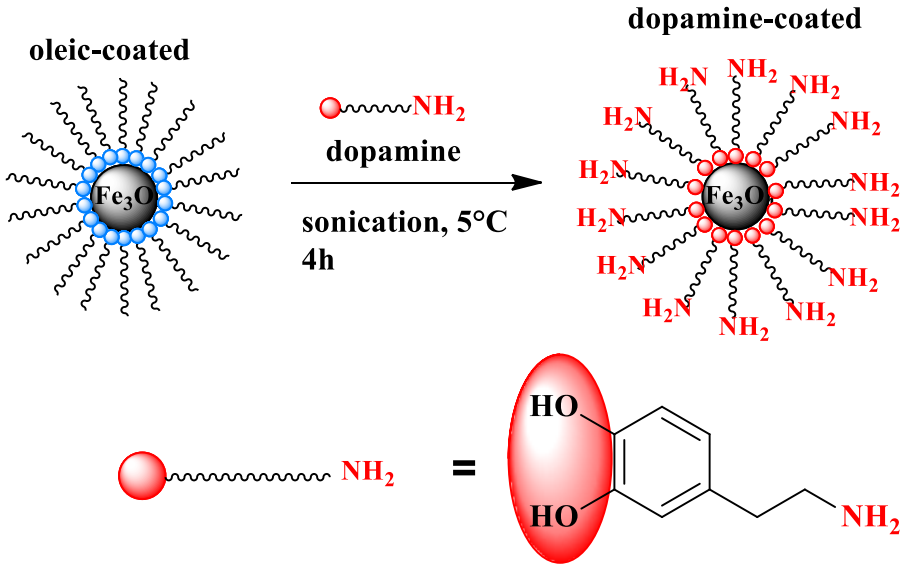

Figure 52. Preparation of dopamine (chemical structure below the reaction) coated Fe_3O_4 nanoparticles through exchange with oleic acid.

The coating with dopamine allowed to obtain amino groups out of the coating shell, allowing simple purification by extraction with water. In figure 53 I reported the different affinity of nanoparticles coated with dopamine and oleic acid to water and toluene phases.

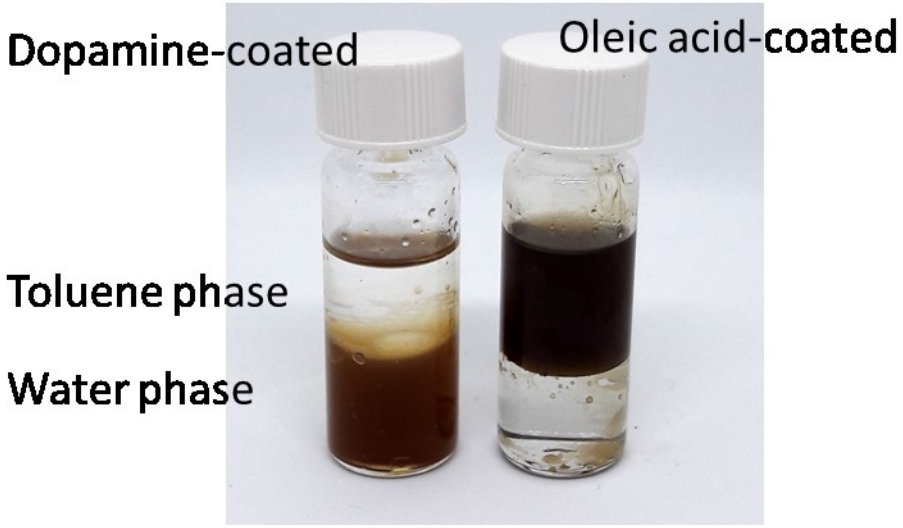

Figure 53. Different affinity of coated nanoparticles to water and toluene.

Amino groups on the outside of coated particles allow also to attach Fe_3O_4 nanoparticles to carboxylated NCC.

Carboxylate groups on the surface of NCC can be obtained by oxidation with TEMPO, a stable radical nitroxide. The reaction (scheme in figure 54) occurs in presence of NaBr, NaOCl and base, and only primary hydroxyl groups are oxidized.

Figure 54. Preparation of NCC-COOH through oxidation with TEMPO.

The extent of oxidation, expressed by the parameter degree of oxidation (DO), can be evaluated by conductometric titration, through the comparison between NCC-COOH and pristine NCC. To perform the analysis, a known amount of material was dispersed in water and a known excess of hydrochloric acid was added in order to increase conductivity of the dispersion. NaOH standard solution was slowly added dropwise under stirring, following the neutralization of acidic species by using an electrical conductivity meter. The curves are shown in figure 55.

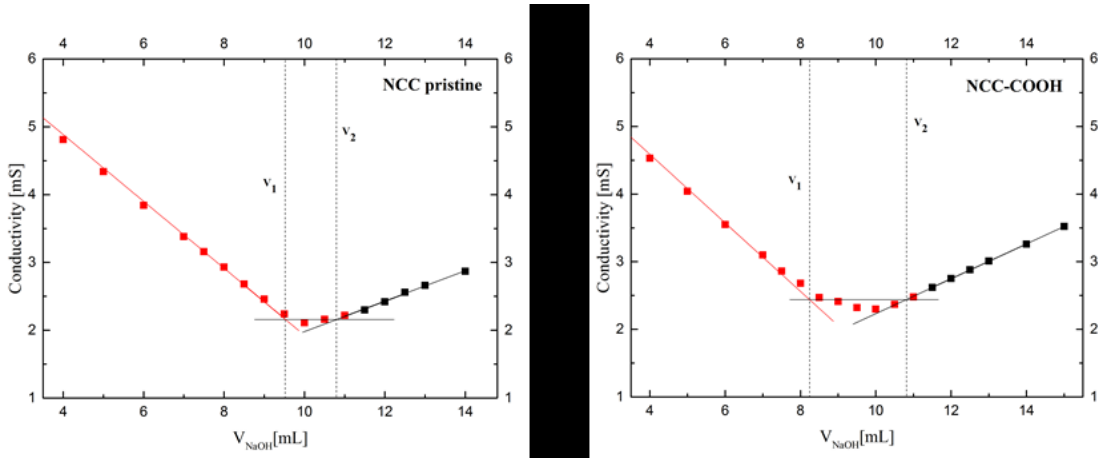

Figure 55. Conductometric titration performed on pristine NCC (left) and NCC-COOH (right).

In the titration curve, one can distinguish 3 main regions:

1) Before the addition of NaOH volume V_1: the excess of HCl increases the conductivity of the system. Gradual neutralization with NaOH reduces constantly the conductivity. The curve slope is high.
2) Between volumes V_1 and V_2: excess of HCl (strong acid) is completely neutralized. NaOH added now is neutralizing weak acidic species on the surface of NCC or NCC-COOH. The curve assumes the shape of a plateau.

3) After the addition of V_2: NaOH is now the specie in excess. The conductivity increases due to the presence of a strong base. The slope of the curve is opposite respect to region 1.

The degree of oxidation (DO) can be calculated exploiting the difference in the plateau of the two curves, using the following formula[13,14]

$$DO = \frac{162 \cdot [NaOH] \cdot (V_2 - V_1)}{w - 36 \cdot [NaOH] \cdot (V_2 - V_1)}$$

where 162 is the molecular weight of anhydroglucose unit, $[NaOH]$ is the concentration of NaOH used in the titration, V_1 and V_2 are the volume of NaOH added between which the plateau is included, w is the mass of dried sample expressed in g and 36 is the molecular weight difference between anhydroglucuronic sodium salt and anhydroglucose. Calculated DOs are shown in table 6.

Sample	DO
NCC pristine	0.06
NCC-COOH	0.12

Table 6. Estimation of DO and the amount of –COONa groups per gram of functionalized NCC.

A higher DO of NCC-COOH is a proof of functionalization of cellulose NCC.

Carboxylic groups can react with dopamine forming strong amidic bonds. The reaction is performed in the presence of N'-ethyl-N-(dimethylaminopropyl) carbodiimide (EDC) and N-hydroxysuccinimide (figure 56)[36,37].

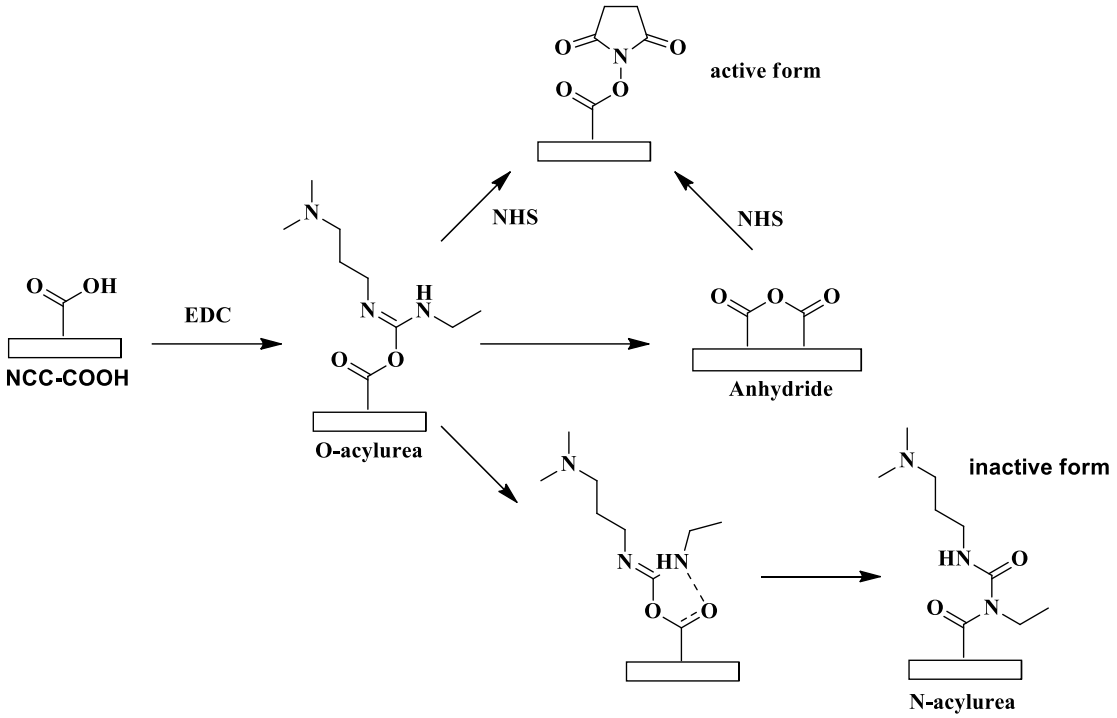

Figure 56. Mechanism for the activation of carboxyl groups on the surface of NCC.

The first step is the formation of O-acylurea, through the reaction between –COOH groups and EDC. The next step is crucial for the activation of hydroxyl groups. O-acylurea is an unstable intermediate that can be subjected to the migration of carboxylates to N-position, with the formation of stable N-acylurea specie. N-acylurea does not react further, decreasing the reactivity of NCC.

Instead, O-acylurea can react directly with NHS giving the active moiety for the reaction with dopamine, or it can react with another –COOH group to form the corresponding anhydride, which can still react with NHS to give the active form. Dopamine coated Fe_3O_4 nanoparticles were added to the activated NCC-COOH to form the amidic bond shown in figure 57.

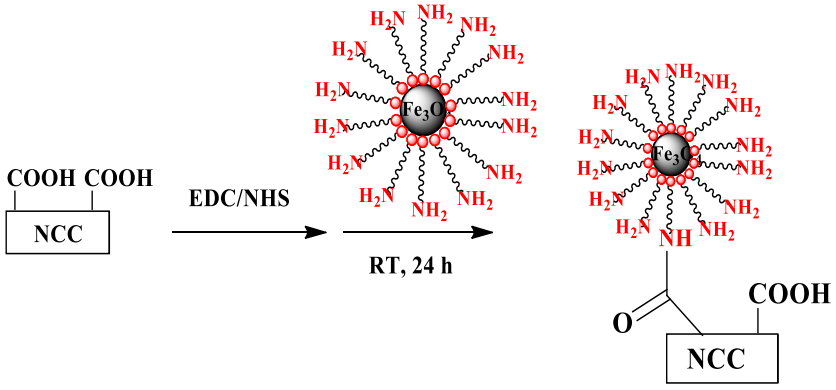

Figure 57. preparation of NCC-Fe_3O_4 hybrids.

To achieve good activation of the surface of NCC-COOH, it is necessary to equilibrate the effects of EDC and NHS to avoid the formation of N-acylurea without slowing down the process.

For the preparation of NCC-Fe_3O_4 hybrids, I used an excess of NCC to facilitate the purification of the product. In fact, after the reaction the separation of magnetic hybrids could be done using a magnet as shown in figure 58, while unreacted NCC-COOH was left in suspension and washed away. If Fe_3O_4 nanoparticles were in excess, it would have been hard to separate them from magnetic NCC hybrids.

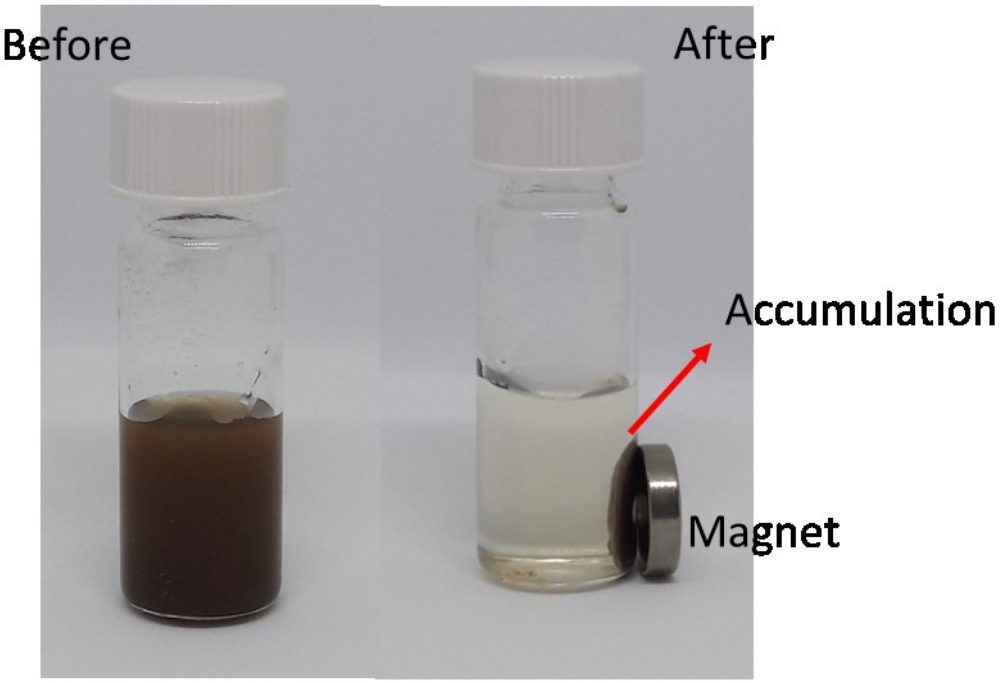

Figure 58. Separation of cellulose hybrids suspended in water with a magnet.

NCC-Fe_3O_4 hybrids were observed by TEM microscopy (figure 59), to confirm the co-presence of cellulose NCC and nanoparticles.

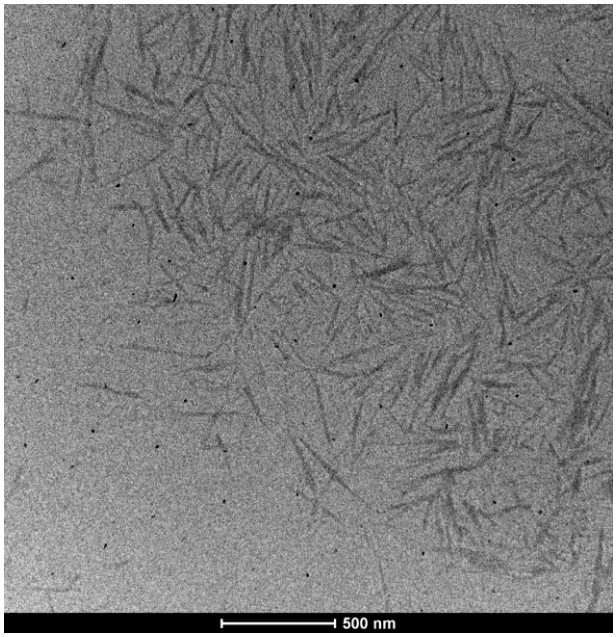

Figure 59. TEM image of NCC-Fe_3O_4 hybrids. NCC can be easily recognised by the needle-shape. Fe_3O_4 nanoparticles are the small black spots (diameter of 10 nm).

These systems were then employed in combination with NCC-GM1 (described previously) to produce double stimuli-responsive alginate beads. Alginate is a linear block copolymer composed by β-D-mannuronic acid (M) and α-L-glucuronic acid chains, as shown in figure 60.

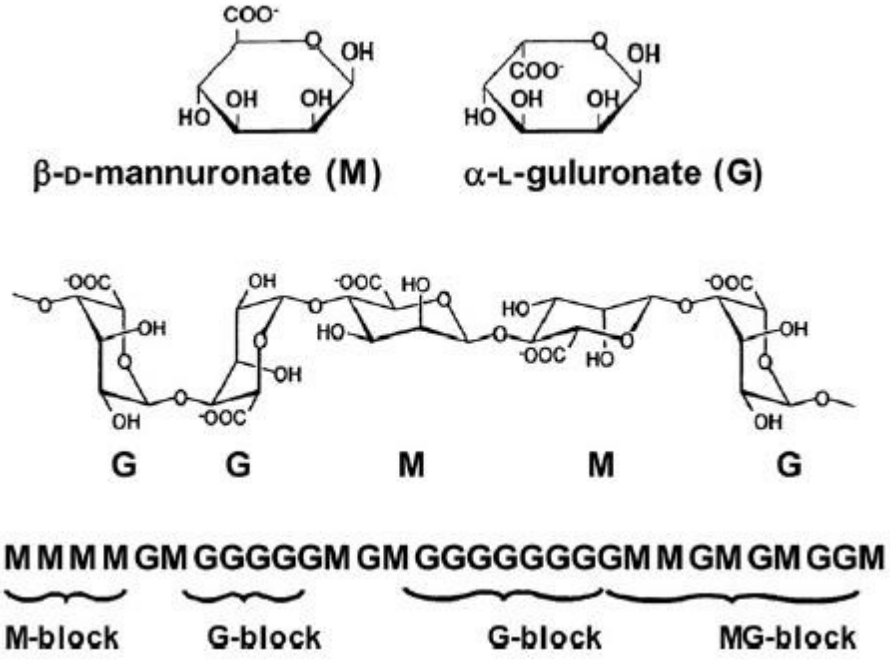

Figure 60. From the top, chemical structure of the monomers; conformation of alternate blocks in the polymer structure; example of chemical composition of polymer chains.

In the presence of bivalent cations, polymer chains are linked together (figure 61), with the consequent immediate formation of gel structures[38].

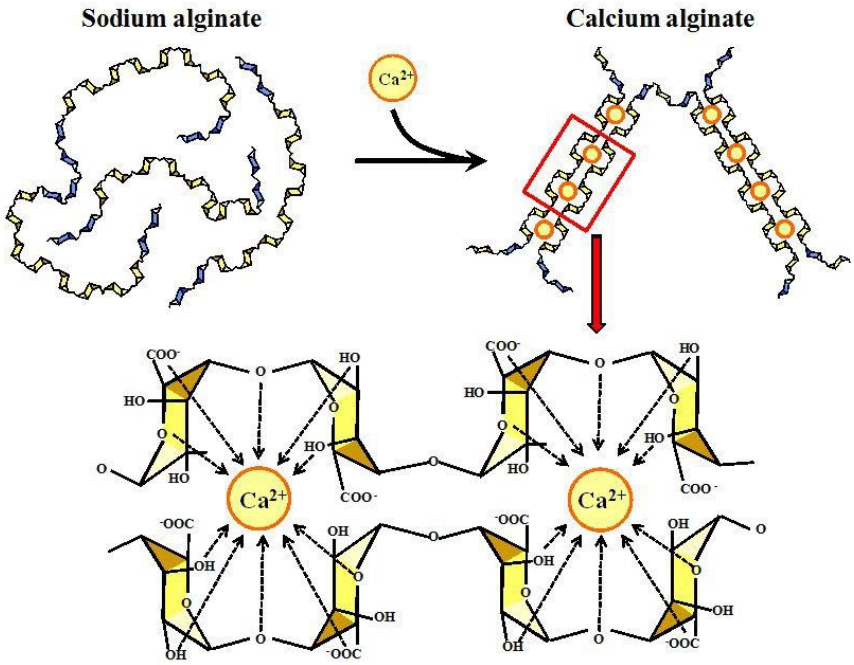

Figure 61. Formation of alginate gels due to the substitution of Na^+ with bivalent Ca^{2+}.

Sodium alginate was dissolved in water, then NCC-GM1 and NCC-Fe_3O_4 were dispersed in this solution. A syringe was filled with the dispersion and a syringe pump was used to drip small droplets inside a concentrated Ca^{2+} solution under stirring. The immediate gelation of calcium alginate blocks droplets into their spherical shape, and, after complete gelation, small alginate beads were obtained. The device used and the obtained beads are shown in figure 62.

Figure 61. On the left, the device used for the preparation of the beads (syringe pump, syringe with alginate, becker with $CaCl_{2(aq)}$). On the right, example of double stimuli-response of the beads to pH variation and magnetic stimulus.

With this procedure, I prepared beads with a diameter of 2.2 mm (as shown in figure 62) that could change colour at different pH conditions and could respond to magnetic stimuli.

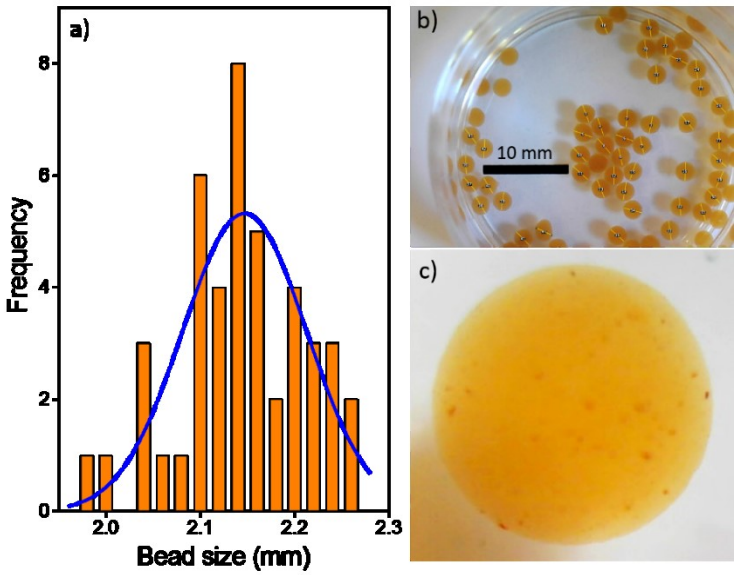

Figure 62. a) Bead diameter distribution; b) picture of the beads c) picture of one bead obtained with optical microscope.

Despite the double-responsive properties of the beads and the biocompatibility of the alginate matrix, we noticed that at high pH the gel structure slowly dissolved. Consequently, the content of the beads leaked into the external solution. Before the application of double responsive beads, I need to find a suitable more pH resistant matrix. Nevertheless, the sensing properties of the materials can be an interesting starting point for future developments.

NCC and NCC derivatives as additives for polyurethane foams

Mechanical properties of NCC have already confirmed the possibility to use this material as an additive for polyurethanes[39]. Thermal and fire behaviour of cellulose nano-derivatives are still argument of interesting research and discussion. My contribution in this topic was to study the characteristics of polyurethanes-NCC foams, starting from the dispersibility of NCC in the polymer matrix and the possible modification that NCC could generate in the foam structure. This project was realized in collaboration with Prof. Alessandra Lorenzetti from the Department of Industrial Engineering of the University of Padova.

To prepare polyurethane foams, ingredients must be weighted in their dry state. This fact is due to the low concentrations required for additives that can be altered easily in presence of solvents and can generate relevant modifications in the polymer structure. For NCC this is the first issue to overcome, because this material is sold as an aqueous suspension. Thus, I started by comparing different methods to obtain dry NCC from a 3% $_{w/w}$ in water suspension:

a) Freeze-drying: by sublimation, I obtained flake-shaped cellulose aggregates that could be redispersed easily through sonication. The water content estimated with TGA analysis was about 4%$_{w/w}$.
b) Evaporation by heating: NCC dispersions were slowly dried in Petri dishes on heating plates set at 40°C. Resulting films were not re-dispersible by sonication and TGA analysis revealed 7% $_{w/w}$ water content.
c) Precipitation with acetone: NCC suspension was centrifuged several times adding fresh acetone portions in order to eliminate water. Then, the obtained NCC was dried under nitrogen flux and under vacuum. The resulting pebble-shaped material was difficult to break using a mortar and was not re-dispersible by sonication since it was highly aggregated. The water content estimated with TGA analysis was about 6%$_{w/w}$.

Therefore, as re-dispersion is a fundamental requisite to produce polyurethane foams, I chose freeze-drying as the most performing method. It should also to be noticed that complete elimination of water was not possible, due to the strong retentive power of NCC. This characteristic has been taken in consideration in all the following steps.

After the production of dried NCC, the dispersion process in polyols was analyzed. Polyols are the main ingredient in term of volume in the preparation of polyurethane foams, but their viscosity makes it difficult to obtain homogeneous dispersions. To this purpose, two different high-powered devices were used, namely a homogenizer and a microtip sonicator. The homogenizer turned out to be the most effective in order to get homogeneous dispersions. To further help the dispersion of NCC, the amount of water required for the expansion of the foam was used to wet NCC before dispersion.

A first attempt to produce polyurethane foam was carried out in the laboratory of Prof. A. Lorenzetti, following a procedure already optimized in her group. A list of the ingredients is reported below.

- Polyols (commercial mixtures)
  - ISOTER 4537
  - ISOTER 842G
  - ISOTER 4530

- Isocyanate (Voranate M600)
- Catalysts
  - DMCHA
  - PMDETA
- Additives
  - NCC
  - H_2O

Wet NCC was dispersed in polyols by homogenization for 10 minutes at 10000 rpm, then catalysts were added and dissolved in the mixture. Finally, isocyanate was added and stirred vigorously for some seconds before the start of polymerization. After a successful first attempt, different samples with different amounts of NCC were prepared in order to optimize the properties of foams. The mechanical and thermal properties of the obtained foams are shown in figure 63.

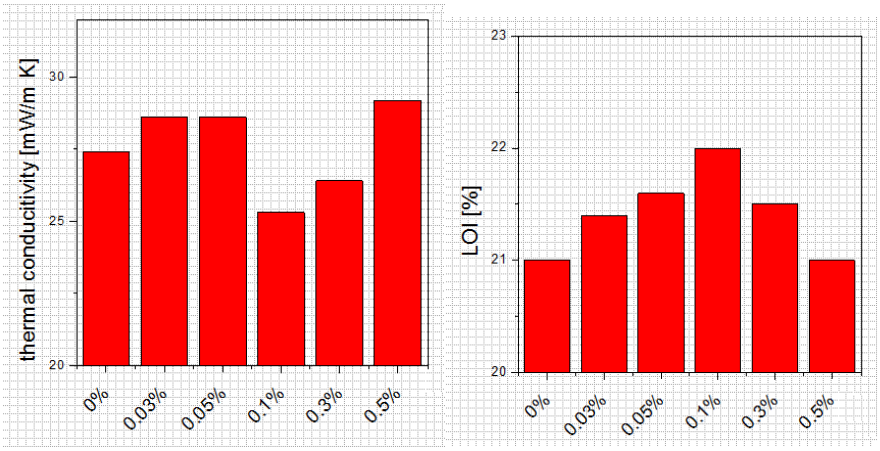

Figure 63. Thermal properties of polyurethane-NCC foams: thermal conductivity and LOI.

The employment of NCC showed interesting modifications in thermal properties. The addition of 0.1%$_{w/w}$ of NCC (respect to the total mass of ingredients) to polyurethane lead to a polymer with decreased thermal conductivity, an important result in terms of insulation, and increased Limiting Oxygen Index, an important aspect in the fire inhibition process. Concentrations above 0.1% did not perform better, probably because of the formation of aggregates in the polymer structure.

To investigate the morphology of PU-NCC foams I prepared fluorescent NCC by functionalizing nanocrystals with fluoresceine isothiocyanate. In order to provide a reactive moiety for isothiocyanate groups, I previously functionalized cellulose with 3-aminopropyl triethoxysilane. The reaction is similar to the one used for the functionalization of silica with fullerenes described at page 52. After purification by centrifugation, the presence of amino groups on the surface of NCC was confirmed through Kaiser test[40].

This particular test is based on the reactivity of ninhydrin towards primary amines. In particular, ninhydrin is at equilibrium with its de-hydrated form, which is reactive towards primary amines to form an imine. In acidic water solutions, the imine is hydrolyzed, giving the correspondent amine. Again, ninhydrin reacts with the newly formed amine to give another imine that is known as Ruhemann's Blue, for the characteristic colour of its solution. The mechanism is shown in figure 64.

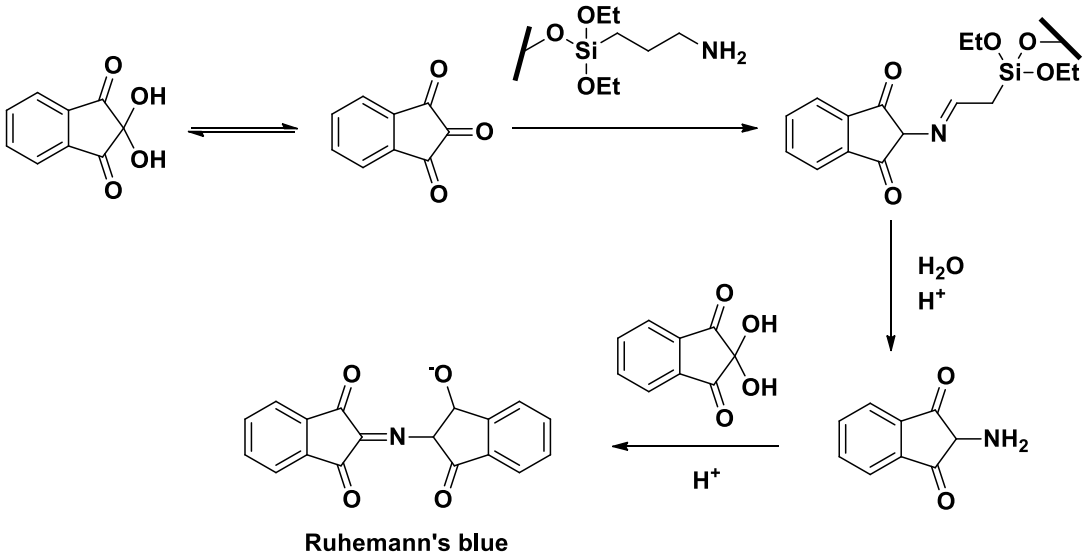

Figure 64. Mechanism of detection of amines with Kaiser test.

The appearance of a blue colour confirms the presence of amino groups on the surface of cellulose nanocrystals.

Amino-functionalized NCC was then functionalized with fluorescein isothiocyanate as shown in figure 65.

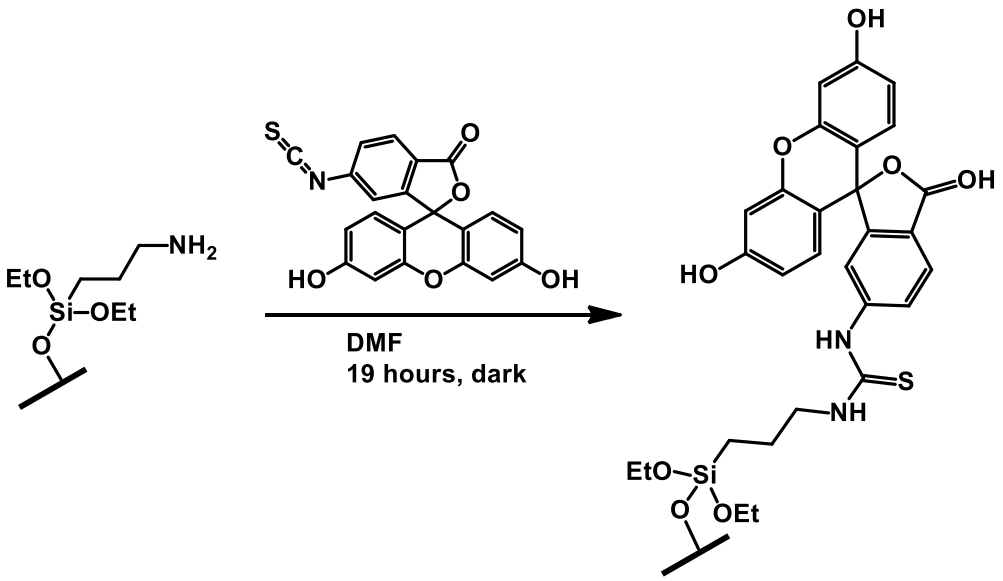

Figure 65. Functionalization of NCC with fluorescein isothiocyanate.

After purification, fluorescence (figure 66) was observed under UV light (254 nm).

Figure 66. Picture of fluorescent NCC dispersed in water.

Fluorescent NCC was freeze-dried and mixed with pristine dried NCC and dispersed in polyols as described before. After foaming process, the resulting polyurethane foam was sliced and observed under a confocal fluorescence microscope. Data collected were elaborated using the software *Icy* to obtain a 3D structure of the foam. Figure 67 shows the reconstruction.

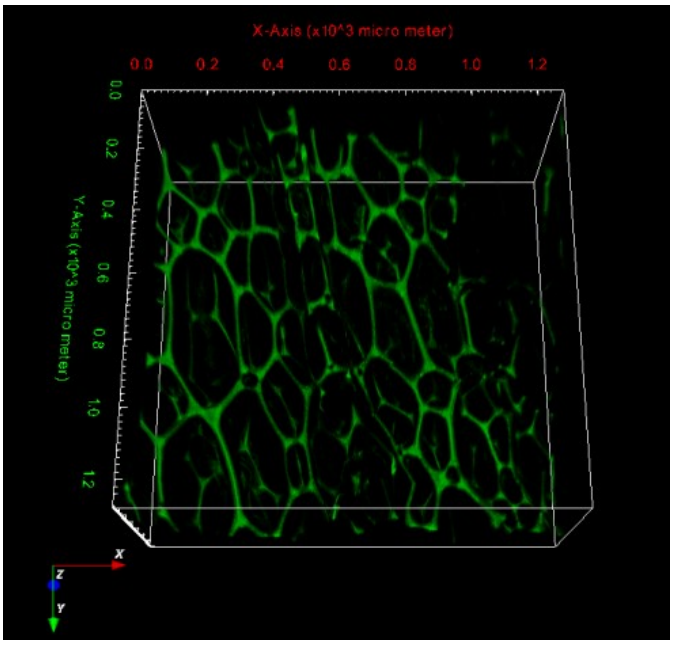

Figure 67. 3D reconstruction of images of fluorescent foams obtained by confocal microscopy.

As one can observe in the picture, green zones representing fluorescent NCC are homogeneously distributed in the polymer 3D network. This fact confirms the participation of NCC in the formation of the foam structure and, consequently, in the improvement of its characteristics.

After verifying the good qualities of NCC as additive for polyurethanes, I designed two functionalization processes that could further improve NCC dispersibility and interaction with the polymer matrix:

a) <u>Functionalization with tannic acid (TA)</u>

Tannic acid and tannins in general are abundant natural polyphenols with low thermal conductivity and low flammability[41]. Moreover, polyphenolic structure (figure 68) is very similar to the structure of aromatic polyols used.

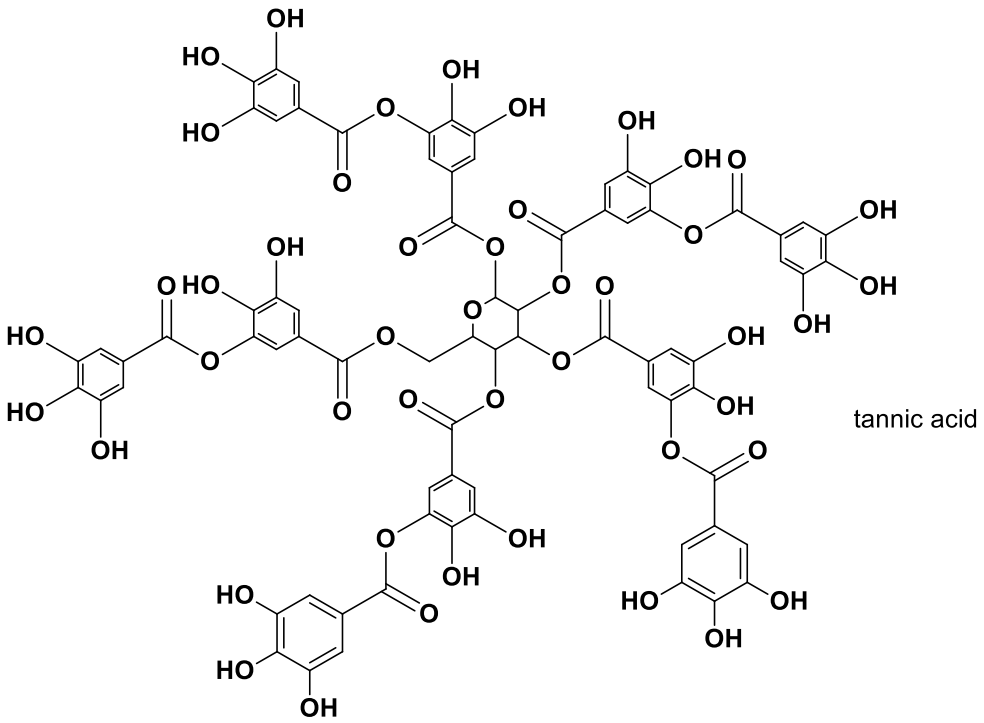

Figure 68. Chemical structure of tannic acid.

For these characteristics, I expect that NCC functionalized with tannic acid should be easier to disperse in the mixture of polyols, thus further improving the characteristics of PU-NCC foams.

The production of NCC-TA hybrids was already reported by the group of Emily Cranston[42]. However, the nature of the bond between NCC and tannic acid remains uncertain. In her work, E. Cranston mentioned a mixed covalent/non-covalent nature, due to the possibility of covalent bonds obtained through transesterification of phenolic branches and non-covalent hydrogen bonds.

Anyway, functionalization with TA provides phenolic or quinonic moieties on the surface of NCC, as shown in figure 69.

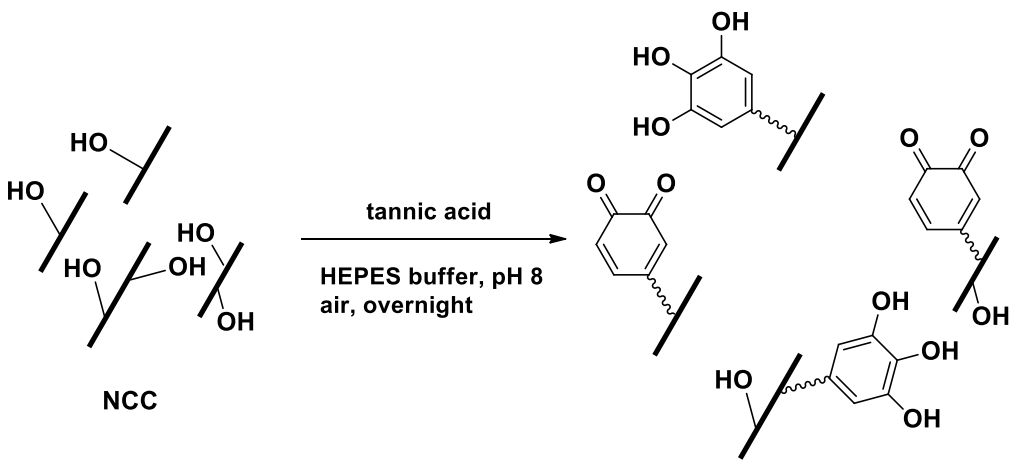

Figure 69. functionalization of NCC with tannic acid.

Phenols groups present in tannic acid can be oxidized by air oxygen, generating quinones. Dispersions of NCC-TA assume a dark colour during the reaction, colour that becomes even darker in presence of air. The dried material instead has light brown colouring.

b) <u>Functionalization with 3-aminopropyl triethoxysilane (APTES)</u>

The functionalization of NCC with APTES was already described at page 91. The amino groups present on the surface of nanocrystals are reactive towards many chemical species. Out of them, isocyanates are the interesting moiety in this work, because they are one of the ingredients of polyurethane foams. As explained in the introduction, amines can react with isocyanates forming di-substituted ureas. NCC bearing amino groups on the surface can become, in this way, a solid support for the polymerization of polyurethane chains, shown in figure 70.

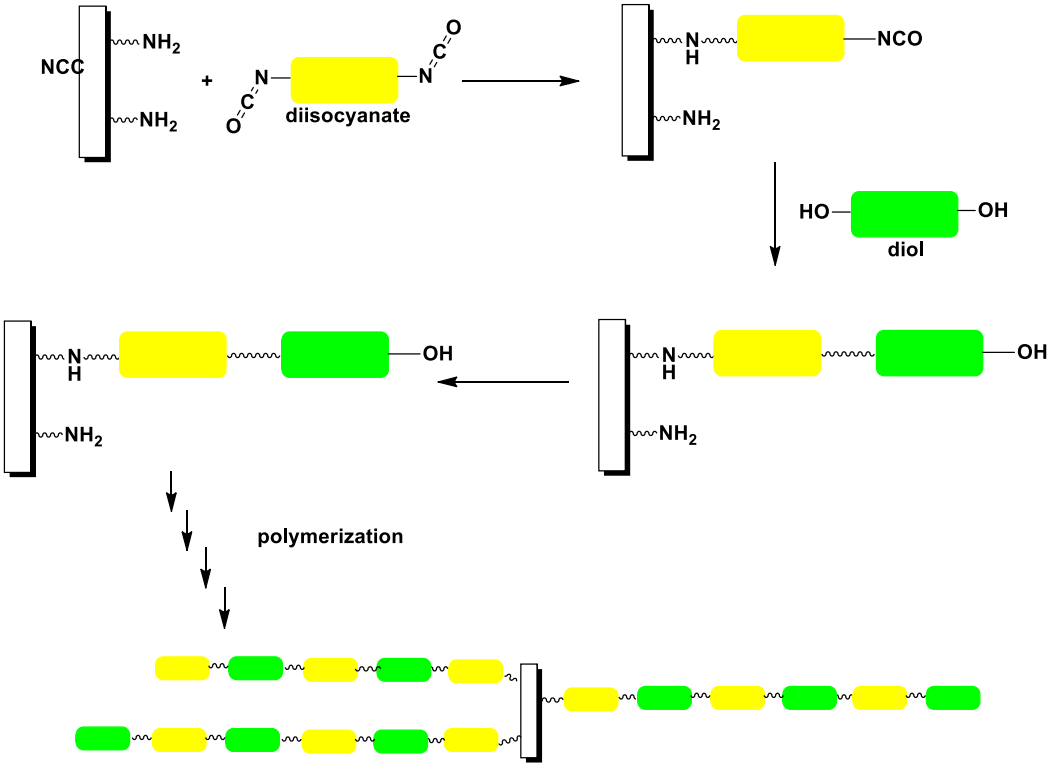

Figure 70. NCC-driven polymerization of polyurethane chains.

Following this route, I wanted to study the behaviour of foams when NCC is not only dispersed in the polymer network, but becomes itself the nucleus of polymerization of polyurethane chains.

As for pristine NCC, I dispersed 0.1%$_{w/w}$ of modified cellulose to obtain different foams with NCC-TA and NCC-APTES. The thermal properties of these two foams, reported in figure 71, were obtained following the same procedures seen before.

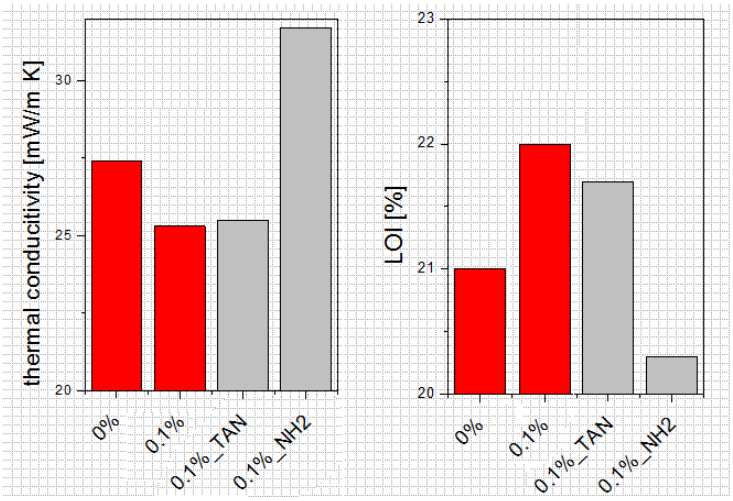

Figure 71. Thermal conductivity and Limiting Oxygen Index of obtained polyurethane foams; from left to right, without NCC, with pristine NCC; with NCC-TA; with NCC-APTES.

Polyurethane foams with NCC modified with tannic acid showed results comparable to the foams with pristine NCC.

The addition of NCC-APTES instead lead to a foam with considerably different properties. Unfortunately, from the engineering point of view, this modification of NCC is not suitable for the application studied; however, this difference aroused my curiosity regarding any changing between this polymeric material and the previous ones. In a future perspective, I think it could be interesting to investigate the structure of foams prepared with NCC-APTES moieties.

Conclusions

I studied the modification of NCC properties through chemical functionalization, in order to apply this material in different field of interest. I prepared a pH sensor by anchoring a pH sensitive dye to the surface of cellulose nanocrystals, exploiting directly the reactivity of hydroxyl groups, which are abundant on the surface of cellulose nanocrystals. The pH sensor was then incorporated in a TEOS gel matrix with the enzyme urease to build a cuvette-device able to detect urea. This prototype, based on the enzymatic decomposition of urea and on the pH sensitive abilities of NCC-dye derivative, allowed to follow urea decomposition via UV-Visible spectroscopy and colorimetrically.

I explored also other chemical modifications of NCC and the preparation of hybrids that conjugates the properties of NCC with the magnetic nature of magnetite nanoparticles. First, I learned how to prepare small magnetic particles bearing amino moieties for further functionalization. I modified the surface reactivity of NCC by oxidation of –OH groups to obtain carboxylate groups, reactive towards amines. In this way, I was able to combine NCC with Fe_3O_4 nanoparticles and obtain magnetic-responsive hybrids. This material was used in combination with the previous NCC-dye derivative to produce alginate gel beads able to answer to both magnetic and pH stimuli.

Finally, I contributed to the investigation of the use of NCC as an additive for polyurethane foams. I studied the dispersion of cellulose nanocrystals in polyols and the thermal characteristics of PU-NCC foams. After optimization of process steps, NCC has been proven to be a performant additive producing a decrease of thermal conductivity and an increase of LOI factor, important parameters in the evaluation of the quality of fire-retardant foams to be used in thermal insulation. I employed NCC functionalized with fluorescein to verify the homogeneity of dispersion of NCC in the polymer matrix. Moreover, I designed two possible functionalization routes, employing tannic acid and APTES, in order to modify the properties of foams and study the contribution of NCC in the modification of the polymeric polyurethane structure.

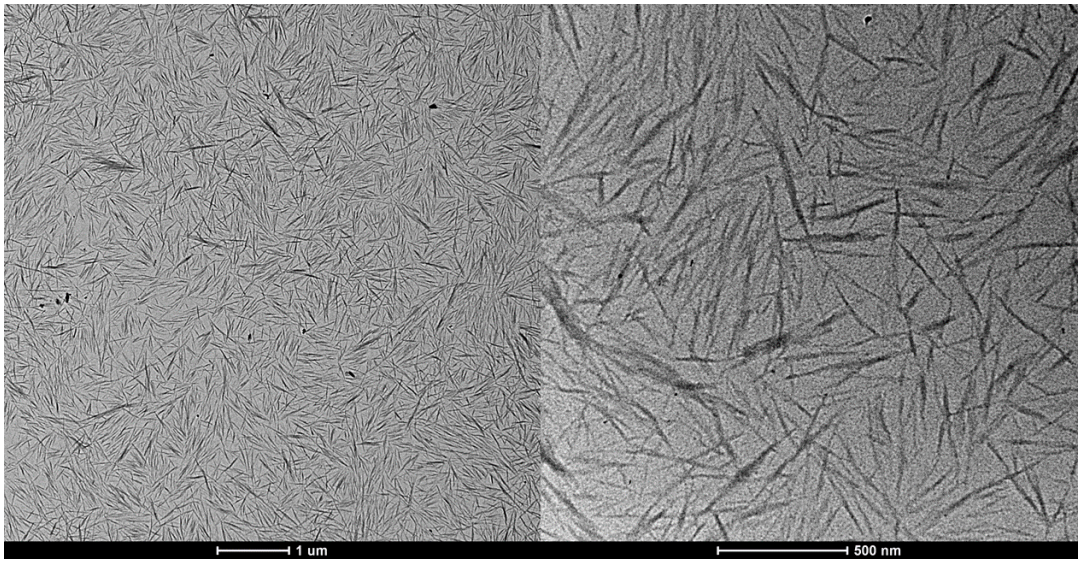

TEM images of NCC.

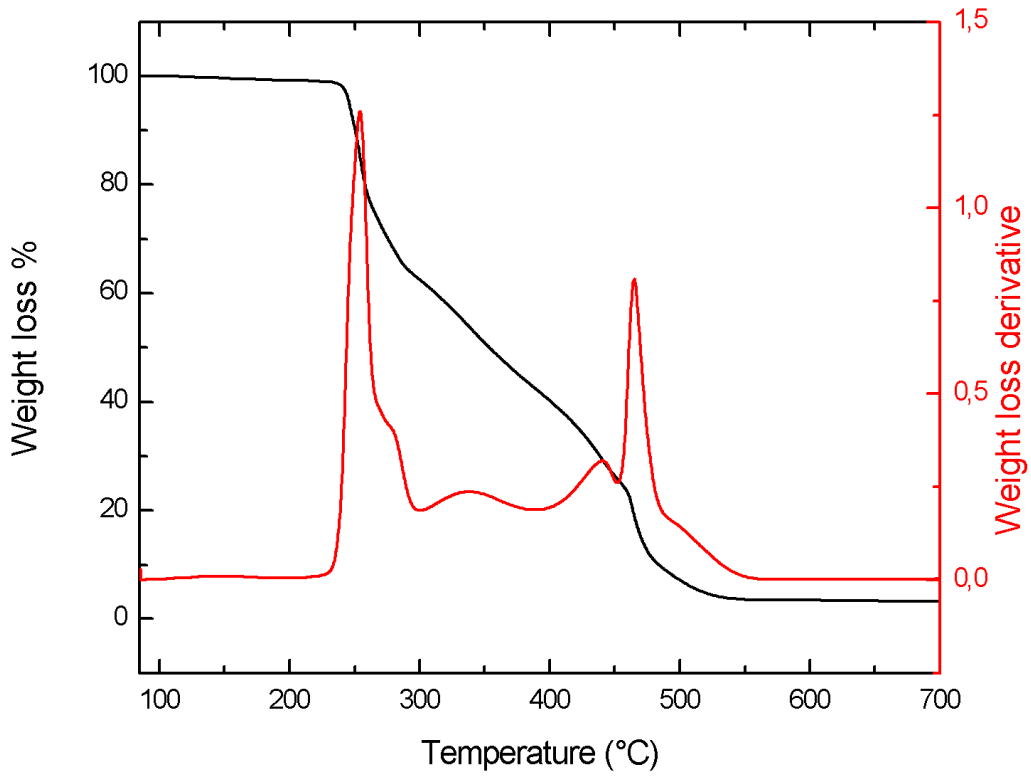

TGA analysis of NCC.

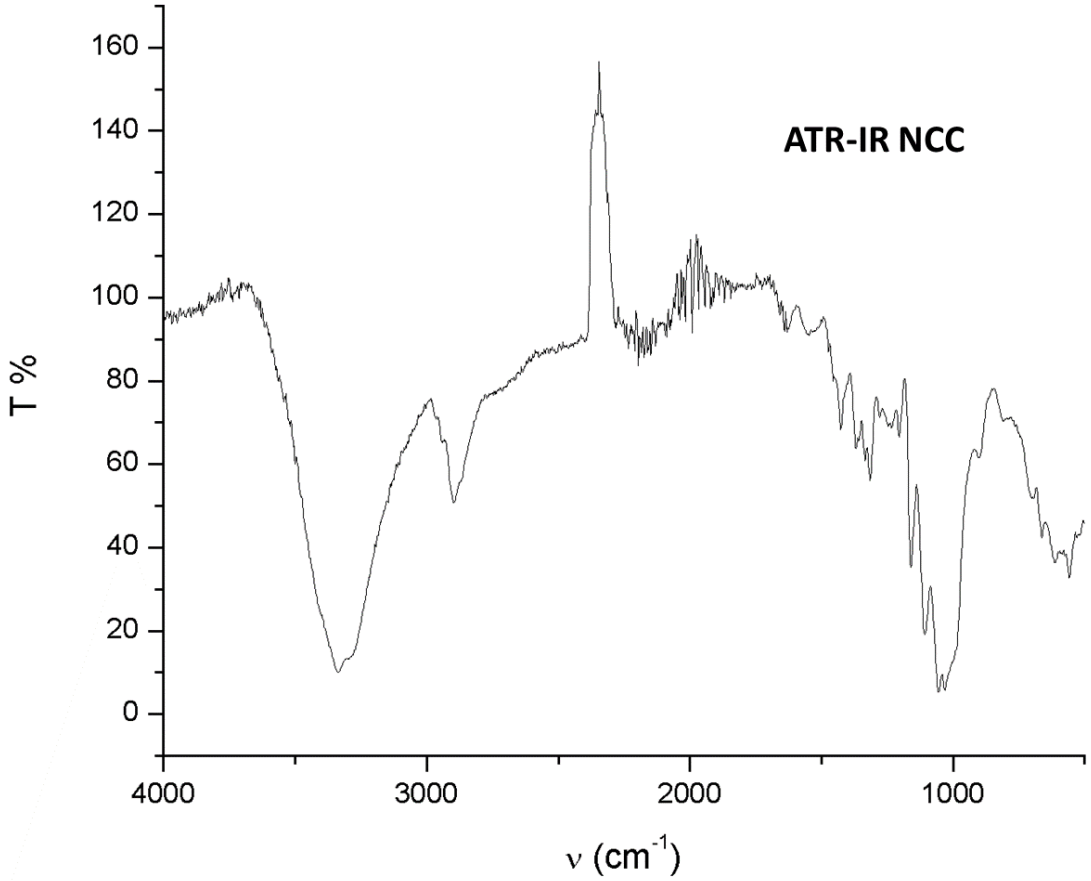

ATR-IR spectrum of NCC.

Elemental analysis (mass content)

C%	H%	N%	S%
39.55	6.08	/	1.15

pH responsive NCC-Dye hybrid as urea sensor

Preparation of NCC-Dye hybrid

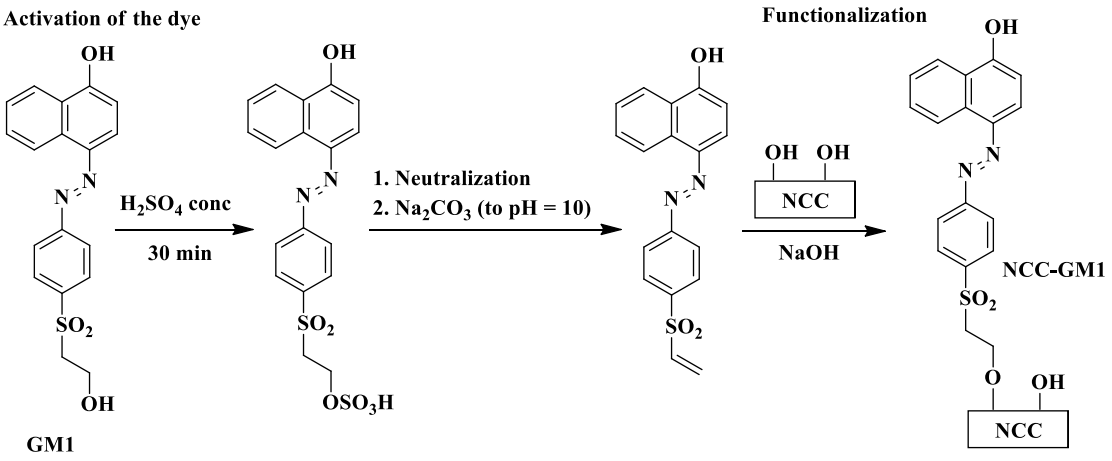

GM1 (20.1 mg, 0.056 mmol) was dissolved in concentrated sulfuric acid (0.69 g). After 30 minutes, the solution was diluted with 5 ml of milliQ water and neutralized with $NaOH_{(aq)}$ (32%). $Na_2CO_{3(aq)}$ (29 mmol) was added to reach a pH value of 10. Then a water dispersion of NCC (30.46 g, 3.39 % w/w) was added to the solution under vigorous stirring. After the homogenization of the dispersion, $NaOH_{(aq)}$ (32%) was added to increase the pH to 12 and the reaction was carried on for 4 hours. The product was washed centrifuged (12000 rpm for 1 hour) and resuspended in milliQ water several times before being dyalized against water until the colour changed for magenta to orange. The product was deposited by centrifugation and resuspended in the minimum amount of water.

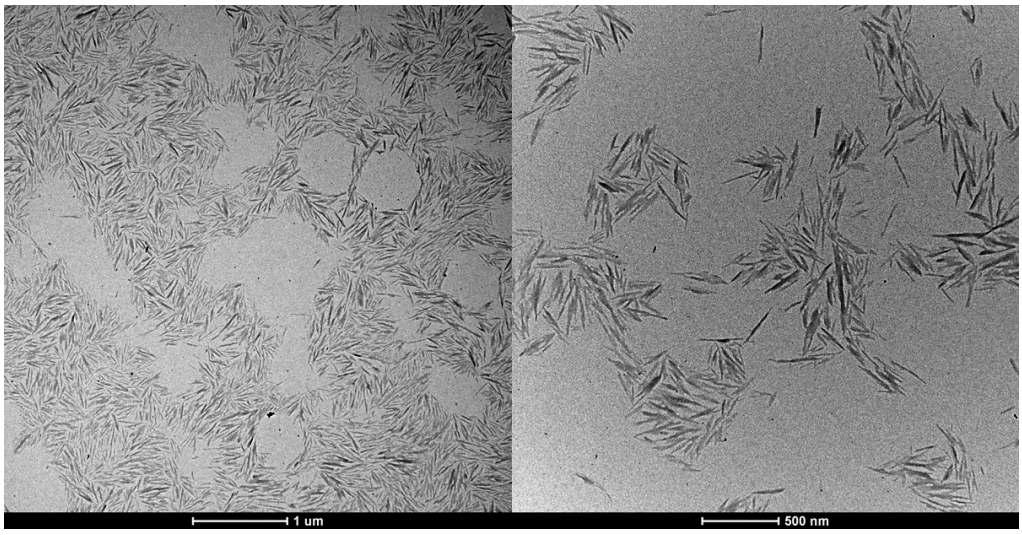

TEM images of NCC-GM1.

Immobilization in TEOS matrix

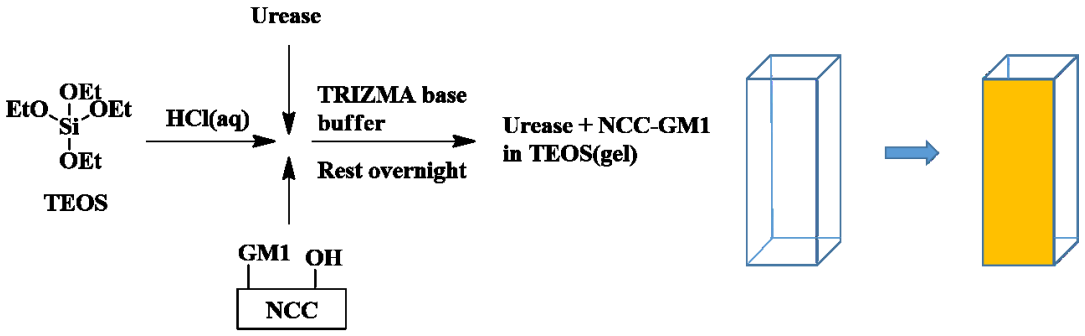

TEOS (7.65 ml) was mixed with water (2.3 ml) and HCl (167 µl). After complete dissolution, 5 ml of TEOS solution were mixed with 100 µl of urease solution and 500 µl of NCC-Dye dispersion (see page 101). The mixture was spread on one of the four walls of a disposable UV-Visible cuvette as shown in the scheme, then left at open air overnight to evaporate the solvent. 2 cuvettes could be prepared with this TEOS amount.

UV-Visible analysis of urea solutions

Trizma base buffer (pH = 7) was poured into the cuvette for 2 hours to set the starting pH. A urea solution (10 mM in water) was then poured into the cuvette to perform UV-Visible analysis.

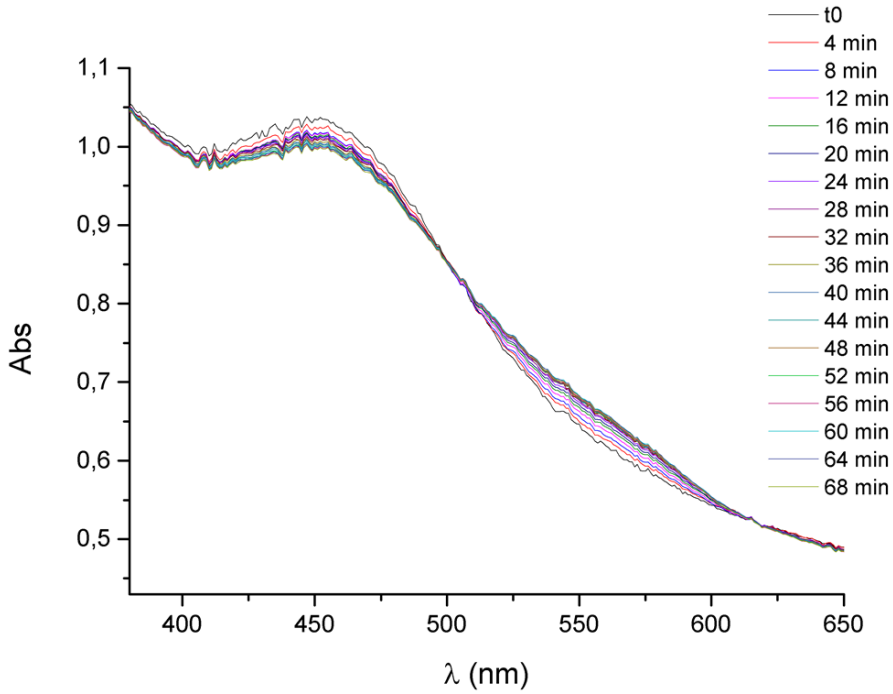

UV- Visible monitoration of sensor-cuvette loaded with a urea solution.

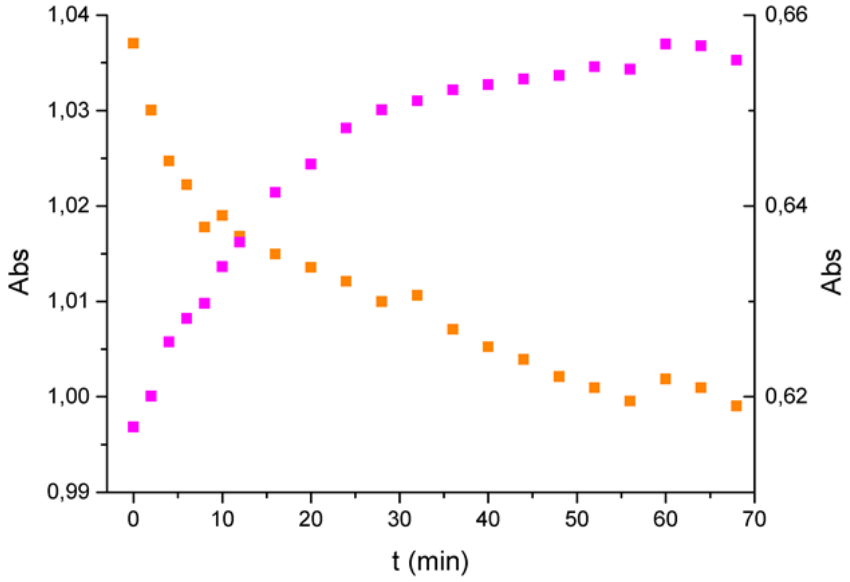

Variation of absorption at fixed wavelength (orange squares for 452 nm and purple squares 563 nm) during time.

Double responsive alginate beads

Synthesis of Fe_3O_4 magnetic nanoparticles

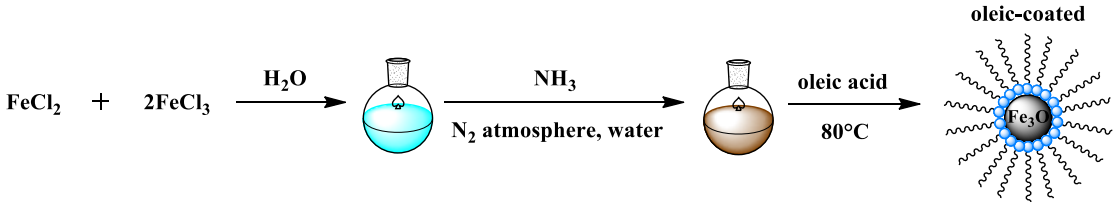

$FeCl_2 \cdot 4H_2O$ (1.5 g, 1 eq) and $FeCl_3 \cdot 6H_2O$ (4.1 g, 2 eq) were dissolved in 100 ml of water under N_2 atmosphere. After 20 minutes a clear solution was obtained and 25 ml of a 25 % $NH_{3(aq)}$ solution was added quickly under vigorous stirring, changing the colour from orange to black. Then the solution was heated up to 80°C and 1 ml of oleic acid was added slowly over a period of 1 h. The suspension was left stirring overnight under N_2 atmosphere at room temperature. Toluene (about 100 ml) was added in order to extract the Fe_3O_4 nanoparticles from water using a separating funnel. For quicker separation some ml of NaCl brine were added. The product in toluene was stored in the fridge.

Dopamine coating of Fe_3O_4 nanoparticles

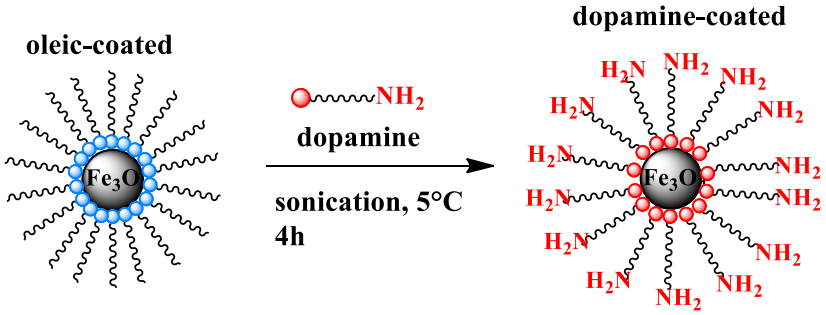

50 ml of the Fe_3O_4-oleic coated Nps dispersion (1.58 % w/w) were divided in two centrifuge tubes and methanol was added in order to eliminate the excess of oleic acid. The suspension was centrifuged (9000 rpm for 30 min) and re-dispersed in fresh methanol three times, then the Nps were separated from methanol using a magnet. The Nps were transferred into a round bottom flask using 125 ml of water. Afterwards, 75 ml of DMF and dopamine (0.5 g) were added under stirring and the suspension was sonicated in an ice bath for 4 h. DMF and unreacted Fe_3O_4-oleic

coated Nps were eliminated by centrifuging several times substituting the supernatant with fresh MeOH (9000 rpm for 30 min).

TEMPO-mediated oxidation of NCC

NCC (21.6 g, 3% w/w in H_2O) was diluted with 9 ml of water. Then TEMPO (10.0 mg) and NaBr (200 mg) were added and the suspension was stirred for 30 min at RT. The TEMPO-mediated oxidation of NCC was initiated by slowly adding 4.9 ml of $NaClO_{(aq)}$ (14 %) over a period of 20 min at RT under stirring. Afterwards the pH of the suspension was set to 10 by adding NaOH (0.5 M) and monitored for the following 50 min. Then the suspension was quenched with 5 ml of MeOH and the pH was set to 7 by adding a HCl solution (0.5 M). The product was filtered by dialysis and freeze-dried by lyophilisation.

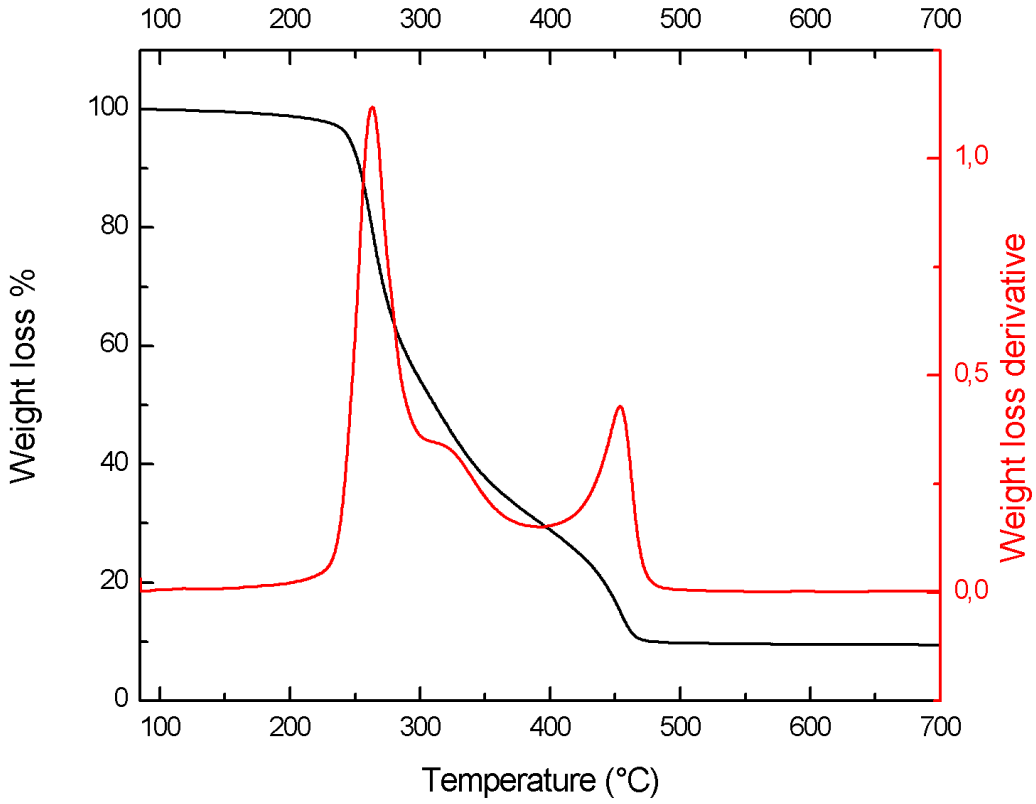

TGA analysis of NCC-COOH.

NCC degree of oxidation

To evaluate the degree of oxidation a conductometric titration was performed for both NCC and NCC-COOH. 10 ml of a standard $HCl_{(aq)}$ solution (0.01 M) were added to a suspension of the analyte (35.1 mg for NCC, 34.5 mg for NCC-COOH) dispersed by sonication in water. A standard $NaOH_{(aq)}$ solution (0.01 M) was added dropwise while following the conductivity behaviour of the solution.

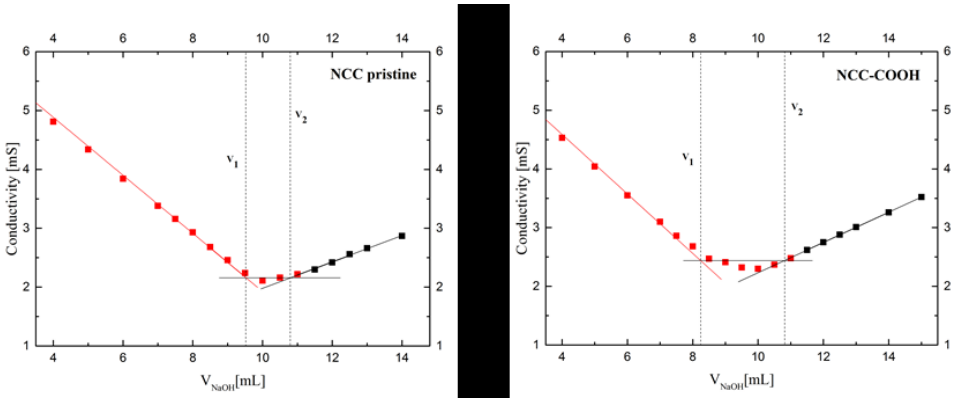

Graphs of the conductometric titration of pristine NCC (left) and NCC-COOH (right).

Preparation of NCC-Fe_3O_4 hybrids

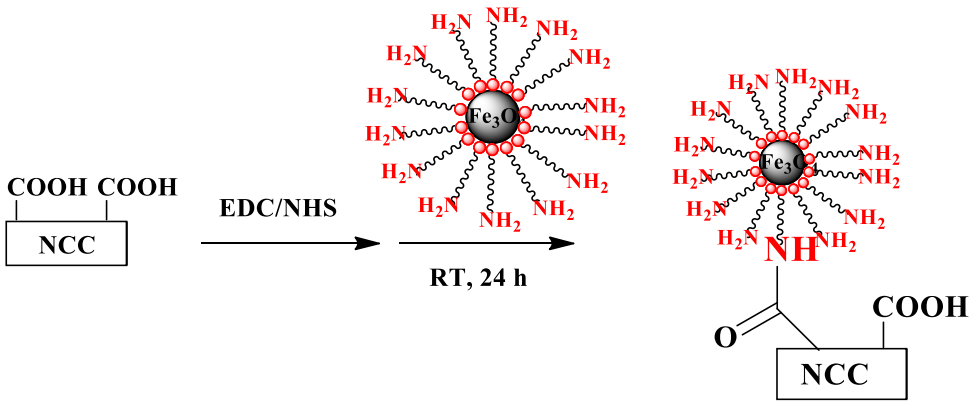

NCC-COOH (150 mg) was dispersed into 30 ml of 50 mM MES buffer. EDC (30.7 mg) and NHS (51.2 mg) were added to the suspension and left under vigorous stirring for 15 min. Afterwards, dopamine-coated Fe_3O_4 Nps (3 ml of a 7.7% w/v dispersion) were added and the reaction was carried out under stirring for 24 h at RT. NCC-Fe_3O_4 hybrids were transferred in a dialysis membrane to eliminate the excess of reagents.

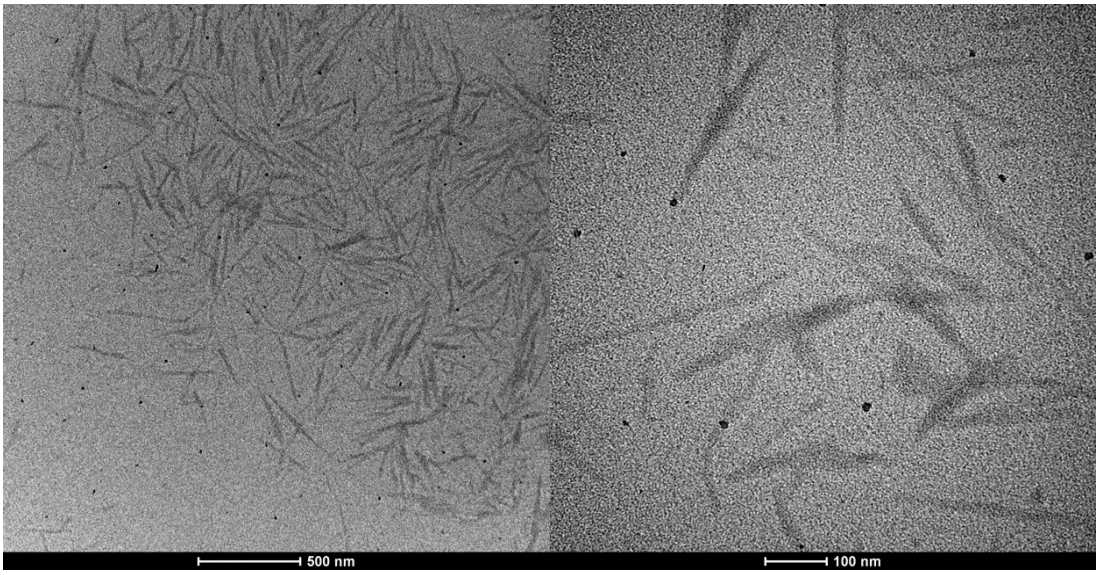

TEM images of NCC-Fe_3O_4 hybrids.

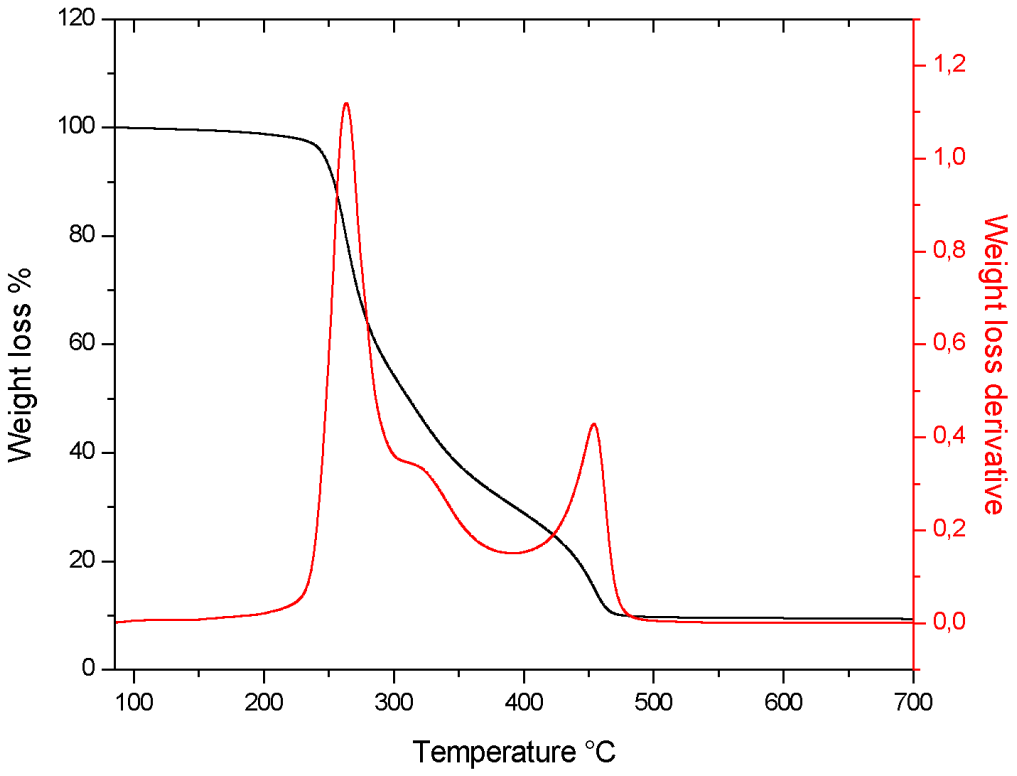

TGA analysis of NCC-Fe_3O_4 hybrids.

Preparation of alginate magnetic beads-sensors

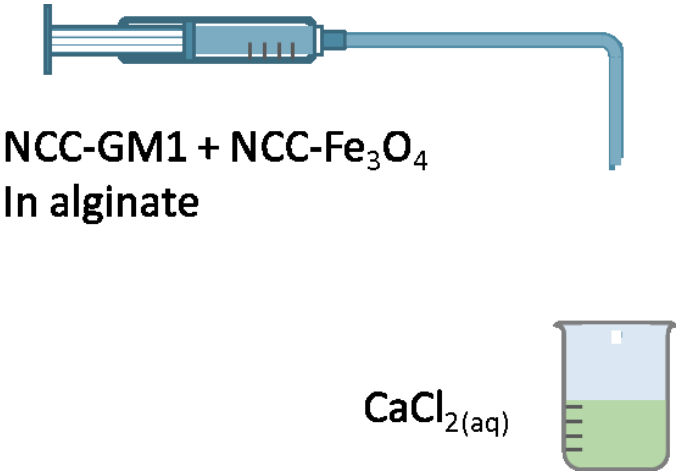

2 ml of the aqueous dispersion of NCC-Fe_3O_4 hybrids were transferred into a vial and the crystals were concentrated on the bottom using a magnet. After the elimination of the supernatant, 5 ml of an alginate solution (1% of sodium alginate in water) were added and stirred for 10 min. Under stirring, 2 ml of the NCC-GM1 dispersion (to be found at page 101) were added. Afterwards, the mixture was ultrasonicated for 10 min (output 2.0, interval: 3 s on, 3 s off) using a microtip to obtain an homogeneous dispersion, that was loaded into a syringe and added dropwise to a solution of $CaCl_2$ (4% w/w in water) under mild stirring. After the addition, beads were left under stirring for 30 min and then washed with water.

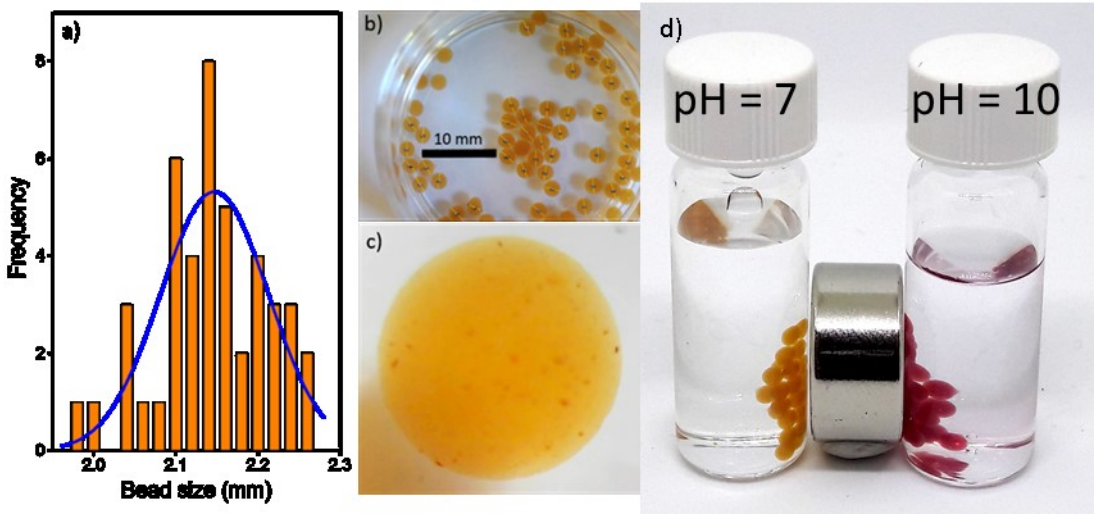

a) Dimensional distribution of b) alginate magnetic beads; c) particular of a single bead; d) answer to magnetic and pH stimuli.

NCC and derivatives as additives for polyurethane foams

NCC from freeze-drying process

NCC aqueous dispersion was freeze-dried directly without any previous processing step. About 250 mL of suspension (3%$_{w/w}$) could be dried in 20 hours.

NCC from evaporation process by heating

Small amounts of NCC aqueous suspension (3%$_{w/w}$) were poured into a Petri dish (10 mL for a Petri dish with a diameter of 5 cm) and placed on a heating plate set to 40°C for 20 hours. Several Petri dishes could be heated in parallel.

NCC from precipitation with acetone

25 mL of aqueous suspension (3%$_{w/w}$) were poured into a centrifuge tube (total volume of 50 ml). 25 mL of acetone were added and the tube was sonicated for 10 minutes. NCC was precipitated by centrifugation (9000 rpm for 40 minutes), the supernatant was eliminated and the precipitate was re-suspended in fresh acetone by sonication. These steps were repeated 5 times, then, after precipitation, NCC was left under N_2 flux for 20 hours.

Functionalization of NCC with 3-aminopropyl-triethoxy silane

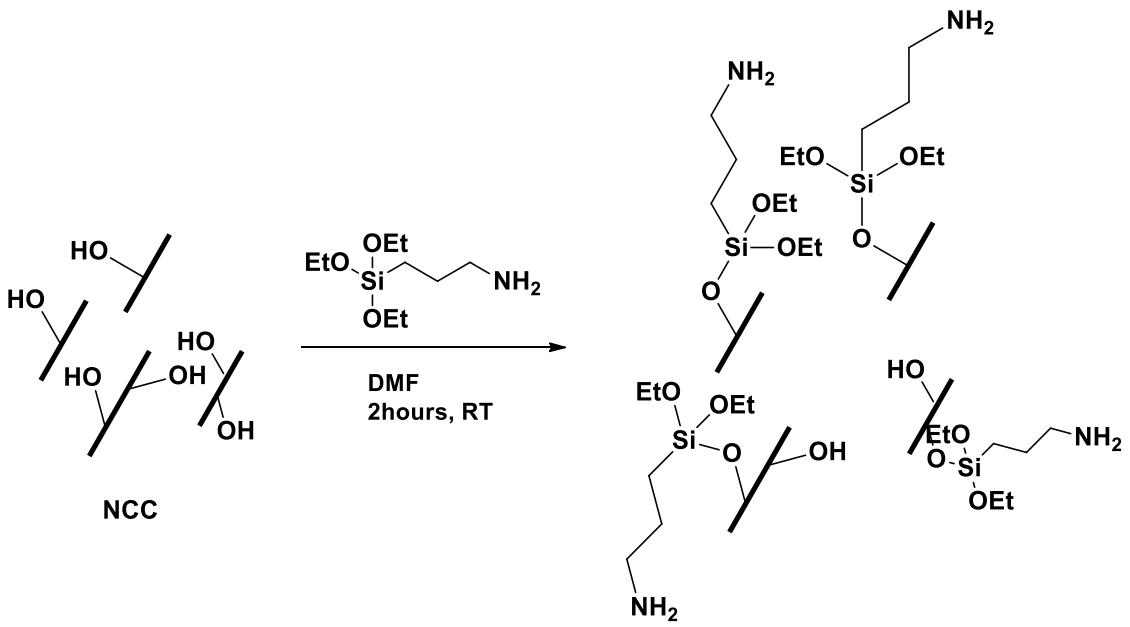

NCC (freeze-dried, 0.2 g) was dispersed in 20 ml of DMF. APTES (0.5 ml, 2.1 mmol) was dissolved in the dispersion and left stirring at RT for 2 hours exposed to the air.

The reaction mixture was then centrifuged and resuspended in fresh DMF three times and three times in fresh methanol. Functionalization was confirmed through Kaiser test, made of three different solutions:

Reagent A) 16,5 mg of KCN in 25 mL of distilled water;

1,0 mL of above solution diluted with 49 mL of pyridine (freshly distilled from ninhydrin);

Reagent B) 1,0 g of ninhydrin in 20 mL if n-butanol;

Reagent C) 40 g of phenol in 20 mL of n-butanol.

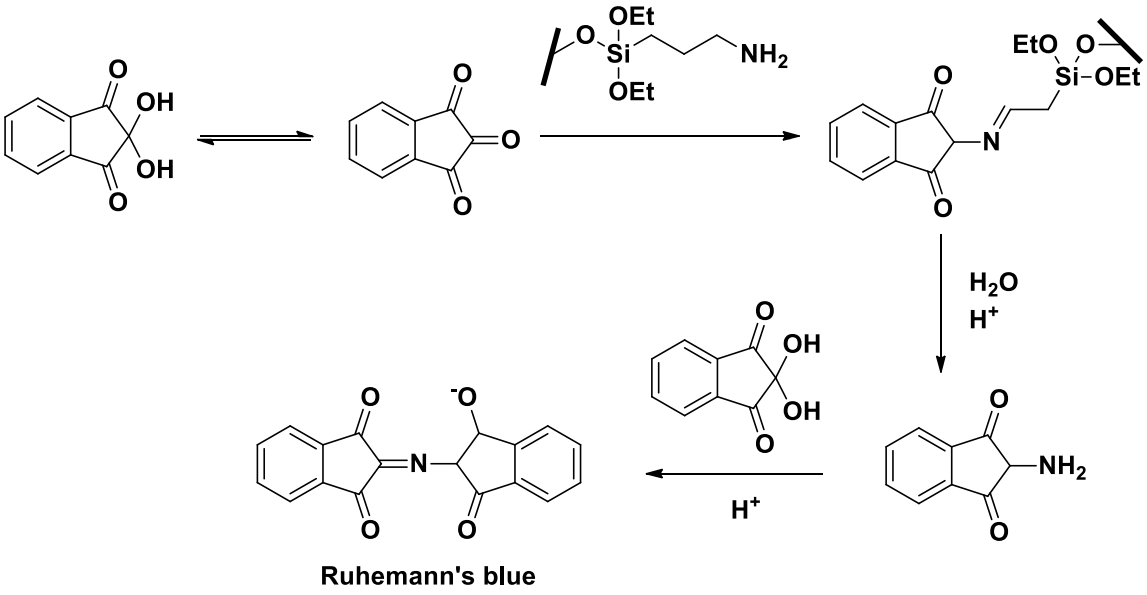

After the test the precipitate was finally dried under vacuum.

Aqueous suspension of NCC-NH_2 (functionalized with APTES) after Kaiser test.

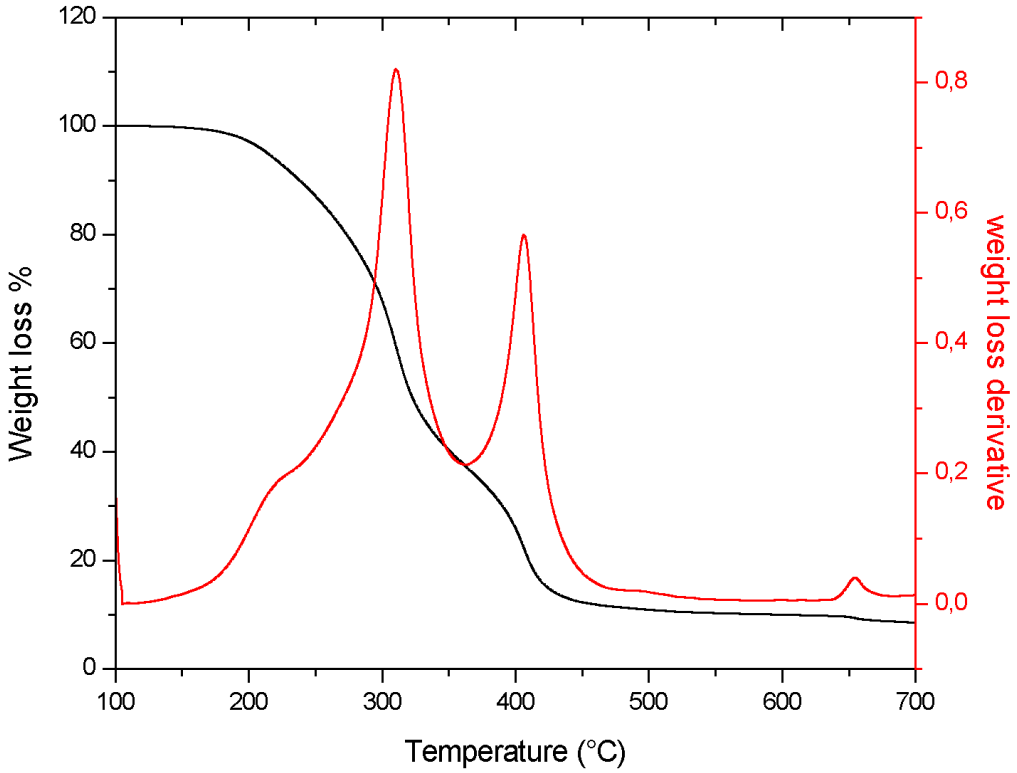

TGA analysis of NCC-NH_2.

Elemental analysis (mass content)

C%	**H%**	**N%**	**S%**
36.59	6.66	5.41	0.53

Functionalization of NCC-NH_2 with fluorescein isothiocyanate

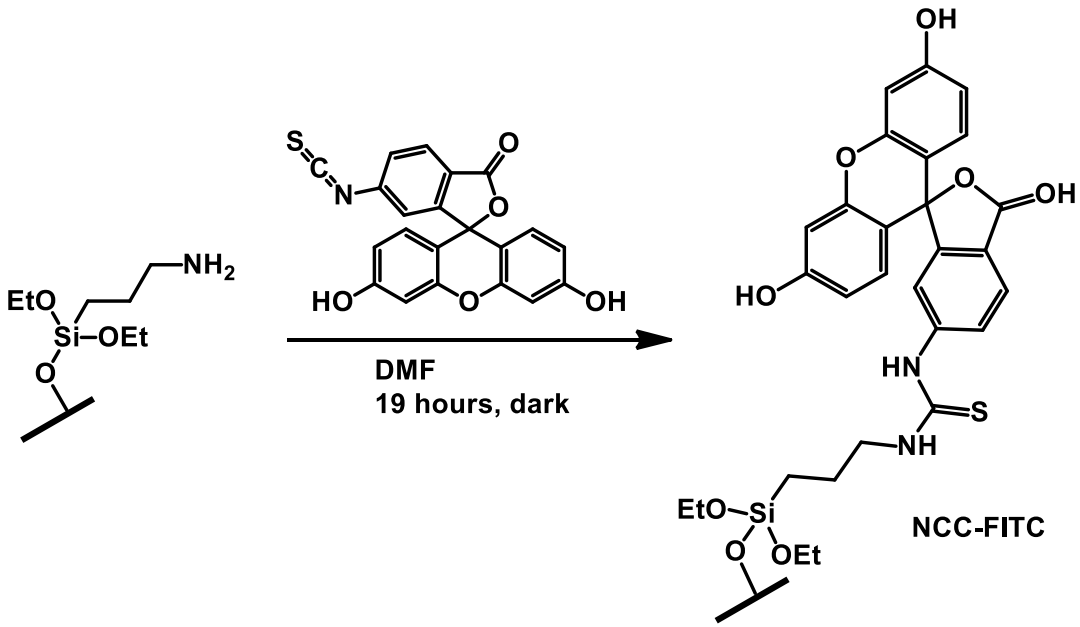

NCC-$SiNH_2$ (freeze-dried, 0.18 g) was dispersed 18 mL of DMF and stirred for 2h. Fluoresceine isothiocyanate (FITC, 24 mg, 0.06 mmol) was added to the dispersion, the flask was plugged and left under stirring for 19 h in dark. The product was centrifuged and resuspended three times in fresh DMF and three times in fresh acetone. After another centrifugation, the precipitate was dried under vacuum.

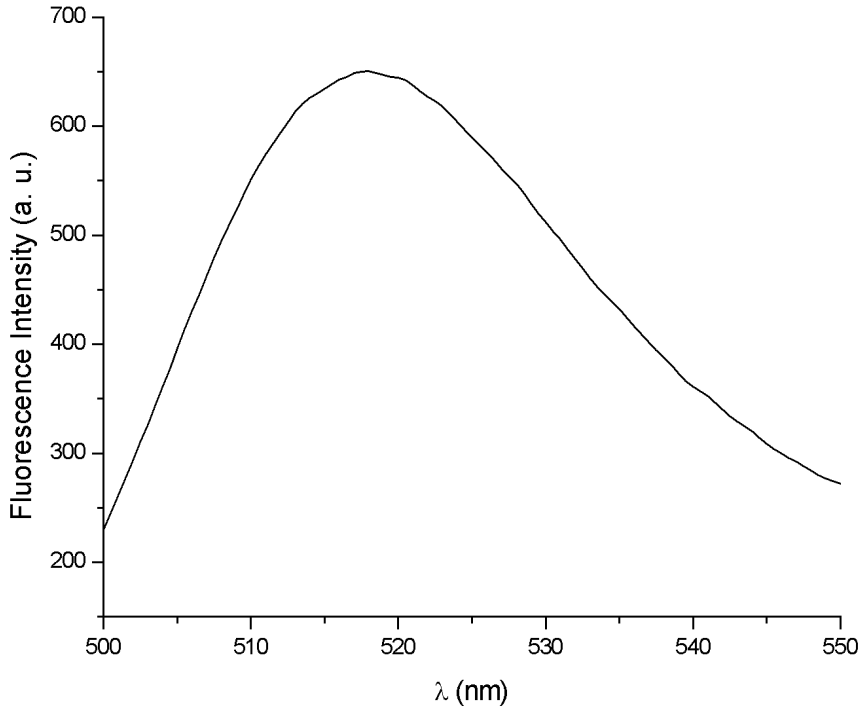

Emission spectra of NCC-FITC dispersed in water (λ_{exc} = 490 nm)

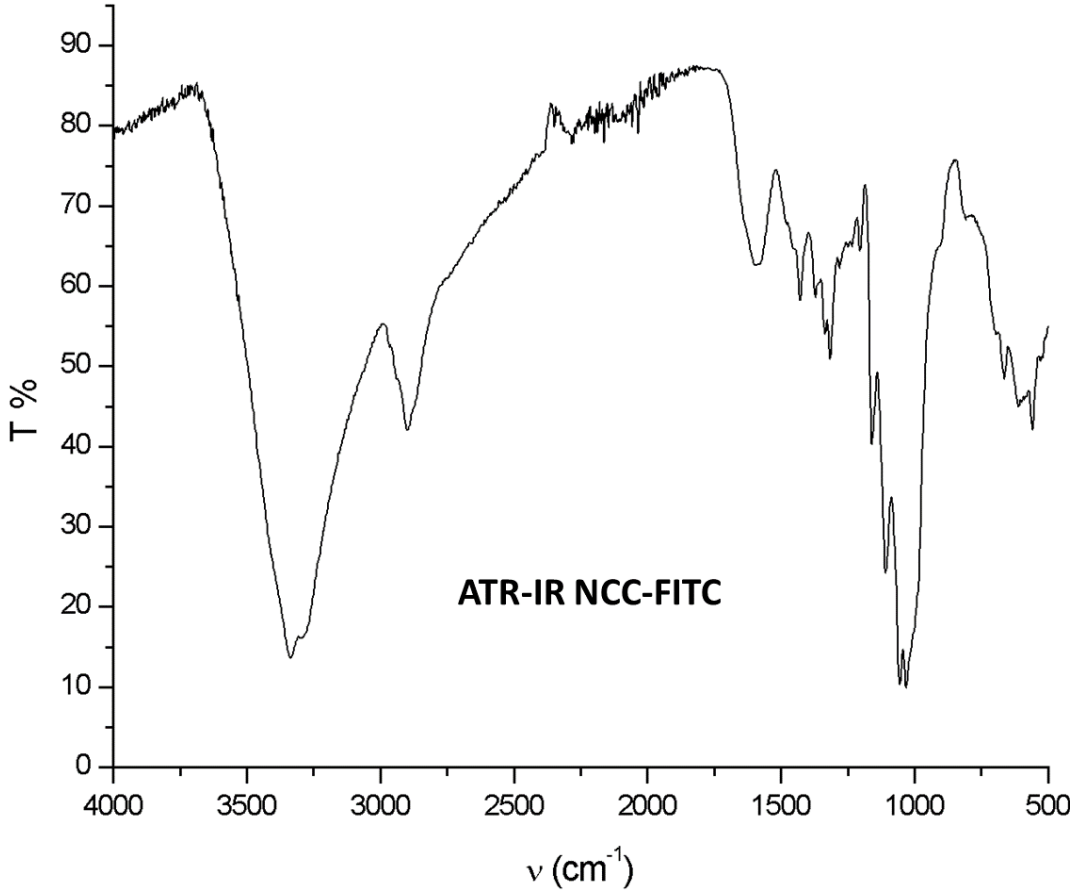

ATR-IR spectrum of NCC-FITC.

Elemental analysis (mass content)

C%	**H%**	**N%**	**S%**
37.54	5.89	1.63	0.42

Functionalization of NCC with tannic acid

The functionalization procedure is taken from literature [42].

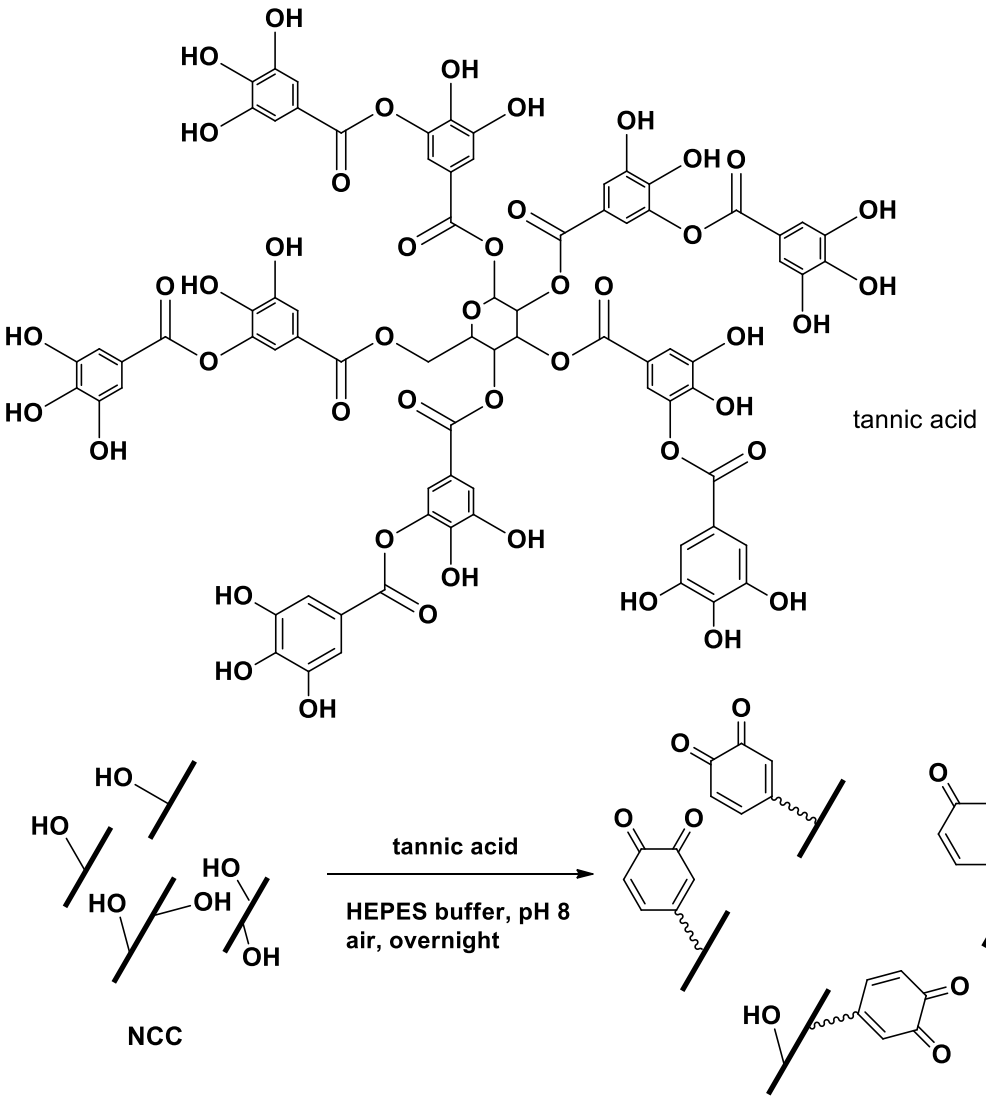

HEPES buffer (0.51 g) was dissolved in 150 mL NCC (2% w/w) aqueous solution and pH was adjusted to 8 with the addition of $NaOH_{(aq)}$ 1 M. Tannic acid (0.15 g) was added and the mixture was continuously stirred overnight, with open flask to provide the presence of oxygen. To eliminate the excess of reagents, the product was dialyzed against deionized water for six days and freeze-dried.

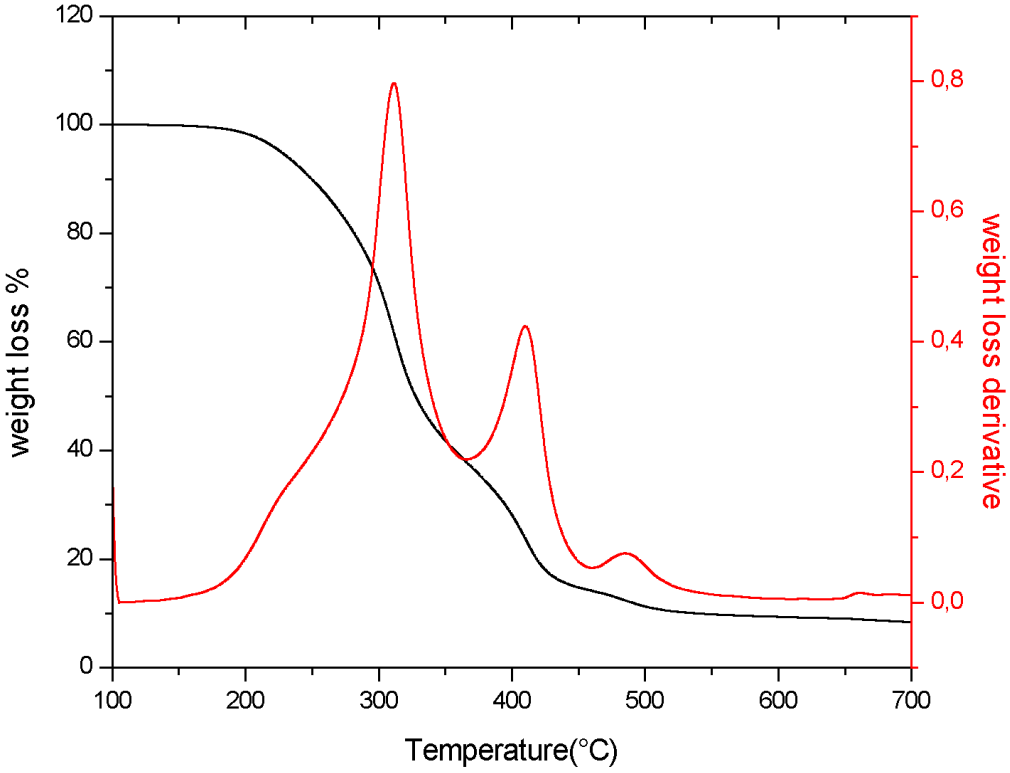

TGA analysis of NCC-TA.

Dispersion of NCC and NCC derivatives in polyols

Polyols were mixed in the ratio optimized in the laboratories of Prof. A. Lorenzetti (ISOTER4537/ISOTER4530/ISOTER842G in the weight ratio of 40/40/20) by stirring. After the homogenization of the mixture, NCC (0.8 g) was added and dispersed using different techniques (sonication, microtip sonication, homogenization) to evaluate the dispersion efficacy. The experiment was repeated also for NCC functionalized with tannic acid and with APTES.

Preparation of polyurethane foams

Polyols were mixed in the ratio optimized in the laboratories of Prof. A. Lorenzetti (ISOTER 4537/ISOTER 4530/ISOTER 842G in the weight ratio of 40/40/20) by stirring. Water (4 ml) was added to NCC, or its derivatives, (0.8 g) then wet NCC was dispersed by homogenization (10 minutes at 10000 rpm) in polyols. After dispersion all the additives were dissolved in the mixture and isocyanate was added last and stirred vigorously for 15 seconds.

Ingredient	Mass (g)
ISOTER4537	20.00
ISOTER4530	40.00
ISOTER842G	40.00
Voranate M600	156.39
DMCHA	1.00
PMDETA	0.30
NCC	0.80
H_2O	4.00
L6900	2.50

Then the mixture was immediately transferred into a mold that was processed in the laboratory of Prof. Lorenzetti.

Preparation of fluorescent polyurethane foams

Polyols were mixed in the ratio optimized in the laboratories of Prof. A. Lorenzetti (ISOTER 4537/ISOTER 4530/ISOTER 842G in the weight ratio of 40/40/20) by stirring. Water (4 ml) was added to NCC (0.52 g) and NCC-FITC (0.28 g), then this mixture was added to polyols and dispersed by homogenization (10 minutes at 10000 rpm). After dispersion all the additives were dissolved in the mixture and isocyanate was added last and stirred vigorously for 15 seconds. Then the mixture was immediately transferred into a mold that was processed in the laboratory of Prof. Lorenzetti.

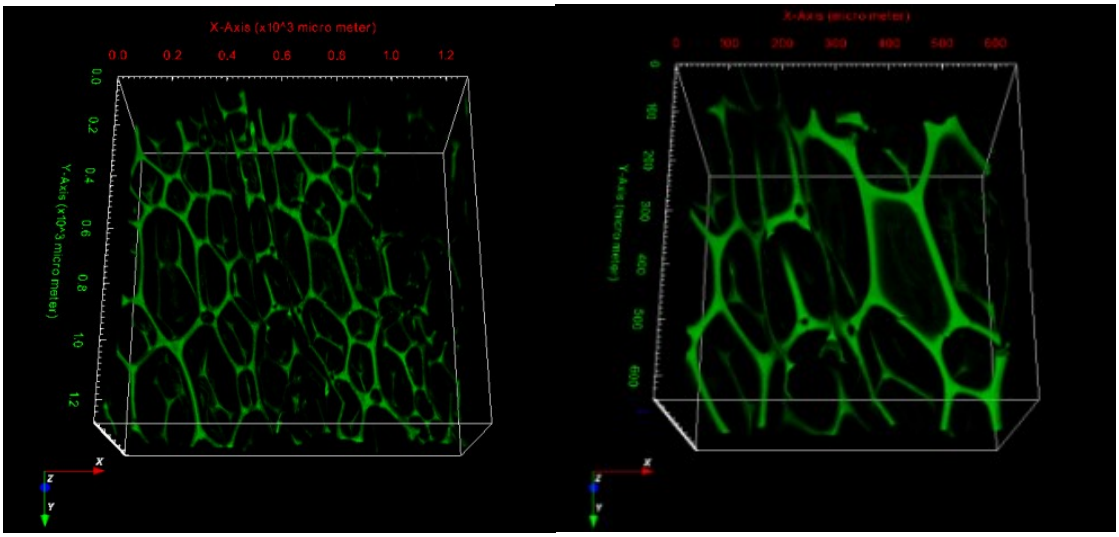

3D reconstruction of images of fluorescent foams obtained by confocal microscopy with 10x objective (left) and 20x objective (right).

References

1. A. Payen, *Comptes rendus*, **1838**, 7, 1052.
2. B. G. Ranby, *Discussions of the Faraday Society*, **1951**, *11*, 158.
3. B. G. Rånby, *Acta Chemica Scandinavica*, **1949**, 3, 649.
4. W. Thielemans, *Nanoscale*, **2014**, *6*, 7764.
5. A. Dufresne, *Nanoscale*, **2014**, *6*, 5384.
6. O. J. Rojas, *Chemical Reviews*, **2010**, *110*, 3479.
7. D. Gray, *International journal of biological macromolecules*, **1992**, *14*, 170.
8. D. G. Gray, *Langmuir*, **1997**, *13*, 2404.
9. A. Dufresne, *Nanoscale*, **2012**, *4*, 3274.
10. D. Mecerreyes, *International Journal of Molecular Sciences*, **2014**, 15, 11922.
11. S. Srivastava, *International Journal of Advanced Research in Engineering and Technology*, **2014**, 5, 70.
12. M. R. Vignon, Cellulose, **2000**, 7, 177.
13. M. R. Vignon, Cellulose, **2006**, 13, 679.
14. M. R. Vignon, *Biomacromolecules*, **2003**, 4, 1417.
15. H. Fukuzumi, *Nanoscale*, **2011**, 3, 71.
16. O. Wolfbeis, *Fresenius Journal of Analytical Chemistry*, **1993**, *346*, 564.
17. O. S. Wolfbeis, *Sensors and Actuators B: Chemical*, **1993**, *11*, 425.
18. O. S. Wolfbeis, *Analytica Chimica Acta*, **1994**, *292*, 41.
19. R. Janoschek, *Dyes and Pigments* **1994**, *24*, 223.
20. O. S. Wolfbeis, *Analytical Chemistry* **1994**, *66*, 3323.
21. D. Randall, S. Lee, The Polyurethanes Book, 2002, Wiley & Sons Ltd., New York (U.S.A.).
22. N. A. Alian, *Journal of Organometallic Chemistry*, **2015**, 791, 99.
23. *US Patent* 5,714.543, **1998**.
24. *US Patent* 5,539,011, **1996**.
25. *US Patent* 6,043,290, **2000**.
26. J. Lin, *Trends in Analytical Chemistry*, **2000**, *19*, 541.
27. L. González, *Anal Bioanal Chem* **2008**, *392*, 1411.
28. O. S. Wolfbeis, *Analytica Chimica Acta* **1994**, *292*, 41.
29. O. S. Wolfbeis, *Sensors and Actuators B: Chemical* **1993**, *11*, 425.
30. M. Bagheri, *Sensors and Actuators B: Chemical* **2003**, *90*, 143.
31. T. Carofiglio, *Chemical Communications*, **2014**, 50, 9493.
32. M. Guglielmi, *Journal of Sol-Gel Science and Technology*, **1994**, 3, 1, 47.
33. L. M. Bronstein, *Applied Materials and Interfaces*, **2015**, 7, 27254.
34. O. J. Rojas, Biomacromolecules, **2017**, 18, 898.
35. F. Schüth, *Angewandte Chemie International Edition*, **2007**, 46, 1222.
36. S. J. Xiao, *Langmuir*, **2011**, 27, 12058.
37. S. Djebbar, Langmuir, **2010**, 26, 809.
38. D. Cantero, *Journal of Bioscience and Bioengineering*, **1999**, 88, 686.
39. J. Youngblood, *Chemical Society Reviews*, **2011**, 40, 3941.
40. E. Kaiser, *Analytical Biochemistry*, **1970**, 34, 595.

41. W. J. Grigsby, *Journal of Wood Chemistry and Technology*, **2009**, 29, 305.
42. E. D. Cranston, *Sustainable Chemistry*, **2017**, 5, 5018.

Chapter 3

Controlled Nucleation and Crystallization of Small and Ligand-Free ZnS Nanoparticles via a Low Temperature and Easy Microfluidic Approach

Introduction

Microfluidic reactors (MRs) are based on the flow of minute amounts of fluids within micrometer-size channels. In the micro size domain, a better control of chemical reactions, in terms of selectivity, suppression of by-products formation and safer processing, is achieved because thermal and mass transfer processes are enhanced. In addition, MRs allow for both optimization, through a rapid screening of reaction parameters, and upscaling of synthetic methods using the numbering-up concept, in which several MRs work in parallel.

Although these unique features of MRs have been mainly applied in preparative organic synthesis, in the last few years MRs have been used also for the preparation of nanomaterials[1]. In particular, the integration of nanoparticles (NPs) and MR technologies offer tremendous opportunities for the possibility to control NPs nucleation and growth that, in turn, affect their size, size-distribution and composition. The enhanced heat transfer in MRs reduces the impact of thermal effects on diffusion and growth of NPs, whereas surface tension, electrostatic effects, van der Waals interactions and surface roughness of channel walls are relevant to govern diffusion and type of nucleation (homogeneous vs. heterogeneous) that are particularly important for size- and shape-control of nanomaterials. Particularly in the case of inorganic colloids, where size, shape and crystalline structure play a major role in affecting relevant functional properties[2], pursuing a fine control on reagents flows and mixing within a MR becomes pivotal to gain control on the nucleation and/or growth stages.

In this study, we address the nucleation and growth of extremely small ZnS NPs by using a simple microfluidic set-up in which aqueous solutions of the two ZnS precursors (Zn(NO3)2 and Na2S) were mixed at room temperature to yield a controlled precipitation of the target colloid.

Nanostructured ZnS is well known to be a direct wide-gap semiconductor (3.72 eV in its cubic phase and 3.77 eV in its hexagonal one) and, because of its tunable photophysical and electrochemical properties, it has been proposed for a broad

range of applications, including catalysis and photocatalysis, nonlinear optics, optoelectronic devices, sensors, lasers[3-7] and, for its low cytotoxicity, optical bioimaging.

ZnS occurs mainly in two main polymorphs, namely sphalerite and wurtzite[8] whose interconversion and phase evolution have been the topic of several investigations [7,9]. Sphalerite is stable at room temperature (cubic, spatial group F-43m), whereas hexagonal wurtzite (spatial group P63mc) becomes stable above 1023°C[8]. Although several synthetic approaches have been developed to prepare ZnS nanostructures displaying different shape and morphologies [7], to our knowledge only one synthesis of pure ZnS nanocrystals under continuous flow conditions was reported earlier, using thioglycerol as a capping agent[10]. Microfluidics was employed to prepare different metal sulfide NPs, such as PbS [11] or CdS [12] and ZnS/ZnSe and ZnS/CdSe core-shell nanosystems. Therefore, this is the first study that reports the synthesis of ZnS in flow, without stabilizing ligands or surfactants and by using non-toxic, earth-abundant and cheap precursors. Our optimized approach gives stable suspensions of "naked" ZnS that, for many applications, is a prerequisite to exploit specific properties (e.g., luminescence). The absence of ligands is expected to influence remarkably the kinetics of NPs nucleation and growth[7].

Results and discussion

The preparation of small, surfactant-free, crystalline ZnS nanoparticles was accomplished by the flow reactor shown in figure 1. A balanced precursors feeding ensured by two reciprocating syringes or by two common syringes pumps, the use of a 90° T-junction for highly effective turbulent mixing and a short (few seconds) residence time after the junction at room temperature, allowed to isolate tiny ZnS nanocrystals. They were collected as a slurry and kept at low temperature to avoid any further growth or ripening. Within minutes, from the slurry separated a cloudy floc that was centrifuged.

The residue was washed with water and suspended again in water to give an opalescent colloidal suspension which was stable for several days, despite the absence of a surfactant. It is reasonable to assume that repulsive electrostatic interactions, through preferential absorption of hydrogen sulfide anions on the surface of ZnS nanocrystals, stabilize the colloidal suspension that, at this stage, has a pH between 12 and 10. Hydrogen sulfide anions were removed by concentrating and

drying the suspension, likely through H_2S extrusion. XPS analysis (vide infra) showed that the nanocrystals are rich in zinc, rather than in sulfur. Re-dispersion of this dry ZnS in water generates neutral to slightly acidic suspensions that typically precipitates in a few minutes for the absence of electrostatic stabilization.

Flow rate and precursors molar ratio were independently varied to assess the effect on the NPs characteristics. Table 7 shows that the variation of flow rate or concentration only slightly affects the size of the final colloids.

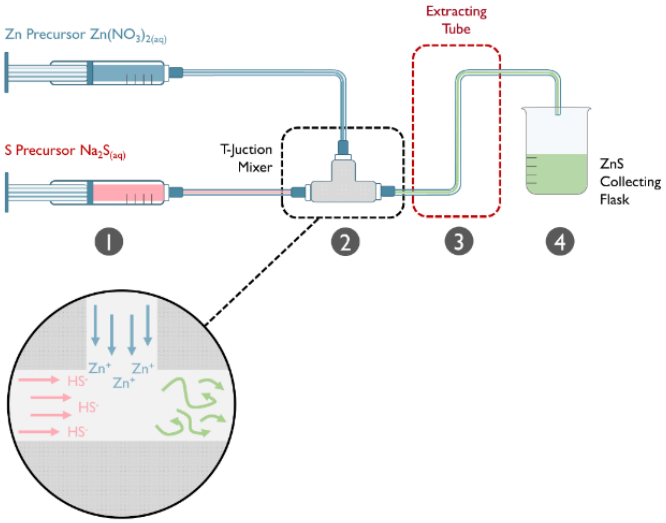

Figure 72. Microfluidic set-up for the synthesis of ZnS colloidal suspensions: (1) Feeding via twofold-syringe pumps; (2) T-junction; (3) variable length reaction tube; (4) quenching zone/product collection.

In addition, a model batch synthesis (SE001) was carried out, for comparison, by dropwise addition of the zinc precursor to an ice-bath pre-cooled Na_2S solution under vigorous stirring, leading to larger NPs and, correspondingly, to a lower specific surface area (the detailed post-synthetic workup operations are described in the Experimental Section).

Sample	Flow rate (ml/min)	Zn^{2+} conc. (M)	S:Zn ratio (mol/mol)	Average diameter[1] (nm)	Average diameter[2] (nm)	BET area (m^2/g)
MF001	2	0.1	2	4.4	<10	-
MF007	1.2	0.01	5	5.1	6.6	298 ± 4
MF008	1.2	0.1	2	4.8	~5	265.5 ± 0.9
SE001[a]	--	--	--	6.2	7.8	225.0 ± 2.2

Table 7. Experimental parameters and obtained properties of selected synthetized samples. (a) batch reaction performed as comparison. [1]As determined by size-strain analysis via whole pattern fitting of XRD pattern. [2]As determined by TEM micrographs.

According to the LaMer model[13] and its kinetic description by Sugimoto[14-15] and Chu[16], nucleation and growth of ZnS NPs are consecutive rather than simultaneous events; this promotes the formation of many nuclei growing further in a second phase. In the batch synthesis of ZnS, the dropwise addition of $Zn(NO_3)_2$ to a stirred Na_2S solution gives larger nanocrystals than those isolated when the reaction is carried out within a flow reactor. The key feature to consider here is mixing. Mixing of reagents in a T-junction of a flow reactor is much faster than in a batch reactor for the short diffusion path within the microchannels thus promoting supersaturation and an increased number of nucleation centers that, after a short residence (few seconds) time to minimize growth through aggregation or ripening phenomena (see tube 3, Scheme 1) and the quenching step (beaker 4, Scheme 1), yield the observed small ZnS nanocrystals, as evidenced by TEM micrographs reported in figure 73. At the same time, fast mixing limits the incidence of concentration gradients that would led to random (both timely and spatially) nucleation bursts.

As introduced above, according to the meanwhile outdated and oversimplified Classical Nucleation Theory (CNT)[17], the most acknowledged mechanism for the formation of particles from a liquid environment is the nanoparticle formation process proposed by LaMer in which four stages are involved: supersaturated solute formation, nucleation, growth, and aggregation. The formation of many nuclei in a short burst determined by the supersaturation conditions is followed by the growth of particles. This “releases” the supersaturation constraints below the critical nucleation concentration and freezes the number of nuclei formed, whereas the growth of the particles continues until all solute has been consumed, thus lowering the overall free energy of the system (particles and solutes). In the absence of an effective stabilization (either steric or electrostatic), van der Walls attraction-driven

aggregation of individual nanoparticles induces flocculation, coagulation and eventually precipitation out of the solution. To achieve stable suspensions of nanoparticles with given size and size distribution, one of the following requirements should be fulfilled: i) stop the growth (e.g. via reagent depletion) when particles are still in a specific nanometer size range and ii) avoid particle aggregation. In our flow system, where mixing is fast, nucleation occurs rapidly while nanocrystals grow in a compositionally homogeneous environment through (likely oriented) addition of further precursors and not via uncontrolled agglomeration. In this sense, the synthesis of NPs in flow discloses exciting perspectives. Several studies suggested that homogeneous reaction and particle nucleation are diffusion-limited and occur at the boundary between the laminar streams of reagents, while the slower activation growth process occurs on a longer (seconds) time scale, thereby separating the nucleation and growth stages[18]. The key parameters governing both nucleation and growth of nanocrystals have been thoroughly investigated by De Mello and co-workers that in a recent study[19] highlighted how MRs provide a unique environment for elucidating reaction kinetics and mechanisms.

XRD patterns of the dry ZnS powder showed the exclusive presence of sphalerite. Rietveld refinement (whole pattern fitting, MAUD[20]) gave an average NPs diameter of 5 nm. It is worth noting that smaller ZnS NPs were reported in the literature[21] which, however, were prepared in the presence of ligands and/or surfactants to hinder their growth. TEM and XRD analyses (table 7) show that single nanoparticles are single crystallites as a further confirmation that homogeneous nucleation and a limited aggregation/ripening is taking place in the flow reactor after the fast and efficient mixing step of the reagent in the T-junction.

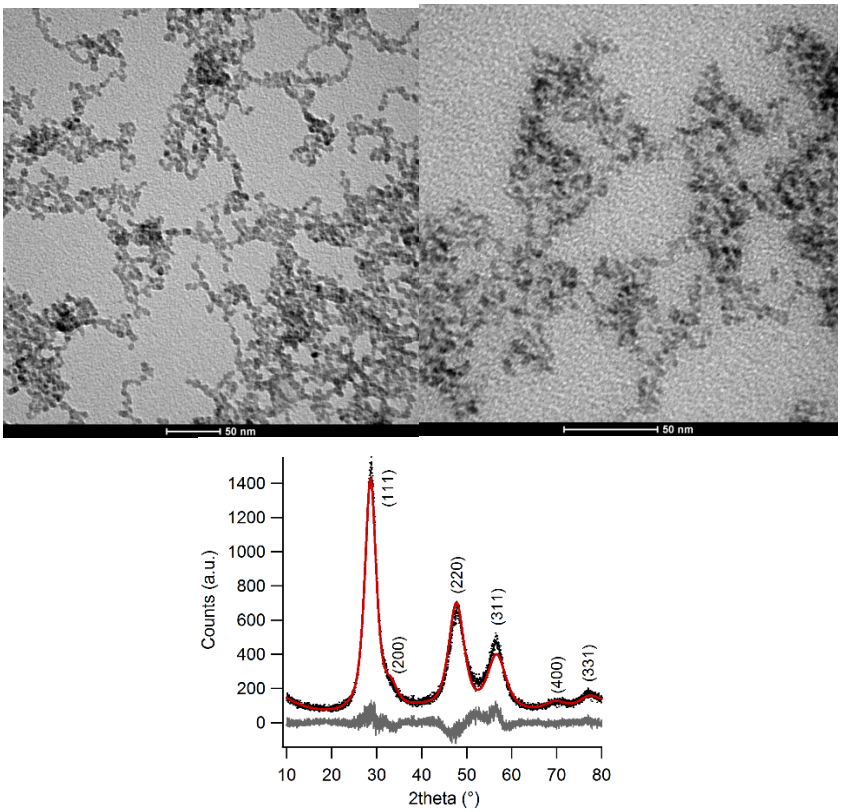

Figure 73. Left, TEM image of the MF007 sample. Right, TEM image of the MF008 sample. Center, refined XRD pattern of the MF001 sample.

Noticeably, the dried ZnS powder has a very large specific surface area, reaching almost 300 m^2/g for sample MF007, if compared to other samples of ZnS NPs prepared by precipitation protocols in batch[22].

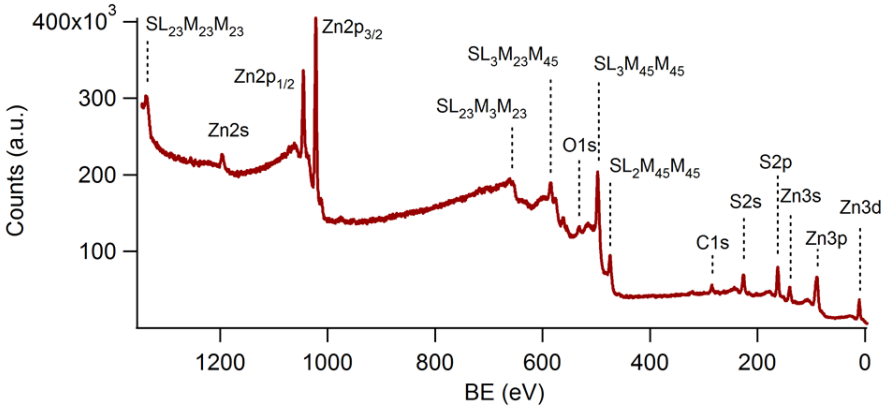

Figure 74. XPS survey spectra of sample MF008

The surface of the isolated nanoparticles was analyzed by XPS. A representative survey spectrum of sample MF008 is reported in Figure 74, showing the exclusive presence of zinc and sulfur, beside the ubiquitous presence of carbon and oxygen from spurious contamination. The atomic percentages determined by the selected

O1s, C1s, S2p and Zn2p regions are C at %: 12.4, O at%: 6.65, S at %: 32.3, Zn at %: 48.7, showing a slight excess of zinc on the surface with respect to the expected stoichiometric ratio (1.5 vs 1), as reported earlier[23]. The binding energy of the main sulfur region, S2p, has a value of 161.5 eV which agrees very well with data previously reported (S2p3/2 = 161.6 eV)[24,26]. This finding confirms that the NPs surface is exclusively made of zinc sulfide with no passivation by sulfates. The binding energy of the Zn2p3/2 main component is at 1021.9 eV, a value which is in line with data for ZnS, whereas the corresponding Auger parameter is at 2011.1 eV. Both values are compatible with ZnS (Zn2p3/2 = 1022.0 eV, Auger parameter= 2011.5 eV)[24].

ZnS is an important photocatalyst for the hydrogen evolution reaction (HER), and its light harvesting properties (especially in the visible fraction of the spectrum) can be modulated, e.g., by introducing surface defects. For examples, S vacancies where shown to decrease the band gap[27]. Since XPS measurements hinted towards such a situation in the investigated samples, their photocatalytic performances were investigated, following the procedure reported in the Experimental Section (using Na_2S and Na_2SO_3 as sacrificial agents against photocorrosion). The activity of the samples was evaluated using both the full spectrum (thus including the UV fraction of the emitted spectrum) or the visible fraction only (radiation with $\lambda < 420$ nm was omitted), see Table 8.

In the case of visible light irradiation only, the samples show similar rates of H_2 production, with MF001 showing a higher value. Compared to the literature[27], the values obtained are quite remarkable. For example, ZnS prepared by hydrothermal methods and tested under similar conditions to ours, reportedly was producing H_2 with rates of 0.465 mmol h^{-1} g^{-1}[28], and was achieving higher values (3.31 mmol h^{-1} g^{-1}) only in the presence of 4 wt% Au as cocatalyst[29].

When the whole spectrum is taken into consideration, the samples show a different trend, with MF008 showing the highest value. Interestingly, the batch sample is able to perform extremely well, even though it has a larger average size and lower surface area.

Sample	HER full spectrum (mmol h^{-1} g^{-1})	HER Visible only (mmol h^{-1} g^{-1})
MF001	34	1.52
MF007	36.7	1.37
MF008	45.7	1.35
SE001	43	1.33

Table 8. Photocatalytic hydrogen production rates of ZnS catalysts suspended in aqueous solution.

In conclusion, a controlled nucleation and crystallization of pure sphalerite ZnS colloids was achieved under continuous flow conditions at room temperature, in water and without the use of any stabilizing ligand. The colloids, characterized by X-Ray Photoelectron Spectroscopy (XPS), nitrogen physisorption, X-Ray diffraction (XRD), Transmission Electron Microscopy (TEM), display an average size of 5 nm and an impressively high specific surface area of 287 m^2/g that likely contributes to the good photocatalytic properties in hydrogen evolution reaction (HER) tests. The microfluidic approach enables a much tighter control on relevant parameters affecting nucleation and growth, thus disclosing the possibility to produce, in a simple and reproducible fashion, ligand-free, stable and crystalline colloids.

Experimental part

Batch route

In the first batch synthetic approach, the Na2S solution was kept vigorously stirred in an ice bath to ensure a stable 0°C reaction temperature overtime, while the Zn solution was added dropwise (roughly one drop every two seconds). The resulting slurry was kept stirred for one hour and the product was isolated by centrifugation (10 minutes at 10000 rpm). The resulting white solid was than washed with water, sonicated and centrifuged for a total of four cycles. The final powder was dried in a vacuum desiccator at room temperature.

Microfluidics route

For these syntheses, a simple T-shaped single-mixer setup was designed, realized and employed. The flow system was fed using initially a double-syringe pump, but a reciprocating syringe pump (Syrris Asia Syringe Pump) was lately preferred to allow an unstopped flow process. Zinc nitrate hexahydrate and sodium sulfide nonahydrate milliQ water solutions were employed as precursors, each one being separately pumped into the reactor. The obtained slurry was collected in ca. 200 ml of mildly stirred cold water kept in an ice bath. The product was left to settle down in order to easily remove a large fraction of the mother liquor, than the obtained slurry was centrifuged and further washed with milliQ water. The final powder was dried in a vacuum desiccator at room temperature.

XPS spectroscopy

Powder samples were investigated by XPS with a Perkin–Elmer ϕ 5600ci instrument using Al-Kα radiation (1486.6 eV), operating at 350 W. The working pressure was less than $5 \cdot 10^{-8}$ Pa. The calibration was based on the binding energy (BE) of the Au $4f_{7/2}$ line at 83.9 eV with respect to the Fermi level. The standard deviation for the BE values was 0.15 eV. Reported BEs were corrected for charging effects and the BE value of 284.6 eV was assigned to the C1s line of carbon. Survey scans were obtained in the 0–1350 eV range (pass energy 187.5 eV, 1.0 eV $step^{-1}$, 25 ms $step^{-1}$). Detailed scans (29.35 eV pass energy, 0.1 eV $step^{-1}$, 50–150 ms $step^{-1}$) were recorded for O1s, C1s, Zn2p, ZnLMM, S2p, and S2s. The atomic composition, after a Shirley-type background subtraction[30] was evaluated using sensitivity factors supplied by Perkin–Elmer. Peak assignment was carried out according to literature data.

XRD diffraction

The XRD patterns on the ZnS nanostructures were collected with a Bruker D8 Advance Diffractometer equipped with a Göbel mirror by using the Cu-Kα radiation. The angular accuracy was 0.0010° and the angular resolution was better than 0.01°. All the experimental data were analyzed by using the Material Analysis Using Diffraction (MAUD) software package[20], to deduce quantitative crystallographic and microstructural information by using the Rietveld refinement method.

TEM microscopy

TEM micrographs where obtained with a FEI Tecnai G12 microscope operating at 100 kV, equipped with a OSIS Veleta camera. Samples were prepared by suspending the dried powders in ethanol through sonication and then deposited on 300 mesh lacey carbon coated copper grids. Particles were manually segmented and measured using the ImageJ package. The obtained distributions were fitted using the log-normal distribution.

Photocatalytic H2 evolution

All photocatalytic experiments were performed in a home-built air-tight photocatalytic setup in a side-illuminated PEEK cell[31]. A 500 W Hg (Xe) lamp was used as the light source, and the amount of H_2 produced during the experiments was detected with an online GC-TCD (ShinCarbon column) with N_2 as the carrier gas. Therefore, the amount of produced hydrogen was determined as a function of time to compare the photocatalytic activities among samples. In a typical test, 10 mg photocatalyst was dispersed under sonication in 50 mL sacrificial agents solution (0.25 M Na_2S and 0.35 M Na_2SO_3) and transferred into the PEEK cell to generate a photocatalyst loading of 0.2 g/l. Before each test, air in the system was removed by evacuation three times. Then the activity measurements were carried out under constant stirring with automated sampling of the gaseous products with 12 min intervals. The temperature of the solution was maintained at 20°C by constant temperature circulating water.

References

1. C. S. S. R. Kumar, *Small*, **2008**, 4, 698.
2. S. Polarz, *Advanced Functional Materials*, **2011**, 21, 3214.
3. D. Golberg, *Critical Reviews in Solid State and Materials Sciences*, **2009**, 34, 190.
4. X. Fang, *Advanced Functional Materials*, **2013**, 23, 3701.
5. D. Golberg, Advanced Materials, **2009**, 21, 2034.
6. D. Golberg, Progresses in Materials Sciences, **2011**, 56, 175.
7. S. J. Dhoble, *Crystal Growth & Design*, **2017**, 17, 381.
8. A. F. Holleman, E. Wiberg, *Lehrbuch der Anorganischen Chemie*, Walter de Gruyter, Berlin/New York, **1995**.
9. S. Gross, *Inorganic Chemistry*, in press.
10. S. Kulkarni, Nanotechnology, **2008**, 19, 245613.
11. A. J. deMello, *Small*, **2015**, 11, 4009.
12. R. F. Ismagilov, *Lab on a Chip*, **2004**, 4, 316.
13. V. K. LaMer, Industrial & Engineering Chemistry, **1952**, 44, 1270.
14. T. Sugimoto, *Monodispersed Particles*, Elsevier, Amsterdam, **2001**.
15. T. Sugimoto, *Colloids and Surfaces A: Physicochemical and Engineering Aspects*, **2000**, 164, 183.
16. Peters, *Journal of Physical Chemistry A*, **2017**, 121, 7511.
17. H. Cölfen, *Mesocrystals and Nonclassical Crystallization*, Wiley VCH, Weinheim, **2008**.
18. T. A. Michalske, Lab on a Chip, **2007**, 7, 908.
19. A. J. deMello, Accounts of Chemical Research, **2017**, 50, 1248.
20. L. Lutterotti, *Beam Interaction With Materials and Atoms*, **2010**, 268, 334.
21. B. R. Ratna, Physical Review B, **1999**, 60, 9191.
22. I. Tsuji , Journal of Photochemistry and Photobiology A, **2003**, 156, 249.
23. N. Dengo, *Master thesis*, **2015**, supervisor S. Gross.
24. NIST Database.
25. S. Gross, *European Journal of Inorganic Chemistry*, **2015**, 4, 706.
26. M. Nogues, *An J. Phys. Chem. Solids*, **1989**, 50, 269.
27. J. J. Wu, *Powder Technology*, **2017**, 318, 8.
28. M. H. Whangbo, *Scientific Reports*, **2015**, 5, 8544.
29. J. Yu, *Applied Materials and Interfaces*, **2013**, *5*, 1031.
30. D. A. Shirley, Physical Review B, **1972**, 5, 4709.
31. E. J. M. Hensen, Inorganic Chemistry, **2015**, 54, 9491.

Chapter 4

Continuous-Flow Selective Monobromination Meso-Tetraphenylporphyrin in β-Pyrrolic Position

Introduction

Porphyrins and related compounds are a class of macrocycles that play a lead role in a variety of research areas such as catalysis, molecular recognition, solar energy conversion, material science and photo-medicine.[1] This is due to their outstanding optical and electronic properties that can be also finely tuned by a judicious choice of the electronic and steric properties of the peripheral substituents as well as by metalation of the porphyrin inner core. The unique porphyrin features have been imparted by covalent conjugation to a variety of nanomaterials such as carbon-based nanomaterials (fullerenes, carbon nanotubes, graphenes, carbon dots), biopolymers (nanocrystalline cellulose, nanofibrillated cellulose)[2], gold and silica nanoparticles, glass surfaces, transition metal oxides and so long. Finally, multiporphyrinic assemblies built both covalently or supramolecularly by hydrogen bonding and/or metal-ligand interactions have been designed to mimic the natural photosynthetic systems and to produce hollow structures capable to encapsulate various guests.[3] All the above applications require the synthesis of porphyrin compounds precisely designed, often without lose sight on scale, purification and cost, as nicely commented by M. O. Senge[4] in his recent feature article on porphyrin functionalization. Indeed, up-scaling the synthesis of a porphyrin derivative can be a complex duty, due to the low yields generally observed, and to the extensive use of chromatography for purification which is unpractical on large scale. Thus, a synthetic path that works properly in microgram scale must be completely redesigned for commercial scale production.

The emerging microreactor (MR) technology is an enabling technology that has a great potential for intensification of synthetic processes.[5] Indeed, due to the micrometric dimension of the MR channels, thermal and mass transfer are enhanced thus allowing for a better control of chemical reactions in terms of selectivity, suppression of by-product formation and safer processing. In addition, MR technology enables rapid screening of reaction parameters for an easiest optimization and for the production of lead compounds. The main benefit of the MRs is their scalability using the numbering-up concept, namely several MRs are placed in parallel thus

maintaining the mass and thermal transport phenomena constant without the need a further optimization of the process.

Despite the potential of MRs there are, at our knowledge, only two reports about their use for porphyrin synthesis. K. T. de Oliveira and co-workers[6] reported the one-pot synthesis of several symmetrically meso-substituted porphyrins under continuous flow conditions and demonstrated the scalability of the process up to 13.9 gr per day, namely more than 5 kg per year, a remarkable amount for this fine chemical. N. Stock and co-workers[7] reported gram-scale synthesis of two porphyrin-based metal-organic frameworks containing Gallium or Indium using a MR set-up to precisely control the nucleation and growth step and ultimately the size and the porosity of the nanocrystals. Even more surprisingly, so far there are no reports about the use of MRs for porphyrin post-functionalization. Certainly, post-functionalization of the meso and β-pyrrolic peripheral positions of the porphyrin framework is a commonly pursued synthetic strategy for the construction of elaborated porphyrin derivatives. For example, one of the best performing Greatzel-type solar cell reported so far employs a porphyrin photosensitizer obtained by modification of meso-tetraphenyl porphyrins at the β-pyrrolic position with functional groups with extended β-systems.[8]

Herein we report the continuous-flow synthesis of the mono-β-brominated meso-tetraphenyl porphyrin derivative, TPPBr, a very useful synthon for grafting the macrocyclic porphyrin framework with a variety of moieties by metal-mediated cross-coupling carbon-carbon and carbon-heteroatom reactions, as recently reviewed.[9]

Results and discussion

Bromination at the pyrrolic β-position of meso-tetraphenyl porphyrin, TPP, is generally carried out with N-bromosuccinimide, NBS as bromide source (figure 75).[10]

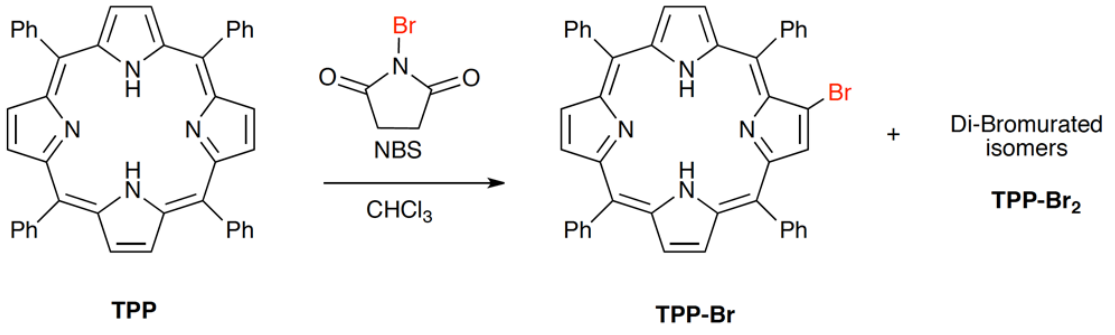

Figure 75. General equation for TPP bromination with NBS.

Porphyrin mono-bromination is generally a low yield step and forcing the reaction conditions (i.e using a large excess of brominating agent, increasing the temperature and/or the reaction time, or using a promoting agent like pyridine) in the attempt to increase the yield invariably lead in great extent to di-brominated or poly-brominated isomers. Moreover, separation of various halogenated compounds by preparative chromatography is quite labour intensive and often translates into a considerable loss of the target mono-brominated derivative during its isolation. Thus, poor efficiency and low productivity of this method make it unsuitable for application to a large-scale synthesis.

We started this study by performing the conventional batchwise synthesis with two different protocols reported in literature namely the method reported by Callot,[11] which employs N-bromo succinimide (NBS) in chloroform (therein referred as Method A), and the procedure reported by Zhang,[12] which substantially the same of Callot but using pyridine as a reaction promoter (Method B). According to Method A, TPP was mixed in chloroform with 1.8 equivalents of NBS and stirred for 6 hours at room temperature. TLC analysis showed four spots corresponding to the target TPPBr, two isomeric $TPPBr_2$ derivatives, together with some unreacted TPP. HPLC analysis of the reaction mixture allowed the quantitative determination of target TPPBr (51%), as well as the $TPPBr_2$ (41% as an isomeric mixture), and the unreacted TPP (8%). It is worthy to note that, despite the decent HPLC yield, the purification of TPPBr by preparative gravity column chromatography on silica (eluent: toluene-cyclohexane 1:1 v/v) was quite elaborated and gave an isolated yield of only 18%. On the other hand, according to Method B, a $CHCl_3$ solution of TPP in the presence of an excess of pyridine was subjected, under reflux, to a slow (4 hours) drop-wise addition of NBS solution in chloroform (3 equivalents). After refluxing for further 2 hours, the reaction was quenched with acetone and analyzed by HPLC showing a composition of 76% TPPBr, 21% $TPPBr_2$, and 3% unreacted TPP. Preparative chromatography using the same conditions reported for Method A, led to a 30% isolated yield of target TPPBr. Although isolated yield for Method B was almost twice than Method A, the main drawback was the use the unpleasant pyridine and the larger excess of NBS (3 equivalent rather than 1.8 for protocol A) so we decided to develop a continuous-flow synthesis on the protocol A. To this purpose we used the Vapourtec MR platform set-up according the scheme reported in figure 76.

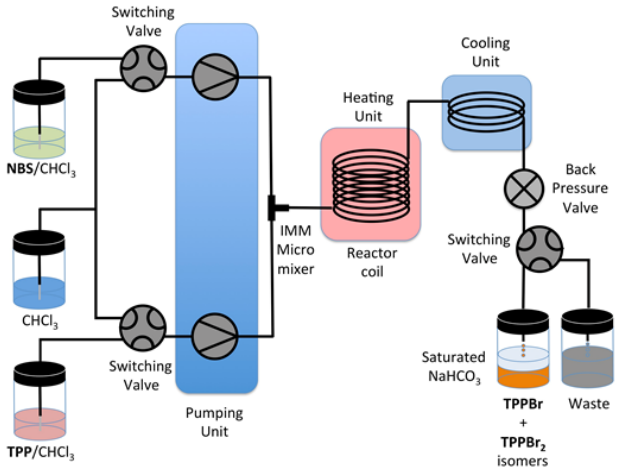

Figure 76. Experimental set-up for continuos-flow monobromination of TPP.

This apparatus allowed to produce mixtures of TPP and NBS with a predetermined stoichiometric ratio which were subsequently injected through a switching valve, as a plug, in a flow of chloroform solvent which carries them along the MR. The latter was constituted by a coil of PTFE tubing maintained at a constant temperature in a thermostatic chamber. A built-in software evaluates, according the experimental parameters, the expected dispersion of the plug due to diffusion and triggers a switching valve placed at the reactor outlet with the purpose to collect exclusively the inner, most concentrated part of the reaction plug. This operational procedure allows minimizing the reagent consumption during the optimization of the reaction parameters, a fundamental issue when more elaborated porphyrins have to be selectively monobromurated. In addition, since mixing efficiency is likely to be a key factor in determining TPP mono-versus poly-bromination selectivity, we managed to enhance the standard mixing capability of Vapourtec apparatus by using a IMM slit interdigital micromixing device that combines feed streams by a multilamination process allowing a complete mixing in the millisecond range. At least not last, it should be pointed out that quenching effectively and reproducibly a reaction at the outlet of a MR is crucial to be sure that the sample collected is really representative of what is going on inside the MR without any post-MR contribute. Since the reaction under study is likely to be slowed down by decreasing the temperature, we added a thermal quenching coil at the end of the MR. In addition, a chemical quenching was also applied by collecting the sample on a $NaHCO_3$ saturated aqueous solution. Several experiments were carried out in order to determine the influence of key parameters such as residence time, reaction temperature, and TPP/NBS ratio on reaction yield and selectivity. Results are summarized in Table 9. First of all, we studied the effect of the temperature on the outcome of the TPP bromination (Table 9, entries 1÷4). It is noteworthy that by placing a 100 psi back-pressure regulator at the end of the reaction stream the reaction temperature could be safely raised well

above the boiling point of the solvent (61°C in the case of chloroform), an option not easily accessible with a conventional apparatus. For these experiments the TPP/NBS molar ratio was set to 1 and the residence time was set to 5 minutes to assure a reasonable productivity.

Entry	Residence time (min)[a]	T (°C)	**NBS** (equivalents)	**TPP** (%)[b]	**TPPBr** (%)[b]	**$TPPBr_2$** (%)[b]
1	5	25	1.0	92	9	0
2	5	75	1.0	76	22	2
3	5	100	1.0	54	42	4
4	5	125	1.0	47	48	5
5	1	125	1.0	75	23	2
6	2	125	1.0	64	33	3
7	8	125	1.0	33	61	6
8	10	125	1.0	33	60	7
9	5	125	0.8	47	50	4
10	5	125	1.1	33	56	11
11	5	125	1.25	26	59	15
12	5	125	1.5	12	69	19
13	8	125	1.0	26	67	7

Table 9. Effect of the residence time (min), temperature (°C) and NBS equivalents on TPP bromination under continuous flow conditions.[b]Determined by HPLC analysis (Column: Phenomenex 5 µm; Eluent: cyclohexane/toluene 80:20 in volume in the presence of 0.1% triethylamine; Detector: UV-vis set at 420 nm).

Experiments were carried out at 25, 75, 100, and 125°C. Bromination of TPP at 25°C (entry 1) produced TPPBr only in a minimum extent (8%) thus demonstrating the reaction is essentially thermal in nature. Indeed, raising the temperature to 75°C then to 100°C and to 125°C resulted in an increased formation of TPPBr to 22%, 42% and 48% respectively. Most significantly, the amount of dibrominated porphyrins was very low even at 125°C (5%). On the basis of these results, we decided to set up the temperature to 125°C for all subsequent optimization experiments. As a second operational parameter, we studied the effect of the residence time by setting its value to 1, 2, 8, and 10 minutes (Table 9, entries 5÷8). As expected, by decreasing the residence time from 5 (entry 4) to 1 minute (entry 5) the TPPBr yield dropped from 48% to 23%. On the other hand, increasing the residence time to 2, 8 and 10 minutes resulted in a rising of the amount of TPPBr produced to 33%, 61%, and 60%, respectively. Interestingly, the amount of $TPPBr_2$ isomers was 7% or less.

Although the yield of about 60% observed for 8 and 10 minutes residence time was appealing with respect of the 48% yield obtained with a residence time of 5 minutes, we believe that it is not enough to compensate the diminished productivity resulting from an increasing residence time. Therefore we decided to keep the residence time set at 5 minutes and to study the effect of the number of equivalents of NBS on the reaction outcome (entries 9÷12). We tested 0.8, 1.1, 1.25, 1.5 equivalents of NBS with

respect to TPP. By using increasing amounts of NBS the yield of TPPBr could be raised up to 69% (entry 12) but at the price of a concomitant building up of $TPPBr_2$ isomers up to 19%. Being aware from the batch experiment that the isolated yield can be much lower than the HPLC yield as result of purification difficulties, we also performed a preparative scale test. One of the advantages of the microreactor technology is that the scaling up process does not require, as often happens in the case of syntheses carried out batch-wise, re-optimization of the experimental conditions. Indeed, reactor can be parallelized or simply kept running until the desired amount of target compound is produced. We thus employed conditions of entry 6 (rather than using the best performing conditions of entry 13, to obtain a larger productivity) to process a total amount of 100 mg (0.163 mmol) of TPP. The collected output stream was first analysed by HPLC, resulting in a mean product distribution very close to the expected one, and then chromatographed over silica to give 53 mg (0.076 mmol) of TPPBr, corresponding to 47% isolated yield. Finally, in view of a possible future application to a larger scale production of TPPBr we also managed to increase the process productivity by doubling the reactor volume (10 mL instead of 5mL). Surprisingly, we could observe even a yield increased up to the 67% together with a very good selectivity for the TPPBr derivative (entry 13). This was probably due to an enhancement of efficiency of the mixing device determined by the higher flow rates used.

In conclusion, we have demonstrated that a higher degree of reaction control for bromination of TPP is achievable thanks to continuous flow reactors. Flow conditions could be tuned to favour both product yield or selectivity depending on desired recovering of starting material. In any case, larger space-time yields respect to batch methods could be obtained. Moreover, the flow process developed in this study has been demonstrated to be easily scalable to higher production.

Experimental part

Method A (Batch synthesis)

A mixture of TPP (200 mg, 0.326 mmol) and NBS (102 mg, 0.573 mmol, 1.8 equivalents) in CHCl3 (50 mL) was stirred at room temperature for 6 hours. The solvent was evaporated and the solid residue was washed with water, extracted with chloroform and dried on Na2SO4. HPLC yields: 51% TPPBr, 41% TPPBr2, 8% unreacted TPP. Preparative chromatography by gravity on silica column (eluent: toluene:cyclohexane 1:1 v/v) afforded 41 mg of TPPBr (18% isolated yield). 1H-NMR (300 mHz, CDCl3, □ in ppm): 8.95-8.84 (m, 5H), 8.79 (m, 2H), 8.28-8.17 (m, 6H), 8.15-8.09 (m, 2H), 7.86- 7.70 (m, 12H), -2.80 (s, 2H). 13C-NMR (75 MHz, CDCl3, □ in ppm): 142.04, 141.71, 140.80, 138.02, 134.57, 134.52, 134.50, 134.40, 134.30, 129.59, 128.79, 128.21, 127.93, 127.81, 126.94, 126.80, 126.72, 126.69, 120.72, 120.28, 120.01, 119.56. UV-vis (CH_2Cl_2, λmax nm, Log ε) 421 (5.55), 518 (4.27), 553 (3.72), 593 (3.70), 648 (3.67); Mass Spectrometry (ESI-MS): 693 (M+1)+, 347 [(M+2)/2]+; Fluorescence (CH2Cl2, excitation at 420 nm, λmax nm): 657, 718.

Method B (Batch synthesis)

To a three neck round-bottom flask charged with TPP (1.27 g, 2.1 mmol) and CHCl3 (300 mL) pyridine (12 mL) was added. After refluxing for 5 min, a solution of NBS (1.12 g, 6.3 mmol, 3.0 eq) in CHCl3 (500 mL) was added dropwise in 4 hours. The solution was then refluxed for an additional 2 hours, quenched with acetone (150 mL), and concentrated by rotary evaporator to dryness (HPLC yields: 76% TPPBr, 21% TPPBr2, 3% unreacted TPP). The residue was purified via gravity column chromatography (silica gel, toluene/cyclohexane 1:1), affording 437 mg of TPPBr (30% isolated yield).

Flow Synthesis

Reactions under flow-conditions were performed using a Vapourtec R platform supplied by Vapourtec Ltd (UK) coupled with a IMM micromixer (Meinz, Germany). The reactors coil employed were PTFE tubes with a total internal volume of 5 and 10 ml, equipped with a back-pressure (100 psi) cartridge. Solutions of TPP and NBS in CHCl3 were used as reactor feeds. A thermal quench was performed at the end of the reactor assembly using a refrigerated coil, followed by chemical quench/extraction step at the collection point performed thorough dropping of reaction output in saturated aqueous bicarbonate solution. After phase separation the organic layer was collected and diluted with chloroform, dried over magnesium sulphate and accurately

filtered. Collected samples were than analyzed by HPLC after a proper dilution with the eluting phase.

References and notes

1. R. Paolesse Ed., *Applications of Porphyrinoids*, Series 34 Topics in Heterocyclic Chemistry, Springer-Verlag, Berlin, Heidelberg, **2014**.
2. T. Carofiglio, *Chemical Communications*, **2013**, 49, 8525.
3. *Multiporphyrin Arrays: Fundamentals and Applications*, Dongo Kim Ed., Taylor & Francis, **2012**.
4. M. O. Senge, *Chemical Communications,* **2011**, 47, 1943.
5. T. Noël, *Chemical Society Reviews*, **2016**, 45, 83.
6. K. T. de Oliveira, *RSC Advances*, **2015**, 5, 84350.
7. N. Stock, *Inorganic Chemistry*, **2016**, 55, 5312.
8. M. Graetzel, *Angewandte Chemie International Edition*, **2014**, 53, 2973.
9. H. Shinokubo, *Chemical Rev*iews, **2017**, 117, 2910.
10. K. I. Kobrakov, *Chemistry of Heterocyclic Compounds,* **2009**, 45, 259.
11. a) H. J. Callot, *Tetrahedron Lett.* **1973**, 14, 4987; b) H. J. Callot, *Bulletin de la Société Chimique de France,* **1974**, 1492.
12. X. P. Zhang. *Journal of Organic Chemistry,* **2007**, 72, 9060-9066.

NMR spectra

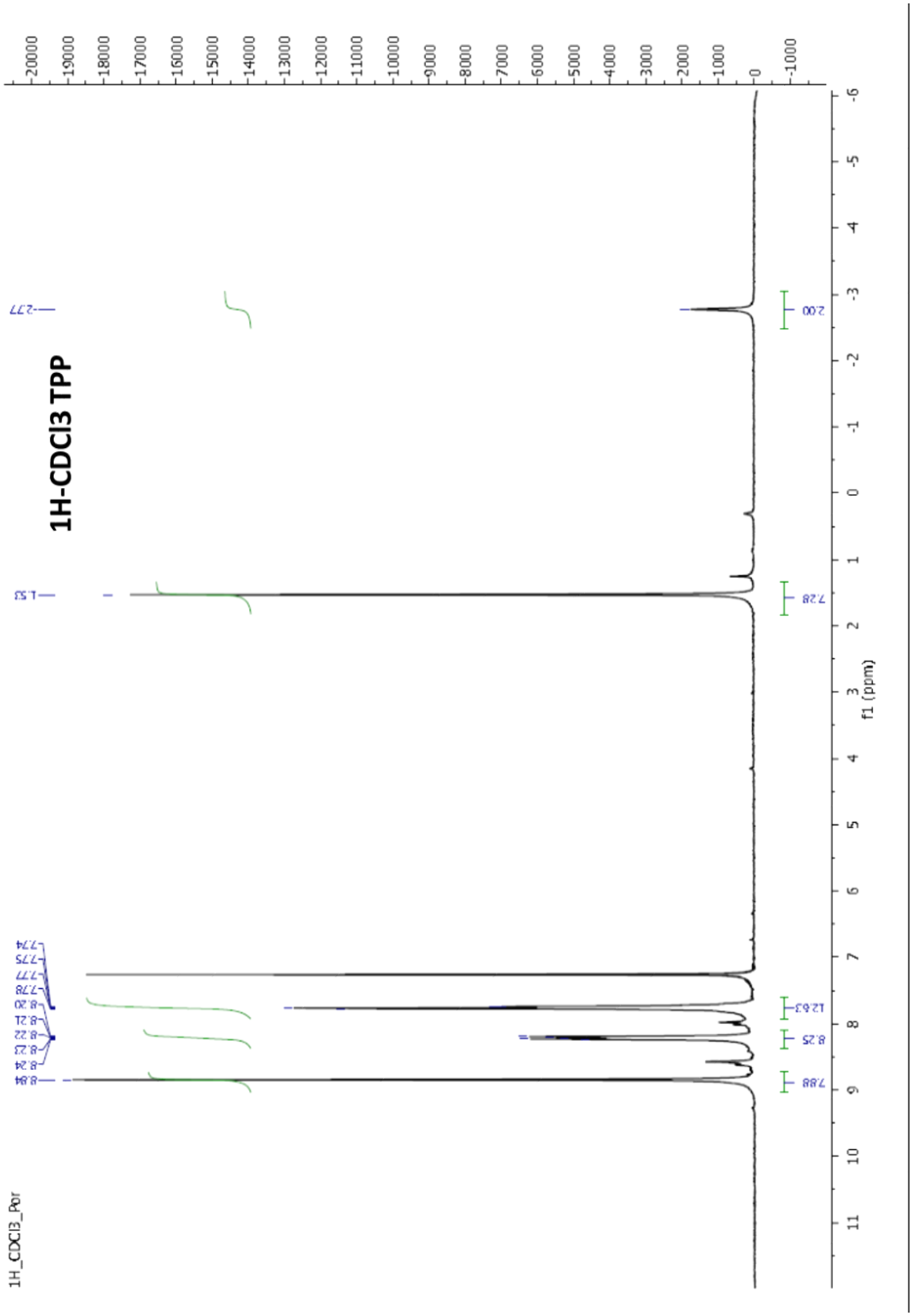

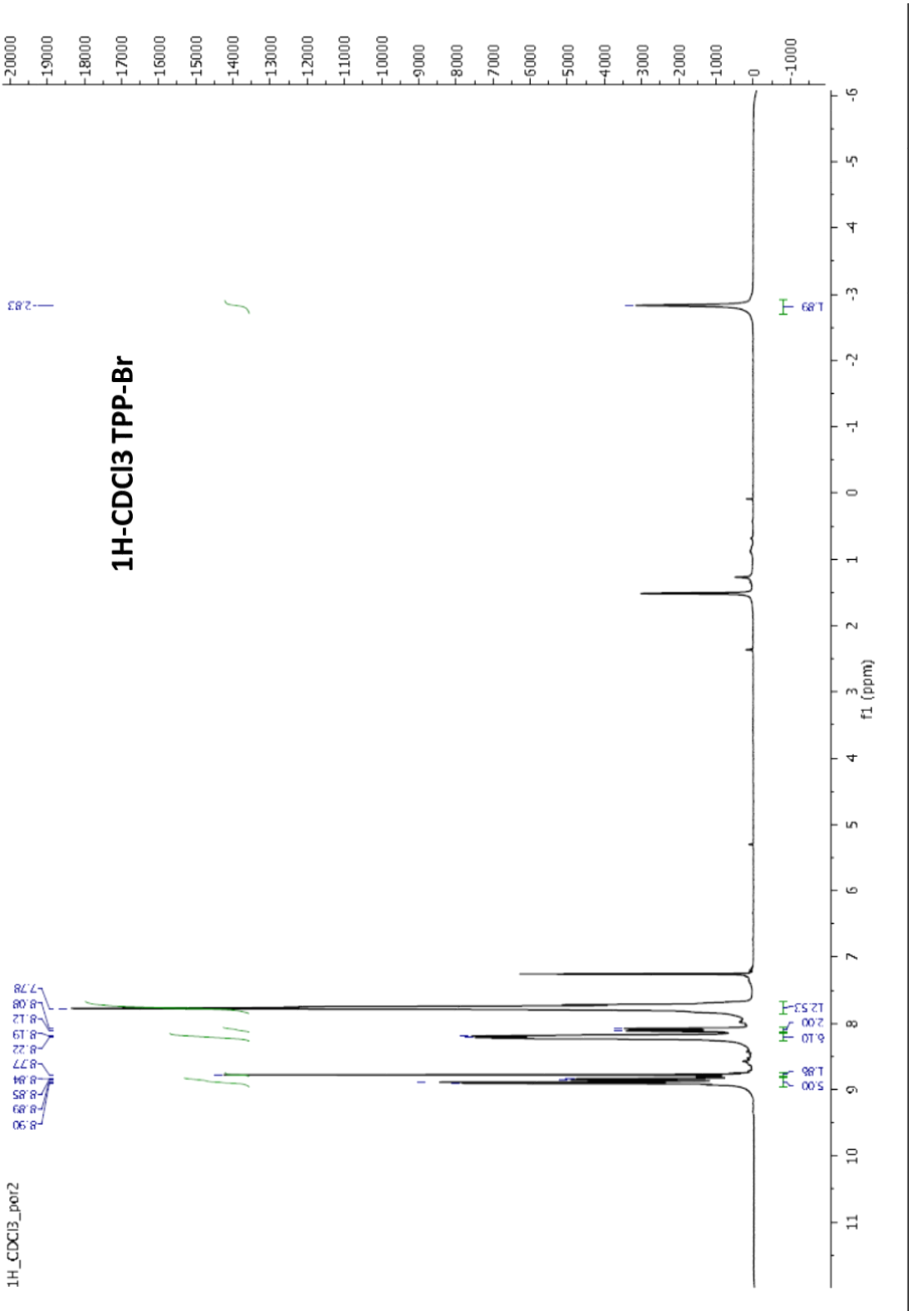
1H-CDCl3 TPP-Br
1H_CDCl3_por2
f1 (ppm)

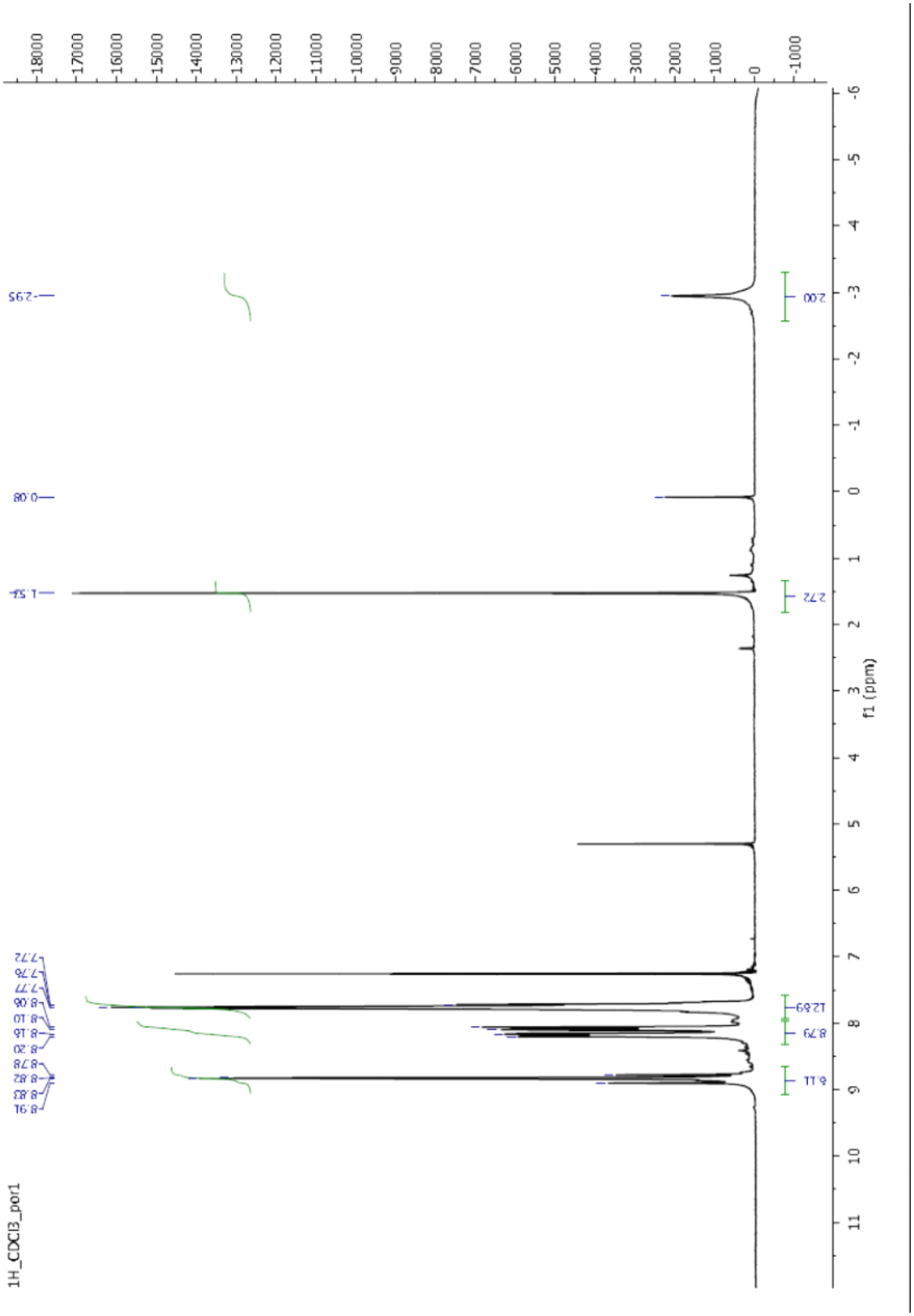
1H_CDCl3_por1
f1 (ppm)
2.95
0.08
1.52
2.00
2.72
12.69
8.79
6.11
8.91
8.83
8.82
8.78
8.20
8.16
8.10
8.06
7.77
7.76
7.72

Reagents and instruments

Commercial solvents and reagents are reported in Tables. Solvents and reagents were used without any further purification, unless specified.

Solvent	MW [g/mol]	d [g/ML]	b.p. [°C]	Seller
Toluene	92.14	0.867	110.6	Sigma-Aldrich
Dimethyl sulfoxide	78.13	1.1	189	Sigma-Aldrich
Tetrachloromethane	153.82	1.594	76-77	Sigma-Aldrich
Chlorobenzene	112.56	1.106	132	Sigma-Aldrich
Ethyl acetate	88.11	0.901	77	Sigma-Aldrich
Acetonitrile	41.05	0.786	81-82	Sigma-Aldrich
Acetone	58.08	0.791	56	Sigma-Aldrich
Isooctane	114.23	0.692	98-99	Sigma-Aldrich
Methanol	32.04	0.791	64.7	Sigma-Aldrich
DMF	73.10	0.948	153 – 155	Sigma-Aldrich
Ethanol	46.06	0.789	78	Sigma-Aldrich
Chloroform	119.38	1.492	60.5 – 61.5	Sigma-Aldrich

Reagent	MW [g/mol]	d [g/ML]	b.p. [°C]	Seller
Triethylamine	101.19	0.726	88.8	Sigma-Aldrich
Methyl-trimethoxysilane	136.22	0.955	102-104	Sigma-Aldrich
t-buthyl-dimethyl-chlorosilane	150.72	solid	-	Sigma-Aldrich
n-octadecyl-dimethyl-chlorosilane	347.09	solid	145-155	Sigma-Aldrich
Fluorescein isothiocyanate	389.38	solid	-	Sigma-Aldrich
Methyl methacrylate	100.12	0.936	100	Sigma-Aldrich
Bromine	159.81	3.119	58.8	Sigma-Aldrich
3-aminopropyl triethoxysilane	221.37	0.946	217	Sigma-Aldrich
C60-fullerene	720.66	solid	-	
1,3-diphenyl-isobenzofuran	270.32	solid	-	Sigma-Aldrich
Zinc nitrate hexahydrate	297.49	solid	-	Sigam-Aldrich
Sodium sulfide	240.18	solid	-	Alfa Aesar
Manganese chloride tetrahydrate	197.91	solid	-	Sigma-Aldrich
Copper chloride dihydrate	170.48	solid	-	Sigma-Aldrich
Nickel chloride hexahydrate	237.69	solid	-	Sigma-Aldrich
Europium chloride hexahydrate	366.41	solid	-	Sigma-Aldrich
Samarium nitrate hexahydrate	444.67	solid	-	Sigma-Aldrich
Neodimium nitarte hexahydrate	438.35	solid	-	Sigma-Aldrich
Ytterbium chloride hexahydrate	387.49	solid	-	Sigma-Aldrich

Sodium nitroprusside dihydrate	297.95	solid	-	Sigma-Aldrich
Glycin	75.07	solid	-	Sigma-Aldrich
Sodium phosphate	163.94	solid	-	Sigma-Aldrich
Sodium phosphate dibasic	141.96	solid	-	Sigma-Aldrich
GM1 dye	356.54	solid	-	
Sulfuric acid	98.08	1.84	290	Sigma-Aldrich
Sodium hydroxide	40.00	solid	-	Sigma-Aldrich
Sodium carbonate	105.99	solid	-	Sigma-Aldrich
Tetraethoxy silane	208.33	0.933	168	Sigma-Aldrich
Chloridric acid	36.46	1.2	>100	Sigma-Aldrich
Trizma base	121.14	solid	219-220	Sigma-Aldrich
Urease	Type III, glycerol solution, 500-800 units/ML			Sigma-Aldrich
Urea	60.06	solid	-	Sigma-Aldrich
Iron (II) chloride tetrahydrate	198.81	solid	-	Sigma-Aldrich
Iron (III) chloride hexahydrate	270.30	solid	280-285	Sigma-Aldrich
Ammonium hydroxide	35.05	0.9	-	Sigma-Aldrich
Oleic acid	282.46	0.89	194-195	Sigma-Aldrich
Dopamine	189.64	solid	-	Sigma-Aldrich
TEMPO	156.25	solid	-	Sigma-Aldrich
Sodium bromide	102.89	solid	-	Sigma-Aldrich
MES	206.73	solid	-	Sigma-Aldrich
N-3-dimethylaminopropyl-N'-ethyl carbodiimide	191.70	solid	-	Sigma-Aldrich
N-Hydroxysuccinimide	115.09	solid	-	Sigma-Aldrich
Sodium alginate	-	solid	-	Sigma-Aldrich
Calcium chloride	110.98	solid	-	Sigma-Aldrich
HEPES	238.30	solid	-	Sigma-Aldrich
Tannic acid	-	solid	-	Sigma-Aldrich
Kaiser test	Ready-made kit			Sigma-Aldrich
ISOTER4537	Ready-made polyols mixture			Dow-Du Pont
ISOTER4530	Ready-made polyols mixture			Dow-Du Pont
ISOTER842G	Ready-made polyols mixture			Dow-Du Pont
Voranate M600	Ready-made di-isocyanate mixture			Dow-Du Pont
N,N-Dimethyl-cyclohexylamine	127,23	0.849	158-159	Sigma-Aldrich
N,N,N',N'',N''-pentamethyl-diethylenetriamine	173.30	0.83	198	Sigma-Aldrich

Materials	**Dimension**		**Seller**
Silica nanoparticles	Length -	Diameter 110.98 (nm)	Sigma-Aldrich

Cellulose nanocrystals	Length 100-200 (nm)	Diameter ≈5 (nm)	Melodea

UV-Vis-NIR spectroscopy

Uv-Visible spectra were acquired with a Varian Cary 5000 spectrometer, at room temperature, between 280 and 1500 nm, with interval 0.5 nm, scan speed 300 nm/min and spectral bandwidth 2 nm. Quartz cuvettes with 1 cm optical path were used for the measurements.

FT-IR spectroscopy

FT-IR spectra were acquired in a spectral range between 4000 and 400 cm^{-1}. Transmission measurements were performed on a FT-IR Nicolet 5700 spectrometer.

Thermogravimetric analysis

TGA measurements were carried on a TGA Q5000IR (TA instruments). The analyses were performed with a 10°C/min thermal ramp from 100°C to 1000°C. The analysis was performed on dried samples, with a 30 minutes isoterm at 100°C to ensure the elimination of the solvent.

Elemental analysis

Elemental analysis was performed by the technical service of the Department of Chemistry of the University of Padova.

Transmission electron microscopy

TEM micrographs where obtained with a FEI Tecnai G12 microscope operating at 100 kV, equipped with a OSIS Veleta camera. Samples were prepared by suspending the dried powders in water through sonication and then deposited on 300 mesh lacey carbon coated copper grids.

Microtip sonication

Dispersions obtained by microtip sonication were performed with a Titanium tip Misonix 3000 sonicator. The sonication was performed with a 3s ON - 3s OFF interval at power level 2.0 (4 − 6 Watt). The sonication time was varied according to the specific procedure.

Centrifugation

The centrifugation was performed on a MR23i jouan (Thermo Scientific) centrifuge equipped with a variable angle rotor (model 11174711/11174720). 50 ML, conical bottom, Duran glass centrifuge tubes were used for all the centrifugation procedures.

Emulsification with a homogenizer

The emulsification with a homogenizer was carried out using an Ultra Turrax instrument (model T25) equipped with a stainless steel rotor-stator emulsifier. The tip used (model S 25 N-25 F) consists in two concentric parts: an external crown gear and an internal rotating gear. The homogenizer was employed at 5000 rpm for 5 minutes, if not specified otherwise.

Microfluidic equipment for ZnS nanoparticle synthesis

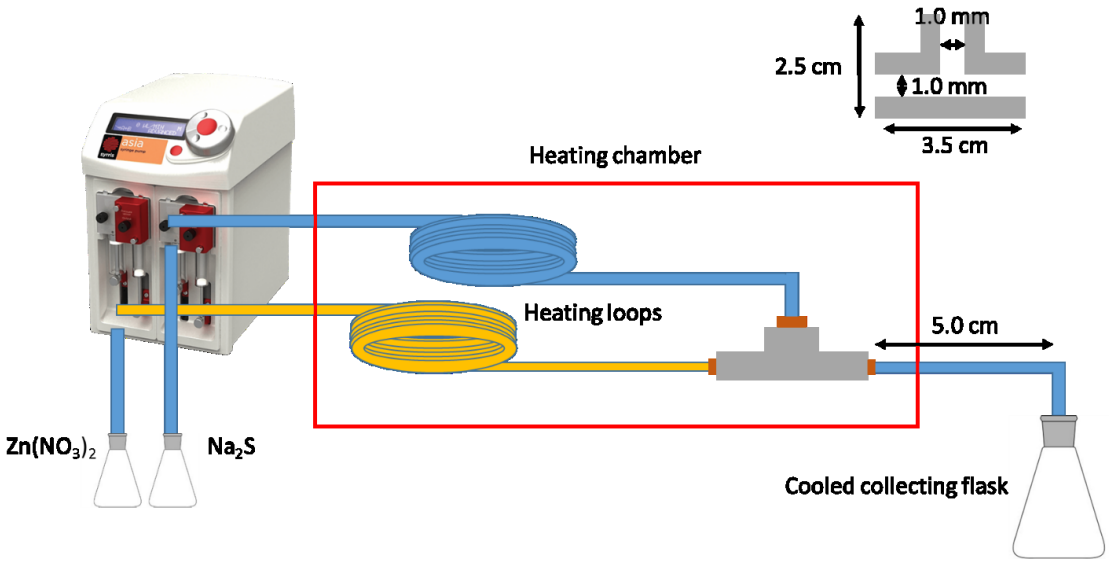

Microfluidic experiments were performed using **PTFE** tubes (OD 1/16, ID 1/32, supelco item no. 58699), if not specified otherwise. An oil bath was used to evaluate the temperature effect on the reaction. Reagents were pumped using an automatic pumping system (Syrris, Asia reciprocating siringe pump) and a T-shaped stainless steel homemade junction was used. Connections between tubing and the junction were realized wit female luer to female 10-32 adapters Tubes dimensions, setup and flow rates varies according to the needs of specific experiments.

Photo-oxidation reactor

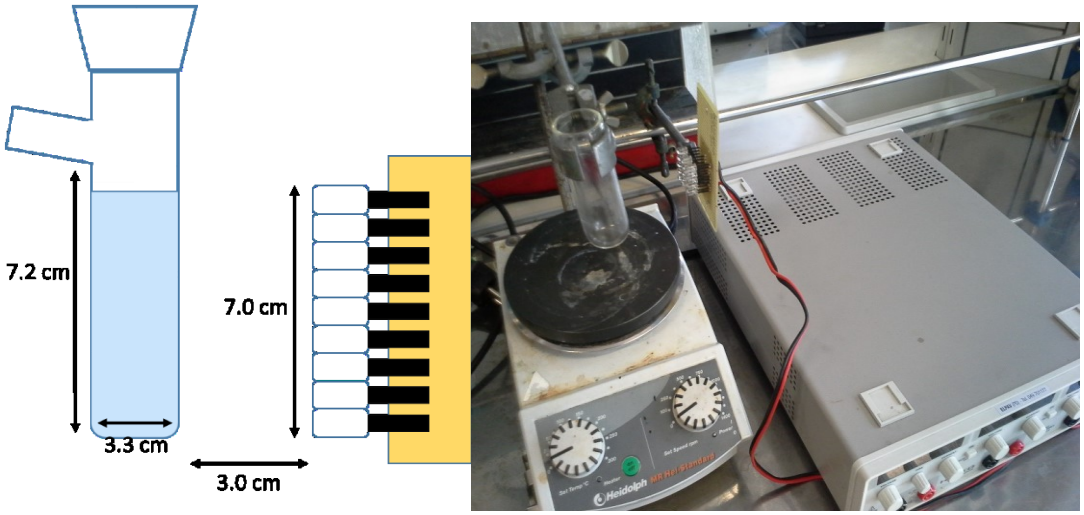

The photocatalytic oxidation was carried on inside a cylindrical glass reactor (dimensions in figure). A lateral arm allowed the introduction of gases. White leds (model ML50W13H-BED, emission spectrum 440-630 nm with two broad peaks at 480 nm and 580 nm) were supplied by a HAMEG instrument (model HM7042-S, Elpav Instruments Padua).